Theory of metal-insulator transitions in graphite under high magnetic field

Zhiming Pan, Xiao-Tian Zhang, and Ryuichi Shindou[*]

International Center for Quantum Materials, School of Physics, Peking University, Beijing 100871, China
and Collaborative Innovation Center of Quantum Matter, Beijing 100871, China

Graphite under high magnetic field exhibits consecutive metal-insulator (MI) transitions as well as reentrant insulator-metal (IM) transitions in the quasiquantum limit at low temperature. In this paper, we identify the low-T insulating phases as excitonic insulators with spin nematic orderings. We first point out that graphite under the relevant field regime is in the charge neutrality region, where electron and hole densities compensate each other. Based on this observation, we introduce interacting electron models with electron pocket(s) and hole pocket(s) and enumerate possible umklapp scattering processes allowed under the charge neutrality. Employing effective boson theories for the electron models and renormalization group analyses for the boson theories, we show that there exist critical interaction strengths above which the umklapp processes become relevant and the system enters excitonic insulator phases with long-range order of spin superconducting phase fields ("spin nematic excitonic insulator"). We argue that when a pair of electron and hole pockets gets smaller in size, a quantum fluctuation of the spin superconducting phase becomes larger and destabilizes the excitonic insulator phases, resulting in the reentrant IM transitions. We also show that an odd-parity excitonic pairing between the electron and hole pockets reconstructs surface chiral Fermi arc states of electron and hole into a 2-dimensional helical surface state with a gapless Dirac cone. We discuss field and temperature dependencies of in-plane resistance by surface transport via these surface states.

I. INTRODUCTION

Graphite under high magnetic field exhibits a metal-insulator transition at low temperature ($H \geqslant H_{c,1} \simeq 30$ T) [1,2]. The transition has been often considered as a prototype of one-dimensional Peierls density-wave instability associated with the $2k_F$ logarithmic singularity in the Lindhard response function [3–12]. A transition temperature T_c of the density wave ordering is determined by a BCS-type gap equation, $\ln T_c \propto -1/\rho(0)$. The density of states at the Fermi level $\rho(0)$ is proportional to the magnetic field H, so that T_c increases monotonically in the magnetic field [3–6]. Further experiments discovered that graphite shows another metal-insulator transition ($H \geqslant H_0 \simeq 53$ T) [13–21] as well as an insulator-metal reentrant transition at higher magnetic field ($H = H_{c,2} \simeq 75$ T) [17–21]. So far, there exist at least two distinct low-temperature insulating phases in graphite under high magnetic field: one insulating phase in the range $H_{c,1} < H < H_0$ and the other in the range $H_0 < H < H_{c,2}$. The reentrant transition at $H = H_{c,2}$ indicates the presence of a normal metal phase with pristine electron and hole pockets above the transition field, bringing about a skepticism against the density wave scenarios. Namely, the transition temperature of the density wave phase would increase monotonically in the field, until the electron and hole pockets that would form the Peierls density wave leave the Fermi level [3–6].

Theoretically, stabilities of the Peierls density wave phases against random single-particle backward scatters depend crucially on a commensurability condition of an electron filling [22–25]. From preceding *ab initio* band calculations of graphite under high magnetic field [8,19], a sequence of specific values of the field in the range 30 T $\lesssim H \lesssim$ 50 T satisfies the commensurability condition. Nonetheless, experimental transition temperatures of the two insulating phases do not show any dramatic sensitivies on certain values of the field in the range. Both of the insulating phases range rather broadly in field (over 20 T) [17–21].

In this paper, we explain these two low-T insulating phases in graphite under the high field as manifestation of excitonic insulators with spin nematic orderings (Fig. 1). We first argue that graphite under high magnetic field ($H \gtrsim 20$ T) is in the charge neutrality region, where electron density and hole density compensate each other. Based on this observation, we begin with interacting electron models with electron pockets and hole pockets, to enumerate possible umklapp scattering processes allowed under the charge neutrality condition. Using perturbative renormalization group (RG) analyses on their effective boson theories, we show that the umklapp terms have critical interaction strength above/below which they become relevant/irrelevant on the renormalization. Above the critical interaction strength, the umklapp term locks the total displacement field as well as spin superconducting phase field. The former locking causes the insulating behavior along the field direction, while the latter results in a long-range order of spin quadrupole moment. We explain the reentrant insulator-metal transition in graphite, through a quantum fluctuation of the spin superconducting phase field. We characterize the spin nematic excitonic insulator phases by out-of-plane (infrared optical) conductivity as well as in-plane transport property (out-of-plane current is parallel to the field). The field and
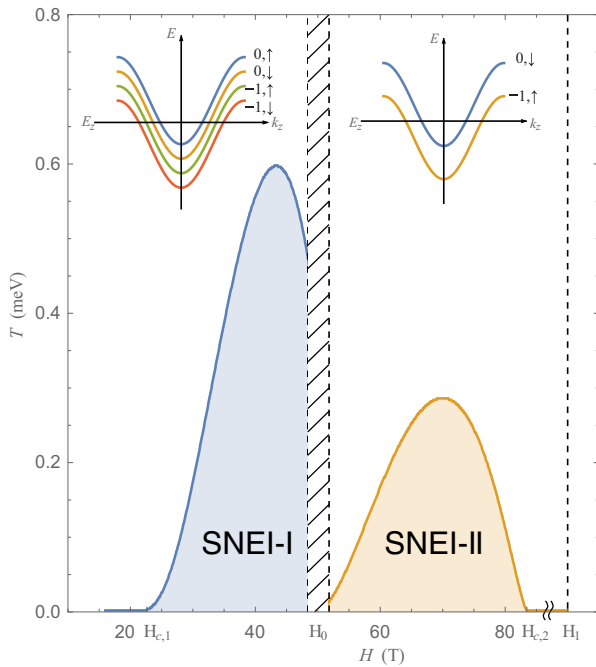
[*]rshindou@pku.edu.cn

FIG. 1. Theoretical phase diagram for graphite under high magnetic field. The phase diagram is obtained from the RG equations, Eqs. (42)–(44) for $H < H_0$ and Eqs. (67)–(69) for $H_0 < H < H_1$. "SNEI-I" and "SNEI-II" stand for two distinct spin nematic excitonic insulator phases (strong-coupling phase). For $H < H_0$, the electronic state near the Fermi level comprises two electron pockets ($n = 0$ LL with ↑ spin and ↓ spin) and two hole pockets ($n = -1$ LL with ↑ spin and ↓ spin). At $H = H_0$, the outer two pockets ($n = 0$ LL with ↑ spin and $n = -1$ LL with ↓ spin) leave the Fermi level. For $H_0 < H < H_1$, the electronic state has one electron pocket ($n = 0$ LL with ↓) and one hole pocket ($n = -1$ LL with ↑). We choose $H_0 = 50$ T and $H_1 = 120$ T. For a detailed parameter set of the RG equations, see Appendix C4. Our theory may not be able to predict much about a transition between SNEI-I and SNEI-II phases (the shaded area around $H = H_0$); see the discussion in Sec. X B. $T = 0$ metal-insulator transition at $H = H_{c,1}$ and insulator-metal transition at $H = H_{c,2}$ are the quantum phase transition with the dynamical exponent $z = 1$.

temperature dependencies of the transport properties are consistent with experimental observation in graphite.

A. Issues to be addressed in this paper

1. Direct metal-insulator transition

Under the magnetic field H ($\parallel z$), kinetic energy part of the three-dimensional semimetal takes the form of decoupled one-dimensional quantum chains (or quantum wires). Namely, the kinetic energy within the xy plane is quenched by the Landau quantization, while the kinetic energy along the field direction remains intact, forming one-dimensional momentum-energy dispersion. As a result, density correlation function calculated within the random phase approximation (RPA) is characterized by the Lindhard response function in the one dimension [3,4]. The function has the logarithmic singularity at $k_z = 2k_F$, where $2k_F$ is a distance between the left and right Fermi points in the same energy band [26]. Thereby, the system has a generic instability toward the charge

density wave ordering, that breaks the spatially translational symmetry along the field direction [3–12].

Meanwhile, graphite under the relevant field regime has four bands that run across the Fermi level (two electron pockets and two hole pockets; $H \lesssim H_0 \simeq 53$ T) or two bands (one electron pocket and one hole pocket; $H_0 \lesssim H$) [8,19]. When each of these four (or two) bands would undergo the Peierls density wave (DW) instabilities individually, the respective instabilities would appear at different critical temperatures or critical fields. In other words, a graphite transport experiment would observe a stepwise increase of the (out-of-plane) resistance R_{zz} on lowering temperature or on increasing the magnetic field.

Nonetheless, the graphite experiment observed a *direct* phase transition from high-T normal metal phase to the low-T insulating phase [16–18,20,21]. Around the transition, the resistance along the field direction R_{zz} continuously increases [16–21] and it increases by 100 times within windows of several kelvins or teslas [16–18,21]. These experimental observations clearly dictate that all the energy bands (pockets) at the Fermi level are gapped out *simultaneously* at the transition point. Thereby, the key question to be asked here is, What is a "talking channel" among these four (or two) bands that enables this direct metal-insulator transition?

In this paper, we consider this channel as *umklapp scattering terms* and construct a mean-field theory that explains this direct metal-insulator transition. To be more specific, all the excitonic insulator phases discussed in this paper are stabilized by the umklapp terms that lock a *total* displacement field along the field direction, a sum of the displacement fields of the four (or two) bands. When the umklapp terms become relevant in the standard RG argument sense, the total displacement field (electric polarization) is locked, resulting in the electrically insulating behavior along the field direction. By calculating an optical conductivity along the field direction, we explicitly demonstrate the presence of finite mobility gaps in the excitonic insulator phases.

2. Reentrant insulator-metal transition

The second issue is the reentrant insulator-metal transition observed at the higher field region in the graphite experiment [14–21], which can hardly be explained by the conventional Peierls DW scenarios. Namely, the RPA density correlation function at finite temperature suggests that the transition temperature of the Peierls DW phase increases monotonically in the field, until the electron and/or hole pockets that would form the DW leave the Fermi level. When they leave the Fermi level, however, the electronic state simply ends up in a semiconductor phase rather than metallic phase. Contrary to this, the graphite experiments clearly observe the insulator-*metal* reentrant transition in the higher-field region. The low-T electric transport along the field direction above the critical field ($H > H_{c,2} \simeq 75$ T) is as metallic as the electric transport in the high-T normal metal phase [17,18,21]. The experiment clearly indicates the presence of pristine electron and hole pockets at the Fermi level above the critical field.

In this paper, we explain this reentrant insulator-metal transition as a consequence of quantum *spin* fluctuation enhanced by raising the magnetic field. To be more specific,

we first point out that the umklapp terms lock not only the total displacement field but also a *spin superconducting phase field*, a difference between a superconducting phase field of an electron/hole pocket with ↑ spin and hole/electron pocket with ↓ spin. The higher magnetic field makes the electron and hole pockets to be smaller in size in the k_z space. In the presence of the repulsive electron-electron interaction, the smaller pockets make their Luttinger parameters smaller than the unit. Smaller Luttinger parameters mean larger quantum fluctuation of superconducting phase field as well as the spin superconducting phase field. Thus, we can naturally argue that in the presence of such smaller electron and hole pockets, the umklapp terms suffer from the enhanced quantum *spin* fluctuation, and become irrelevant in the RG argument sense. When the umklapp terms become irrelevant, the spin superconducting phase field as well as the total displacement field is unlocked, resulting in the reentrant insulator-metal transition. Importantly, the electronic state still possesses electron and hole pockets above the critical field, though their sizes in the k_z space might be small.

3. Field dependence of in-plane resistance

The third issue to be addressed in this paper is an unusual field dependence of the electric transport in the directions transverse to the magnetic field [14–21]. Generally, the bulk electric transport perpendicular to the field is quenched in the clean limit at low temperature ($T \ll \hbar\omega_0$; $\hbar\omega_0$ is the cyclotron frequency). Nonetheless, the system still has low-T electric transport perpendicular to the field through the so-called surface chiral Fermi arc (SCFA) states [27,28]. The associated surface resistance is inversely proportional to a length of the arc in the k_z space. The length is approximately equal to the size of the respective electron (or hole) pocket in the bulk. The size of the pocket generally decreases in the field. Thereby, the surface resistance perpendicular to the field is expected to increase in the field.

Contrary to this theory expectation, the in-plane resistance R_{xx} in graphite under the field ($H \parallel z$) shows an unusual field dependence. The low-T resistance R_{xx} shows a broad peak around 15 T < H < 30 T [1,2,5,6,13–21]. From $H = 30$ T to $H = H_0 \simeq 53$ T, R_{xx} typically reduces by half [14–21]. Inside the high-field-side insulating phase ($H_0 < H < H_{c,2} \simeq 75$ T), the low-T in-plane resistance R_{xx} stays nearly constant in the field [17–21]. For $H_{c,2} < H$, R_{xx} starts increasing in the field again [21].

Field (nearly) independent and metallic R_{xx} in the high-field-side insulating phase can be naturally explained by a surface reconstruction of the SCFA states due to the excitonic pairing in the bulk. To be more specific, we will show that an *odd-parity* excitonic pairing between electron and hole pockets in the bulk reconstructs the SCFA state of the electron and that of the hole into a $(2 + 1)$-d helical surface state with a gapless Dirac cone. R_{xx} through such a Dirac-cone surface state is determined by carrier density doped in the surface region, which is typically independent of the magnetic field. Namely, unlike "decoupled" SCFA states of electron and hole, the reconstructed Dirac-cone surface state barely changes its shape as a function of the magnetic field. At the zeroth-order approximation, the field only changes the "depth" of the

band inversion between electron and hole pockets, while the shape of the Dirac-cone surface state is mainly determined by the excitonic pairing strength inside the inverted band gap. Thereby, one can naturally expect that the surface resistance due to the reconstructed Dirac-cone surface state is much less field-dependent than that of the decoupled SCFA states of electron and hole.

B. Structure of the paper

The structure of the paper is as follows. In the next section with the help of Appendix A, we argue that the graphite under the relevant field regime (20 T < H) is in the charge neutrality region, where electron and hole densities compensate each other. Based on this observation, we enumerate in Sec. III possible umklapp terms that are allowed under the charge neutrality condition in the four-pocket model (a model with two electron pockets and two hole pockets; $H \lesssim H_0 \simeq 53$ T). Employing a Hartree-Fock approximation, we construct effective field theories for possible insulating phases that can be stabilized by these umklapp terms (Sec. IV). There are three such phases: spin nematic excitonic insulator, magnetic Mott insulator, and plain excitonic insulator phases. Using renormalization group (RG) analyses, we argue for typical field dependencies of the respective transition temperatures of these three phases and conclude that the spin nematic excitonic insulator (SNEI-I) phase could naturally fit in the phenomenology of the low-field-side out-of-plane insulating phase ($H_{c,1} < H < H_0$) in the graphite experiment (Sec. V). In Sec. VI, we enumerate possible umklapp terms that are allowed under the charge neutrality condition in the two-pocket model (one electron and one hole pocket; $H_0 < H$). We construct effective field theories for the possible insulating phases that can be stabilized by the umklapp terms. We find two such phases: a phase with two superposed charge density waves and a spin nematic excitonic insulator (SNEI-II) phase. Using the RG analyses, we conclude that the SNEI-II phase can naturally explain the high-field-side out-of-plane insulating phase ($H_0 < H < H_{c,2}$). In Secs. VII and VIII, we discuss the field dependencies of the in-plane resistance in the graphite experiment by the surface electric transports. Especially, we show in Sec. VIII that the odd-parity excitonic pairing in the two-pocket model reconstructs the surface chiral Fermi arc (SCFA) states of electron and hole into a $(2 + 1)$-d helical surface state with a gapless Dirac cone. The surface Dirac-cone state could naturally explain the field (nearly) independent and metallic behavior of the in-plane resistance inside the high-field-side insulating phase. After a brief summary in Sec. IX, we give a discussion with a complementary viewpoint (Sec. X).

II. CHARGE NEUTRALITY REGIME IN GRAPHITE UNDER HIGH MAGNETIC FIELD

Low-temperature transport properties of graphite are dominated by four π-orbital bands around zone boundaries of the first Brillouin zone [29–31]. Graphite is a three-dimensional AB stacking of graphene layers. A unit cell has two graphene layers and it has four inequivalent carbon sites. Call them A, A', B, and B'. A and B share the same layer, and so do A' and B'. A comes right above A' in the cell. The
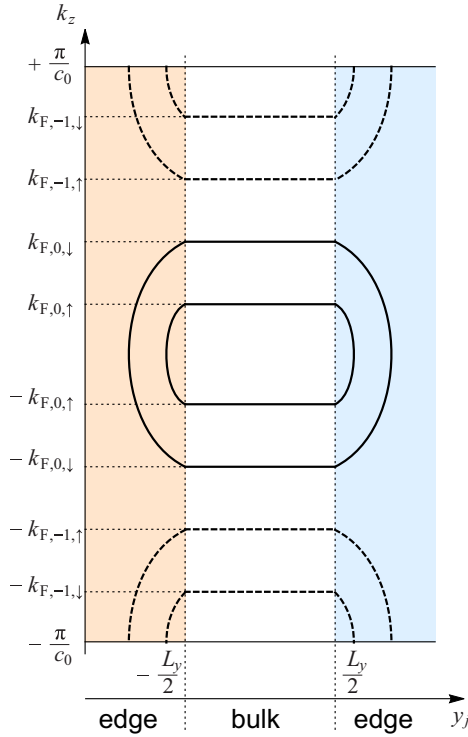
FIG. 2. Schematic picture of electronic states of graphite under high field ($H < H_0$). Solid/dotted lines describe Fermi surfaces of two electron/hole pockets in both bulk and edge regions. Two electron/hole pockets in the bulk region are terminated by electron/hole-type surface chiral Fermi arc states in edge regions, respectively. Namely, $E_{0,\sigma}(k_z, y_j)/E_{-1,\sigma}(k_z, y_j)$ goes higher/lower in energy, when y_j goes from the bulk region to the edge regions (see Appendix A).

electronic band structure near the Fermi level of graphite is composed of π orbitals of carbon atoms that are odd under the mirror with respect to the layer—for example, the $2p_z$ orbital [29–31]. π orbitals of A and A' carbon atoms hybridize rather strongly, forming two π-orbital bands at the zone boundaries that have large momentum-energy dispersions along the c axis (4000 K). Call these π orbitals π_A and $\pi_{A'}$, respectively. π orbitals of B and B' hybridize much more weakly, as B and B' are located right above the centers of the hexagon in their neighboring layers. These two, which we call π_B and $\pi_{B'}$ henceforth, form two degenerate bands at the zone boundaries that have a weaker energy-momentum dispersion along the c axis (400 K).

Under the field along the c axis, the four bands in the zone boundaries are split into Landau levels (LLs) [8,19,31–34]. For $H \gtrsim 30$ T, the $n = 0$ LLs with $\uparrow$ spin and $\downarrow$ spin form two electron pockets around $k_z = 0$, and the $n = -1$ LLs with $\uparrow$ spin and $\downarrow$ spin form two hole pockets around $k_z = \pi/c_0$ (Fig. 2). Here c_0 is a lattice constant along the c axis. According to the band calculation, the outer electron pocket ($n = 0$ LL with $\uparrow$ spin) and the outer hole pocket ($n = -1$ LL with $\downarrow$ spin) leave the Fermi level at $H = H_0 \simeq 53$ T.

The Hall conductivity measurements in a regime of 20 T $\lesssim$ $H \lesssim 60$ T [18,35–37] suggest that the number of the electron states and that of the hole states compensate each other almost completely. An estimation gives $N_e - N_h : L_z/c_0 = 10^{-4} : 1$,

where L_z is a linear dimension along the c axis, and N_e and N_h are numbers of the k_z points within the electron pockets and hole pockets, respectively (k_z is a crystal momentum along the c axis) (see Appendix A for the validity of the estimation).

III. FOUR-POCKET MODEL ($H < H_0$)

Based on this observation, we consider an electron model with two electron pockets ($n = 0$ LL with $\uparrow$ spin and that with $\downarrow$ spins) and two hole pockets ($n = -1$ LL with $\uparrow$ spin and that with $\downarrow$ spins) with the charge neutrality condition ($N_e = N_h$):

$$H_{\rm kin} = \sum_{k_z, j} \sum_{n=0,-1} \sum_{\sigma=\uparrow,\downarrow} E_{n,\sigma}(k_z) c^{\dagger}_{(n,\sigma),j}(k_z) c_{(n,\sigma),j}(k_z). \quad (1)$$

The two electron pockets encompass $k_z = 0$ and the two hole pockets are around the zone boundary $k_z = \pm\pi/c_0$ (Fig. 2),

$$E_{n,\sigma}(k_z) = -2\gamma_2[\cos(k_z c_0) - \cos(k_{F,n,\sigma} c_0)], \quad (2)$$

with $0 < k_{F,0,\uparrow} < k_{F,0,\downarrow} < \pi/(2c_0) < k_{F,-1,\uparrow} < k_{F,-1,\downarrow} < \pi/c_0$ [4]. An index j [$= 1, 2, \ldots, (L_x L_y)/(2\pi l^2)$] counts degenerate electron states within each LL. l denotes the magnetic length, $l \equiv \sqrt{\hbar c/(eH)}$. Since the kinetic energy part takes exactly the same one-dimensional momentum-energy dispersion along the k_z direction for different j, we regard the system as coupled chains and call j a "chain index" [38–40]. The charge neutrality condition takes the form of

$$k_{F,0,\uparrow} + k_{F,0,\downarrow} + k_{F,-1,\uparrow} + k_{F,-1,\downarrow} = \frac{2\pi}{c_0}. \quad (3)$$

For low-temperature electric transports at those temperature much below the bandwidth ($2\gamma_2 \simeq 400$ K), the kinetic energy part can be linearized around the Fermi points of each pocket ($k_z \simeq \pm k_{F,n,\sigma}$):

$$H_{\rm kin} = \sum_j \sum_{a,\tau} \tau v_{F,a} \int dz \, \psi^{\dagger}_{a,\tau,j}(z) i\partial_z \psi_{a,\tau,j}(z) + \cdots. \quad (4)$$

A chirality index τ specifies left mover ($\tau = -1$) or right mover ($\tau = +1$). $v_{F,a}$ is the bare Fermi velocity of each pocket with $a \equiv (n, \sigma)$. For simplicity, we label $(n, \sigma) = (0, \uparrow), (0, \downarrow), (-1, \uparrow)$, and $(-1, \downarrow)$ as $a = 1, 2, 3$, and 4, respectively, throughout this paper, e.g., $k_{F,a} \equiv k_{F,n,\sigma}$, $c_{a,j}(k_z) \equiv c_{(n,\sigma),j}(k_z)$, and $\psi_{a,\pm,j}(z) \equiv \psi_{(n,\sigma),\pm,j}(z)$. $\psi_{a,\pm,j}(z)$ is a slowly varying Fourier transform of those $c_{a,j}(k_z)$ around $k_z \simeq \pm k_{F,a}$:

$$\psi_{a,\tau,j}(z) \equiv \frac{1}{\sqrt{L_z}} \sum_{|k_z - \tau k_{F,a}| < \Lambda} c_{a,j}(k_z) e^{i(k_z - \tau k_{F,a})z}. \quad (5)$$

A short-ranged repulsive interaction is considered:

$$H_{\rm int} = \sum_{\sigma,\sigma'} \sum_{c,d=A,A',B,B'} \int d\boldsymbol{r} \int d\boldsymbol{r}' V(\boldsymbol{r} - \boldsymbol{r}')$$
$$\times \psi^{\dagger}_{\sigma}(\boldsymbol{r}, c) \psi^{\dagger}_{\sigma'}(\boldsymbol{r}', d) \psi_{\sigma'}(\boldsymbol{r}', d) \psi_{\sigma}(\boldsymbol{r}, c), \quad (6)$$

where

$$V(\boldsymbol{r}) \equiv \frac{g}{(\sqrt{2\pi})^3 l_{0,x} l_{0,y} l_{0,z}} e^{-\frac{z^2}{2l_{0,z}^2} - \frac{x^2}{2l_{0,x}^2} - \frac{y^2}{2l_{0,y}^2}}, \quad (7)$$

$\boldsymbol{r} \equiv (x, y, z)$, $\sigma, \sigma' = \uparrow, \downarrow$, and $g > 0$. $l_{0,\mu}$ denotes an interaction length along the μ direction. $\psi^{\dagger}_{\sigma}(\boldsymbol{r}, c)$ denotes the electron creation at π orbital π_c ($c = A, A', B, B'$) of a carbon atom at $\boldsymbol{r}$ with spin σ. The creation field can be expanded in

terms of single-particle bases of the $n = 0$ and $n = -1$ LLs in the Landau gauge:

$$\begin{pmatrix} \psi_\sigma(\boldsymbol{r}, A) \\ \psi_\sigma(\boldsymbol{r}, A') \\ \psi_\sigma(\boldsymbol{r}, B) \\ \psi_\sigma(\boldsymbol{r}, B') \end{pmatrix} = \sum_j \frac{e^{ik_j x}}{\sqrt{L_x}} \sum_{\tau=\pm} \left\{ \begin{pmatrix} \gamma_{A,\sigma} Y_{0,j}(y) \\ \gamma_{A',\sigma} Y_{0,j}(y) \\ \gamma_{B,\sigma} Y_{1,j}(y) \\ \gamma_{B',\sigma} Y_{1,j}(y) \end{pmatrix} e^{i\tau k_{F,0,\sigma} z} \psi_{(0,\sigma),\tau,j}(z) + \begin{pmatrix} 0 \\ 0 \\ \eta_{B,\sigma} Y_{0,j}(y) \\ \eta_{B',\sigma} Y_{0,j}(y) \end{pmatrix} e^{i\tau k_{F,-1,\sigma} z} \psi_{(-1,\sigma),\tau,j}(z) \right\}, \quad (8)$$

where

$$Y_{0,j}(y) \equiv \frac{1}{\sqrt{\sqrt{\pi} l}} e^{-\frac{(y-y_j)^2}{2l^2}}, \qquad (9)$$

$$Y_{1,j}(y) \equiv \sqrt{2} l \frac{d}{dy_j} Y_{0,j}(y) = \frac{\sqrt{2}(y-y_j)}{\sqrt{\sqrt{\pi} l^3}} e^{-\frac{(y-y_j)^2}{2l^2}}, \quad (10)$$

with $y_j \equiv k_j l^2$ and $k_j \equiv 2\pi j/L_x$. The slowly varying field $\psi_{(n,\sigma),\tau,j}(z) \equiv \psi_{a,\tau,j}(z)$ was defined in Eq. (5) with $a \equiv (n, \sigma)$. $\gamma_{c,\sigma}$ ($c = A, A', B, B'$) comprises an eigenvector of a 4×4 SWM (Slonczewski-Weiss-McClure) Hamiltonian at $k_z = \pm k_{F,0,\sigma}$ [30–34]. $\eta_{c,\sigma}$ ($c = B, B'$) comprises the eigenvector at $k_z = \pm k_{F,-1,\sigma}$. L_x is the linear dimension of the system size along the x direction. A substitution of Eqs. (8)–(10) into Eq. (6) and expansion in $\psi_{(n,\sigma),\tau,j}(z) \equiv \psi_{a,j}(z)$ lead to scatterings between different pockets (interpocket scattering) and scatterings within the same pocket (intrapocket scattering).

In this paper, we take into consideration only umklapp scattering terms that are allowed under the charge neutrality condition (Fig. 3), interpocket scattering terms between *opposite* chiralities (Fig. 4), and intrapocket scatterings H_f. This is because, in fermionic functional renormalization group analyses [12,41,42], these scatterings are coupled with one

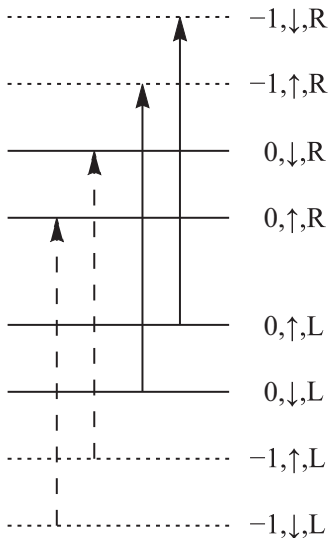
FIG. 3. Schematic pictures of one of the umklapp scatterings, $H_{u,2}$. As in Fig. 2, the vertical axis denotes the momentum along the field direction (k_z), while the horizontal axis denotes the chain index $y_j = k_j l^2$ with $k_j \equiv 2\pi j/L_x$ [$j = 1, 2, \dots, L_x L_y/(2\pi l^2)$]. The two-particle scatterings with solid/dotted arrows are the exchange processes ($m = n$) of the first/fourth terms in Eq. (11) with $(0, \uparrow) \equiv 1, (0, \downarrow) \equiv 2, (-1, \uparrow) \equiv 3$, and $(-1, \downarrow) \equiv 4$.

another at the one-loop level; they have larger chances to become relevant upon renormalization than those scattering terms omitted.

Under the charge neutrality condition [Eq. (3)], the interaction allows the following four umklapp terms and their Hermitian conjugates:

$$H_u = \sum_{j,m,n} \begin{cases} \psi^\dagger_{4,+,n} \psi^\dagger_{3,+,j+m-n} \psi_{1,-,m} \psi_{2,-,j}, \\ \psi^\dagger_{2,+,n} \psi^\dagger_{3,+,j+m-n} \psi_{1,-,m} \psi_{4,-,j}, \\ \psi^\dagger_{4,+,n} \psi^\dagger_{1,+,j+m-n} \psi_{3,-,m} \psi_{2,-,j}, \\ \psi^\dagger_{2,+,n} \psi^\dagger_{1,+,j+m-n} \psi_{3,-,m} \psi_{4,-,j}. \end{cases} \quad (11)$$

Due to the translational symmetry along x in the Landau gauge, the scattering processes conserve a momentum $k_j \equiv 2\pi j/L_x$ that is conjugate to x. In Eq. (11), integrals over the spatial coordinate z and the scattering matrix elements that depend on z and $j, m, n = 1, 2, \dots, (L_x L_y)/(2\pi l^2)$ are omitted for clarity. For example, the first and fourth terms in Eq. (11) take the following explicit form with their Hermitian conjugates:

[1st and 4th terms in Eq. (11)]

$$= 2 \sum_{j,m,n} V^{(12)}_{m-n,j-n} \int dz \int dz' \, e^{-\frac{(z-z')^2}{2l_{0,z}^2}}$$

$$\times \{ e^{-ik_{F,3}z - ik_{F,4}z' - ik_{F,2}z' - ik_{F,1}z}$$

$$\times (\psi^\dagger_{4,+,n} \psi^\dagger_{3,+,j+m-n} \psi_{1,-,m} \psi_{2,-,j}$$

$$+ \psi^\dagger_{2,+,n} \psi^\dagger_{1,+,j+m-n} \psi_{3,-,m} \psi_{4,-,j}) + \text{H.c.}\}. \quad (12)$$

The matrix elements in Eq. (12) are given by a dimensionless function $f^{(12)}(x, y)$ as

$$V^{(12)}_{m,n} \equiv \frac{g}{L_x} \frac{1}{2\pi l_{0,z} l} f^{(12)}(y_m/l, y_n/l). \quad (13)$$

The function $f^{(12)}(x, y)$ can be calculated by the direct substitution of Eqs. (7)–(10) into Eq. (6). g is from Eq. (7).

In addition to H_u, we consider the interpocket scatterings between the *opposite* chirality (H_b) as well as the intrapocket scatterings (H_f). They are

$$H_b = \sum_{j,m,n} \begin{cases} \psi^\dagger_{4,\pm,n} \psi^\dagger_{1,\mp,j+m-n} \psi_{1,\mp,m} \psi_{4,\pm,j}, \\ \psi^\dagger_{3,\pm,n} \psi^\dagger_{2,\mp,j+m-n} \psi_{2,\mp,m} \psi_{3,\pm,j}, \\ \psi^\dagger_{4,\pm,n} \psi^\dagger_{2,\mp,j+m-n} \psi_{2,\mp,m} \psi_{4,\pm,j}, \\ \psi^\dagger_{3,\pm,n} \psi^\dagger_{1,\mp,j+m-n} \psi_{1,\mp,m} \psi_{3,\pm,j}, \\ \psi^\dagger_{4,\pm,n} \psi^\dagger_{3,\mp,j+m-n} \psi_{3,\mp,m} \psi_{4,\pm,j}, \\ \psi^\dagger_{2,\pm,n} \psi^\dagger_{1,\mp,j+m-n} \psi_{1,\mp,m} \psi_{2,\pm,j}, \end{cases} \quad (14)$$

and

$$H_{\mathrm{f}} = \sum_a \sum_{j,m,n} \psi_{a,n}^\dagger \psi_{a,j+m-n}^\dagger \psi_{a,m} \psi_{a,j}, \qquad (15)$$

with $\quad \psi_{a,n}(z) \equiv e^{ik_{F,a}z}\psi_{a,+,n}(z) + e^{-ik_{F,a}z}\psi_{a,-,n}(z) \quad [a = 1, 2, 3, 4;$ see Eq. (B1) for an actual form of H_{f}]. We do not take into account the interpocket scatterings between the *same* chirality, because, at the one-loop level of the fermionic renormalization group equations [12,41,42], they are decoupled from H_{u}, H_{b}, and H_{f}, and do not grow into larger values upon the renormalization.

IV. EFFECTIVE BOSON THEORY

In this section, we construct effective field theories of possible insulating phases that are stabilized by the umklapp scattering terms in Eq. (11). To this end, we first assume that the low-T insulating phases in the graphite experiment do not break the translational symmetries within the graphene plane [the graphene plane is perpendicular to the field (z)]. The assumption apparently does not contradict any experimental observations in the literature [1,2,5,6,13–21]. We thus introduce as "mean fields" the pairings among electron creation/annihilation operators *within the same chain*, and treat the interchain electron-electron interactions within a Hartree-Fock approximation. To be more specific, we keep only the direct process (Hartree term: $j = n$) and exchange process (Fock term: $m = n$) in Eqs. (11), (14), and (15). Within such effective theory framework, the metal-insulator transitions in the graphite experiment are described by a phase transition between a phase with the mean fields being zero and a phase with the mean fields being finite. The former phase corresponds to the high-T normal metal phase and the latter corresponds to the low-T insulating phases.

To do this construction transparently, we first bosonize the slowly varying fermion field in terms of two phase variables defined for each pocket $a = (n, \sigma)$ and each chain $j = 1, \ldots, (L_x L_y)/(2\pi l^2)$ [25,43]:

$$\psi_{a,+,j}(z) \equiv \frac{\eta_{a,j}}{\sqrt{2\pi\alpha}} e^{-i[\phi_{a,j}(z)-\theta_{a,j}(z)]},$$
$$\psi_{a,-,j}(z) \equiv \frac{\eta_{\bar{a},j}}{\sqrt{2\pi\alpha}} e^{-i[-\phi_{a,j}(z)-\theta_{a,j}(z)]}. \qquad (16)$$

Here $(n, \sigma) = (0, \uparrow), (0, \downarrow), (-1, \uparrow),$ and $(-1, \downarrow)$ are abbreviated as $a = 1, 2, 3,$ and 4, respectively. α is a short-range cutoff for the spatial coordinate z. $\phi_{a,j}(z)$, $\theta_{a,j}(z)$, and $\partial_z\theta_{a,j}(z)$ are the displacement field along the field direction (z), superconducting phase field, and current density field along the field, respectively. They are associated with the pocket a and the jth chain. The displacement field and superconducting phase field cannot be simultaneously definite; they are canonically conjugate to each other:

$$[\phi_{a,j}(z), \partial_{z'}\theta_{b,m}(z')] = i\delta_{a,b}\delta_{j,m}\delta(z - z'). \qquad (17)$$

$\eta_{a,j}$ and $\eta_{\bar{a},j}$ in Eq. (16) are Klein factors ensuring the anticommutation relation among fermion fields on different chains (j), pockets (a), and chiralities ($\tau = \pm$); $\{\eta_{a,j}, \eta_{b,m}\} = \{\eta_{\bar{a},j}, \eta_{\bar{b},m}\} = \delta_{a,b}\delta_{j,m}$, and $\{\eta_{a,j}, \eta_{\bar{b},m}\} = 0$. Due to the Klein factor, the interaction parts given in Eqs. (11), (14), and (15) cannot be fully bosonized without approximation.

To obtain the effective boson theories of the insulating phases, we thus employ the Hartree-Fock approximation for the interchain interactions in Eqs. (11), (14), and (15), to keep only the direct process ($j = n$) and exchange process ($m = n$) in Eqs. (11), (14), and (15). This leads to a fully bosonized Hamiltonian

$$H_{\mathrm{kin}} + H_{\mathrm{u}} + H_{\mathrm{b}} + H_{\mathrm{f}} = H_0 + \sum_{i=1}^4 H_{\mathrm{u},i} + \sum_{i=1}^4 H_{\mathrm{b},i} + \cdots, \qquad (18)$$

$$H_0 = \sum_m \sum_{a=1}^4 \int dz \left\{ \frac{u_a K_a \pi}{2} [\Pi_{a,m}(z)]^2 + \frac{u_a}{2\pi K_a} [\partial_z \phi_{a,m}(z)]^2 \right\}, \qquad (19)$$

and $\pi\Pi_{a,j}(z) \equiv \partial_z\theta_{a,j}(z)$. K_a and u_a are the Luttinger parameter and Fermi velocity of a pocket with $a = (n, \sigma)$ that are renormalized by the intrapocket forward scatterings H_{f} (see Appendix B for details). As in the standard bosonization, the renormalizations are given by two parameters $g_{2,a}$ (> 0) and $g_{4,a}$ (> 0) as

$$\frac{u_a}{v_{F,a}} = \sqrt{\left(1 + \frac{g_{4,a}}{2\pi v_{F,a}}\right)^2 - \left(\frac{g_{2,a}}{2\pi v_{F,a}}\right)^2}, \qquad (20)$$

$$K_a = \sqrt{\frac{2\pi v_{F,a} + g_{4,a} - g_{2,a}}{2\pi v_{F,a} + g_{4,a} + g_{2,a}}}. \qquad (21)$$

See also Appendix B for expressions of $g_{2,a}$ and $g_{4,a}$ in terms of g in Eq. (7). The Hartree and Fock terms in the umklapp scatterings of Eq. (11) are bosonized as

$$H_{\mathrm{u},1} = \sum_{j,m} M_{j-m}^{(1)} \int dz \{ \sigma_{3\bar{1},j}\sigma_{4\bar{2},m} \cos[Q_{+,j}^{13} + Q_{+,m}^{24}] + \sigma_{\bar{3}1,j}\sigma_{\bar{4}2,m} \cos[Q_{-,j}^{13} + Q_{-,m}^{24}] \}, \qquad (22)$$

$$H_{\mathrm{u},2} = \sum_{j,m} M_{j-m}^{(2)} \int dz \{ \sigma_{3\bar{2},j}\sigma_{4\bar{1},m} \cos[Q_{+,j}^{23} + Q_{+,m}^{14}] + \sigma_{\bar{3}2,j}\sigma_{\bar{4}1,m} \cos[Q_{-,j}^{23} + Q_{-,m}^{14}] \}, \qquad (23)$$

$$H_{\mathrm{u},3} = \sum_{j,m} M_{j-m}^{(3)} \int dz \{ \sigma_{3\bar{1},j}\sigma_{2\bar{4},m} \cos[Q_{+,j}^{13} + Q_{-,m}^{24}] + \sigma_{\bar{3}1,j}\sigma_{\bar{2}4,m} \cos[Q_{-,j}^{13} + Q_{+,m}^{24}] \}, \qquad (24)$$

$$H_{\mathrm{u},4} = \sum_{j,m} M_{j-m}^{(4)} \int dz \{ \sigma_{3\bar{4},j}\sigma_{2\bar{1},m} \cos[Q_{-,j}^{34} + Q_{+,m}^{12}] + \sigma_{\bar{3}4,j}\sigma_{\bar{2}1,m} \cos[Q_{+,j}^{34} + Q_{-,m}^{12}] \}, \qquad (25)$$

where

$$Q_{\pm,j}^{ab} \equiv \phi_{a,j} + \phi_{b,j} \pm (\theta_{a,j} - \theta_{b,j}), \qquad (26)$$

with $a, b = 1, 2, 3, 4$. $\sigma_{a\bar{b},j}$ and $\sigma_{\bar{a}b,m}$ are Ising variables associated with the Klein factors within the same chain, $\sigma_{a\bar{b},j} \equiv i\eta_{a,j}\eta_{\bar{b},j}$, and $\sigma_{\bar{a}b,m} \equiv i\eta_{\bar{a},m}\eta_{b,m}$. The Ising variables take ± 1.

The Fock term ($m = n$) of the interpocket scatterings, Eq. (14), is bosonized as

$$H_{b,13} = \sum_{j,m} H_{j-m}^{(13)} \int dz \{\sigma_{3\bar{1},j}\sigma_{3\bar{1},m} \cos[\Delta_{jm}Q_+^{13}]$$

$$+ \sigma_{\bar{3}1,j}\sigma_{\bar{3}1,m} \cos[\Delta_{jm}Q_-^{13}]\}$$

$$+ \sum_{j,m} \overline{H}_{j-m}^{(13)} \int dz \{\sigma_{4\bar{2},j}\sigma_{4\bar{2},m} \cos[\Delta_{jm}Q_+^{24}]$$

$$+ \sigma_{\bar{4}2,j}\sigma_{\bar{4}2,m} \cos[\Delta_{jm}Q_-^{24}]\}, \quad (27)$$

$$H_{b,2} = \sum_{j,m} H_{j-m}^{(2)} \int dz \{\sigma_{3\bar{2},j}\sigma_{3\bar{2},m} \cos[\Delta_{jm}Q_+^{23}]$$

$$+ \sigma_{\bar{3}2,j}\sigma_{\bar{3}2,m} \cos[\Delta_{jm}Q_-^{23}]\}$$

$$+ \sum_{j,m} \overline{H}_{j-m}^{(2)} \int dz \{\sigma_{4\bar{1},j}\sigma_{4\bar{1},m} \cos[\Delta_{jm}Q_+^{14}]$$

$$+ \sigma_{\bar{4}1,j}\sigma_{\bar{4}1,m} \cos[\Delta_{jm}Q_-^{14}]\}, \quad (28)$$

$$H_{b,4} = \sum_{j,m} H_{j-m}^{(4)} \int dz \{\sigma_{3\bar{4},j}\sigma_{3\bar{4},m} \cos[\Delta_{jm}Q_-^{34}]$$

$$+ \sigma_{\bar{3}4,j}\sigma_{\bar{3}4,m} \cos[\Delta_{jm}Q_+^{34}]\}$$

$$+ \sum_{j,m} \overline{H}_{j-m}^{(4)} \int dz \{\sigma_{2\bar{1},j}\sigma_{2\bar{1},m} \cos[\Delta_{jm}Q_+^{12}]$$

$$+ \sigma_{\bar{2}1,j}\sigma_{\bar{2}1,m} \cos[\Delta_{jm}Q_-^{12}]\}, \quad (29)$$

with $\Delta_{jm}f \equiv f_j - f_m$. The Hartree term ($j = n$) of the interpocket scatterings in Eq. (14) could also renormalize the Luttinger parameters and Fermi velocities. For simplicity, however, we consider the renormalizations of K_a and u_a only by the intrapocket scatterings H_f as given in Appendix B. Figures 3 and 4 schematically show the interpocket scattering processes that lead to $H_{u,2}$ and $H_{b,2}$, respectively.

The interchain interactions in $H_{u,i}$ and $H_{b,i}$ range over the magnetic length:

$$M_{j-m}^{(n)} \equiv \frac{g}{L_x \alpha^2 l} \mathcal{M}^{(n)}((y_j - y_m)/l), \quad (30)$$

$$H_{j-m}^{(n)} \equiv \frac{g}{L_x \alpha^2 l} \mathcal{H}^{(n)}((y_j - y_m)/l), \quad (31)$$

$$\overline{H}_{j-m}^{(n)} \equiv \frac{g}{L_x \alpha^2 l} \overline{\mathcal{H}}^{(n)}((y_j - y_m)/l), \quad (32)$$

with $n = 1, 2, 3, 4,$ and 13. $\mathcal{M}(y)$ and $\mathcal{H}(y)$ as well as $\overline{\mathcal{H}}(y)$ are dimensionless functions. For example, Eqs. (22), (23), and (30) are obtained from the direct ($j = n$) and exchange processes ($m = n$) of Eq. (12), respectively, with

$$\mathcal{M}^{(1)}(x) = -e^{-\frac{1}{8}(k_{F,1}+k_{F,3}-k_{F,2}-k_{F,4})^2 l_{0,z}^2} \frac{f^{(12)}(x,0)}{\sqrt{2\pi}\pi^2}, \quad (33)$$

$$\mathcal{M}^{(2)}(x) = e^{-\frac{1}{8}(k_{F,2}+k_{F,3}-k_{F,1}-k_{F,4})^2 l_{0,z}^2} \frac{f^{(12)}(0,x)}{\sqrt{2\pi}\pi^2}. \quad (34)$$

For the repulsive interaction case ($g > 0$), integrals of Eqs. (31) and (32) over $y \equiv (y_j - y_m)/l$ give negative values for any $n = 13, 2, 4$.
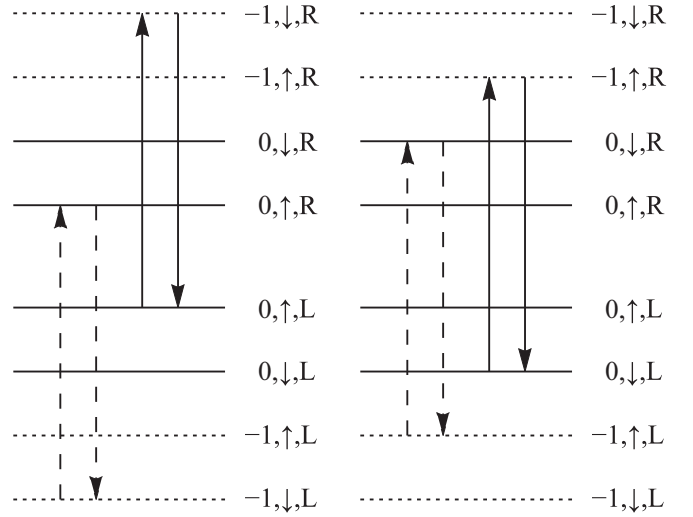

FIG. 4. Schematic pictures of one of the interpocket scatterings, $H_{b,2}$. They are the exchange processes ($m = n$) of the first two terms in Eq. (14) with $(0, \uparrow) \equiv 1$, $(0, \downarrow) \equiv 2$, $(-1, \uparrow) \equiv 3$, and $(-1, \downarrow) \equiv 4$. As in Fig. 2, the vertical axis denotes the momentum along the field direction (k_z), while the horizontal axis denotes the chain index $y_j = k_j l^2$ with $k_j \equiv 2\pi j/L_x$ [$j = 1, 2, \ldots, L_x L_y/(2\pi l^2)$].

In the next section, we will use a perturbative renormalization group (RG) analysis on the effective boson model, $H_0 + \sum_i H_{u,i} + \sum_i H_{b,i}$, where $H_{u,i}$ and $H_{b,i}$ are treated perturbatively (Appendix C). We show that, at the one-loop level of the perturbative RG equations, $H_{b,13}$, $H_{u,1}$, and $H_{u,3}$ are coupled with one another and stabilize (what we call) the plain excitonic insulator phase. Meanwhile, $H_{u,2}$ and $H_{b,2}$ stabilize the spin nematic excitonic insulator phase, and $H_{u,4}$ and $H_{b,4}$ stabilize the magnetic Mott insulator phase.

V. RENORMALIZATION GROUP ANALYSES

A. Spin nematic excitonic insulator (SNEI-I) phase

We begin with the spin nematic excitonic insulator phase stabilized by $H_{b,2}$ and $H_{u,2}$. The RG equations for the interchain interaction functions in $H_{b,2}$ and $H_{u,2}$ take following forms at the one-loop level:

$$\frac{dM_{j-m}^{(2)}}{d\ln b} = \frac{A_{23} + A_{14}}{2} M_{j-m}^{(2)} - 2C_{23} \sum_n M_{j-n}^{(2)} H_{n-m}^{(2)}$$

$$- 2C_{14} \sum_n M_{j-n}^{(2)} \overline{H}_{n-m}^{(2)}, \quad (35)$$

$$\frac{dH_{j-m}^{(2)}}{d\ln b} = A_{23} H_{j-m}^{(2)} - \frac{1}{2} \sum_n \left(C_{14} M_{j-n}^{(2)} M_{n-m}^{(2)} + 4C_{23} H_{j-n}^{(2)} H_{n-m}^{(2)}\right), \quad (36)$$

$$\frac{d\overline{H}_{j-m}^{(2)}}{d\ln b} = A_{14} \overline{H}_{j-m}^{(2)} - \frac{1}{2} \sum_n \left(C_{23} M_{j-n}^{(2)} M_{n-m}^{(2)} + 4C_{14} \overline{H}_{j-n}^{(2)} \overline{H}_{n-m}^{(2)}\right). \quad (37)$$

Here $\ln b > 0$ is a scale change of the RG equations (see Appendix C for their derivations). The temperature T increases monotonically on renormalization; $dT/d\ln b = T$. A_{23}, A_{14}, and their linear combination are the scaling dimensions of H_{j-m}, $\overline{H}_{j-m}$, and M_{j-m} at the tree-loop level:

$$A_{ab} \equiv 2 - \frac{1}{2}\sum_{c=a,b}\left(K_c + K_c^{-1}\right)\coth\left(\frac{u_c\Lambda}{2T}\right) < 0. \quad (38)$$

$a, b = 1, 2, 3, 4$ are the pocket indices, where $1 \equiv (0,\uparrow)$, $2 \equiv (0,\downarrow)$, $3 \equiv (-1,\uparrow)$, and $4 \equiv (-1,\downarrow)$. Λ is a short-range cutoff in the momentum space, $\Lambda = \alpha^{-1}$. C_{ab} in Eqs. (35)–(37) is always a finite positive definite constant for any $a, b = 1, 2, 3, 4$ (see Appendix C3). We assume that C_{ab} has no dependence on temperature and magnetic field. Equations (35)–(37) are functional RG equations under which interchain interactions change their functional forms. To gain a simpler idea of these functional RG equations, we take a sum of the interchain interactions over their chain indices. The sum reduces the interchain coupling *functions* into coupling *constants* as follows:

$$m_{(2)} \equiv 2\pi l^2 \sum_j M_j^{(2)} = \frac{g}{\alpha^2}\int \mathcal{M}^{(2)}(y)dy, \quad (39)$$

$$h_{(2)} \equiv 2\pi l^2 \sum_j H_j^{(2)} = \frac{g}{\alpha^2}\int \mathcal{H}^{(2)}(y)dy < 0, \quad (40)$$

$$\overline{h}_{(2)} \equiv 2\pi l^2 \sum_j \overline{H}_j^{(2)} = \frac{g}{\alpha^2}\int \overline{\mathcal{H}}^{(2)}(y)dy < 0. \quad (41)$$

As mentioned above, the inequalities in Eqs. (40) and (41) hold true for the repulsive interaction case. Considering the repulsive interaction case, we assume the negative bare values of $h_{(2)}$ and $\overline{h}_{(2)}$ in the following.

The RG equations for the coupling constants take forms of

$$\frac{dm_{(2)}}{d\ln b} = \frac{A_{23}+A_{14}}{2}m_{(2)} - \frac{1}{\pi l^2}m_{(2)}(C_{23}h_{(2)}+C_{14}\overline{h}_{(2)}), \quad (42)$$

$$\frac{dh_{(2)}}{d\ln b} = A_{23}h_{(2)} - \frac{1}{4\pi l^2}\left(C_{14}m_{(2)}^2 + 4C_{23}h_{(2)}^2\right), \quad (43)$$

$$\frac{d\overline{h}_{(2)}}{d\ln b} = A_{14}\overline{h}_{(2)} - \frac{1}{4\pi l^2}\left(C_{23}m_{(2)}^2 + 4C_{14}\overline{h}_{(2)}^2\right). \quad (44)$$

The equations dictate that the umklapp term as well as the interchain backward scattering are irrelevant at the tree-loop level, as A_{ab} is negative semidefinite [Eq. (38)]. Smaller $m_{(2)}$, $h_{(2)}$, and $\overline{h}_{(2)}$ are always renormalized into zero ("weak-coupling phase"; normal metal phase).

C_{ab} is positive definite. Thus, the bare repulsive interaction g has a critical strength, above which $m_{(2)}$, $h_{(2)}$, and $\overline{h}_{(2)}$ help one another to grow into larger values ("strong-coupling phase"). The critical strength decreases not only on increasing the magnetic field through a dependence of the one-loop terms on the magnetic length l, but also on decreasing the temperature through a dependence of A_{ab} on the temperature. This suggests that the strong-coupling phase generally appears on the low-temperature side and the transition temperature of the strong-coupling phase increases in larger magnetic field (e.g., see the field dependence of the transition temperature of the SNEI-I phase in Fig. 1 in the region $H < 40$ T).

The transition temperature can also *decrease* when the Luttinger parameters K_a ($a = 1,\dots,4$) deviate largely from the unit. $|A_{ab}|$ has a global minimum at $K_a = K_b = 1$ and $T = 0$. When K_a deviates away from 1, A_{ab} becomes negatively larger and thus the critical strength of g increases; the transition temperature decreases. Physically speaking, K_a being greater/smaller than the unit means stronger quantum fluctuation of the displacement field/superconducting phase field of the ath pocket [Eqs. (19) and (17)]. The enhanced quantum fluctuations generally destabilize the strong-coupling phase.

This observation readily lets us propose a microscopic mechanism for the reentrant transition from the strong-coupling to weak-coupling phases: the transition induced by *raising* the magnetic field. The higher magnetic field generally makes the electron pocket (a) and hole pocket (b) smaller in size in the k_z space. This makes their bare Fermi velocities, $v_{F,a}$, $v_{F,b}$, smaller with respect to the electron interaction energy scale. Thus, in the presence of the repulsive interaction, $g_{2,a}, g_{2,b} > 0$ in Eq. (21), the smaller Fermi velocities make their Luttinger parameters smaller than the unit, $K_a, K_b < 1$. Especially, for $H < H_0$, K_1 and K_4 are expected to be much smaller than the unit near $H = H_0$, where the electron pocket with $a = 1$ [$(n,\sigma) = (0,\uparrow)$] and the hole pocket with $b = 4$ [$(n,\sigma) = (-1,\downarrow)$] are about to leave the Fermi level. Thus, the transition temperature of the strong-coupling phase reduces dramatically near $H = H_0$ through an enhancement of K_1^{-1} and K_4^{-1} in Eq. (38) (e.g., see the field dependence of T_c of the SNEI-I phase in Fig. 1 in the region 40 T $< H < 50$ T). Physically speaking, this reduction is nothing but a consequence of the enhanced quantum fluctuation of the spin superconducting phase variable.

When the bare repulsive interaction is greater than the critical value (strong-coupling phase), the umklapp and interpocket backward scattering terms grow into larger values:

$$h_{(2)}, \overline{h}_{(2)} \to -\infty, \quad m_{(2)} \to \pm\infty.$$

The following argument does not depend on the sign of $m_{(2)}$, so that we set $m_{(2)} > 0$ henceforth. In the strong-coupling regime, $H_{u,2}$ and $H_{b,2}$ are maximally minimized by

$$\phi_{3,m} + \phi_{2,m} = \Phi_-, \quad \phi_{4,m} + \phi_{1,m} = \begin{cases} 2n\pi - \Phi_-, \\ (2n+1)\pi - \Phi_-, \end{cases} \quad (45)$$

$$\theta_{3,m} - \theta_{2,m} = \Theta_-, \quad \theta_{4,m} - \theta_{1,m} = \begin{cases} (2n+1)\pi - \Theta_-, \\ 2n\pi - \Theta_-, \end{cases} \quad (46)$$

with

$$\sigma_{3\overline{2},m} = \sigma_{4\overline{1},m} = \sigma_{\overline{3}2,m} = \sigma_{\overline{4}1,m} = \sigma. \quad (47)$$

The locking of the total displacement field, $\phi_{3,m} + \phi_{2,m} + \phi_{4,m} + \phi_{1,m} = 2n\pi$ or $(2n+1)\pi$, dictates that the system is electrically insulating along the field direction. Meanwhile, any electron densities, $\langle\rho(\mathbf{r},c)\rangle \equiv \sum_{\sigma=\uparrow,\downarrow}\langle\psi_\sigma^\dagger(\mathbf{r},c)\psi_\sigma(\mathbf{r},c)\rangle$ with $c = A, A', B, B'$, do not break the translational symmetry along the field direction (z), because

$$\langle\psi_{(n,\sigma),\tau,j}^\dagger(z)\psi_{(n,\sigma),\overline{\tau},j}(z)\rangle = 0,$$

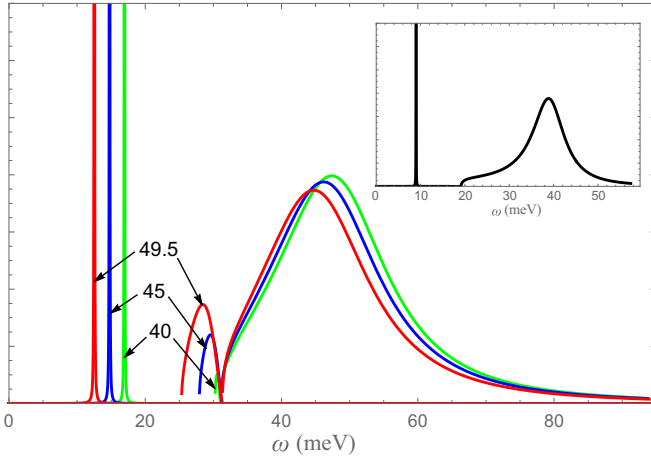$$\langle\psi_{(0,\sigma),\tau,j}^\dagger(z)\psi_{(-1,\sigma),\tau',j}(z)\rangle = 0,$$

FIG. 5. Theoretical calculation results of the optical conductivity $\sigma_{zz}(\omega)$ in the SNEI-I phase ($H = 40$, 45, 49.5 T). Inset: $\sigma_{zz}(\omega)$ in the SNEI-II phase ($H = 55$ T). We use the same parameter sets as in Fig. 1. For details, see Appendix D. Unlike its appearance in the figures, the delta function at $\omega = \omega_*$ is the most prominent in amplitude, while the continuum spectrum is much less significant. The renormalized gap ω_* is on the order of $\sqrt{E_{int} E_{bw}}$, where E_{int} is an interaction energy scale, $E_{int} \sim e^2/(\epsilon l)$, and E_{bw} is a bandwidth energy scale (see Appendix C4).

with $n = 0, -1$, $\tau, \tau' = \pm$, $\bar{\tau} = -\tau$, $\sigma = \uparrow, \downarrow$. Due to the charge neutrality condition, the mean electron density is 2 per two LLs, $n = 0$ and $n = -1$ LLs, and per the unit cell along the c axis. Besides, the insulating phase is associated with particle-hole pairings between the $n = 0$ LL (electron pocket) and $n = -1$ LL (hole pocket). Thus, we regard this phase as an excitonic insulator [18,20,41,42,44,45] instead of charge density wave phase.

An insulating property is manifested by the optical conductivity along the c axis, $\sigma_{zz}(\omega)$ (Fig. 5). In the strong-coupling phase with large $m_{(2)}$, we may employ a Gaussian approximation for the cosine terms in $H_{u,2}$. $\sigma_{zz}(\omega)$ is calculated within the linear response theory as $\sigma_{zz}(\omega) = (e^2 uK)/(2\pi l^2)\delta(\omega - \omega_g)$, where $uK \equiv \sum_a u_a K_a$. $\omega_g^2 \equiv 2\pi uK \sum_j M_j^{(2)}$ defines a gap for collective particle-hole excitation associated with a fluctuation of the total displacement field. An inclusion of a short-ranged dielectric disorder renormalizes the gap into a smaller value ω_* with a smaller spectral weight for the delta function (see Appendix D). Meanwhile, it adds a continuum spectrum in higher-energy regions. The continuum spectra compensate the reduced spectral weight of the delta function. The observation concludes that the excitonic insulator phase is robust against any small dielectric disorder, provided that the renormalized gap size and the spectral weight of the delta function remain finite (see Appendix D).

The long-range order of the spin superconducting phases such as $\theta_3 - \theta_2$, $\theta_4 - \theta_1$ in Eq. (46) breaks the U(1) spin rotational symmetry around the field direction. The breaking of the continuous spin rotational symmetry is manifested by a long-range ordering of spin quadrupole moment ("spin nematic excitonic insulator"). The quadrupole moment that exhibits the order is the symmetric part of the 2nd-rank spin tensor composed of two spin-1/2 moments (see Appendix E).

One spin-1/2 is from the π orbital of the A or A' carbon atom, while the other spin-1/2 is from the π orbital of the B or B' carbon atom. The 2nd-rank spin tensor is defined as

$$Q_{\mu\nu}^{cd}(\boldsymbol{r}) \equiv \langle S_{c,\mu}(\boldsymbol{r}) S_{d,\nu}(\boldsymbol{r}) + S_{c,\nu}(\boldsymbol{r}) S_{d,\mu}(\boldsymbol{r}) \rangle$$
$$- \delta_{\mu\nu} \langle \boldsymbol{S}_{c,\perp}(\boldsymbol{r}) \cdot \boldsymbol{S}_{d,\perp}(\boldsymbol{r}) \rangle, \quad (48)$$

with $c = A, A'$, $d = B, B'$, $\mu, \nu = x, y$, $\boldsymbol{S}_{c,\perp} \equiv (S_{c,x}, S_{c,y})$, $2S_{c,\mu}(\boldsymbol{r}) \equiv \psi_{\sigma'}^{\dagger}(\boldsymbol{r}, c)[\sigma_\mu]_{\sigma'\sigma''}\psi_{\sigma''}(\boldsymbol{r}, c)$, and $\sigma', \sigma'' = \uparrow, \downarrow$. The order of the spin superconducting phase [Eq. (46)] leads to a ferro-type as well as density-wave-type ordering of the 2nd-rank spin tensor, e.g.,

$$Q_{xx}^{AB}(\boldsymbol{r}) + i Q_{xy}^{AB}(\boldsymbol{r}) = e^{2i\Theta_-}[u + u\cos(\Delta K z - 2\Phi_-)],$$

where $\Delta K \equiv k_{F,3} + k_{F,2} - k_{F,4} - k_{F,1}$. u is a complex-valued coefficient. Symmetry-wise, the long-range order given in Eq. (46) can be also accompanied by a helical magnetic order whose magnetic moment lies in the xy plane. The helical order has two spatial pitches along the c axis, $(2\pi)/(k_{F,3} + k_{F,2})$ and $(2\pi)/(k_{F,1} + k_{F,4})$. Microscopically speaking, however, an amplitude of the magnetic moment is tiny and, if any, it appears only in those spatial regions in the cell where two neighboring π orbitals in the same graphene layer overlap (Appendix E).

On increasing the magnetic field, the outer electron pocket with $(n, \sigma) = (0, \uparrow)$ and hole pocket with $(-1, \downarrow)$ leave the Fermi level at $H = H_0$. *Ab initio* electronic band structure calculations evaluate H_0 around 53 T [8]. For $H \to H_0$ ($H < H_0$), the bare Fermi velocities of the two pockets $v_{F,1}$ and $v_{F,4}$ become smaller. So do the Luttinger parameters of the two pockets K_1 and K_4 [Eq. (21)]. The reduction of the Luttinger parameters makes the tree-level scaling dimension A_{14} negatively very large [Eq. (38)]. Thus, according to Eqs. (42), (44), $m_{(2)}$ and $\bar{h}_{(2)}$ are renormalized into smaller values at an early stage of the RG flow for $H \lesssim H_0$, irrespective of bare values of $m_{(2)}$ and $\bar{h}_{(2)}$. Meanwhile, A_{23} as well as $v_{F,2}$ and $v_{F,3}$ remain rather constant around $H = H_0$. Thus, according to Eq. (43), $h_{(2)}$ grows to a larger value and eventually diverges, provided that its bare (initial) value is greater than a critical value (see below for the critical value). Larger $h_{(2)}$ then helps $m_{(2)}$ and $\bar{h}_{(2)}$ grow at a late stage of the RG flow, by way of the one-loop terms in Eqs. (42), (44). The argument so far concludes that, for $H \lesssim H_0$, the transition temperature of the strong-coupling phase is determined only by Eq. (43) with $m_{(2)} = 0$:

$$\frac{dh_{(2)}}{d\ln b} = A_{23} h_{(2)} - \frac{C_{23}}{\pi l^2} h_{(2)}^2. \quad (49)$$

At zero temperature, Eq. (49) gives the critical value for $h_{(2)}$ as

$$h_{(2),c} \equiv \frac{\pi l^2}{C_{23}}(A_{23})|_{T=0} = \frac{\pi l^2}{C_{23}}\left[2 - \sum_{c=2,3}\left(K_c + K_c^{-1}\right)\right] < 0. \quad (50)$$

When $h_{(2)} < h_{(2),c} < 0$, the spin nematic excitonic insulator phase always appears below a finite critical temperature T_c at $H \leqslant H_0$ (Fig. 3). The situation is consistent with the experimental phase diagram of graphite under high field. Meanwhile, RG phase diagrams of the other insulators stabilized

by $H_{u,1}$, $H_{u,3}$, or $H_{u,4}$ are not consistent with the graphite experiment.

B. Magnetic Mott insulator and plain excitonic insulator phases

To see this, let us next consider the nature and the RG phase diagram of the magnetic Mott insulator phase stabilized by $H_{u,4}$ and $H_{b,4}$. By exchanging 2 and 4 in Eqs. (42)–(44), we can readily obtain the corresponding one-loop RG equations for their coupling constants:

$$\frac{dm_{(4)}}{d\ln b} = \frac{A_{34} + A_{12}}{2}m_{(4)} - \frac{1}{\pi l^2}m_{(4)}(C_{34}h_{(4)} + C_{12}\overline{h}_{(4)}),$$
(51)

$$\frac{dh_{(4)}}{d\ln b} = A_{34}h_{(4)} - \frac{1}{4\pi l^2}(C_{12}m_{(4)}^2 + 4C_{34}h_{(4)}^2),$$
(52)

$$\frac{d\overline{h}_{(4)}}{d\ln b} = A_{12}\overline{h}_{(4)} - \frac{1}{4\pi l^2}(C_{34}m_{(4)}^2 + 4C_{12}\overline{h}_{(4)}^2).$$
(53)

Here, the coupling constants are integrals of the interchain coupling functions in $H_{b,4}$ and $H_{u,4}$:

$$m_{(4)} \equiv 2\pi l^2 \sum_j M_j^{(4)} = \frac{g}{\alpha^2}\int \mathcal{M}^{(4)}(y)dy,$$

$$h_{(4)} \equiv 2\pi l^2 \sum_j H_j^{(4)} = \frac{g}{\alpha^2}\int \mathcal{H}^{(4)}(y)dy < 0,$$

$$\overline{h}_{(4)} \equiv 2\pi l^2 \sum_j \overline{H}_j^{(4)} = \frac{g}{\alpha^2}\int \overline{\mathcal{H}}^{(4)}(y)dy < 0.$$

The inequalities hold true for bare values of $h_{(4)}$ and $\overline{h}_{(4)}$ in the presence of the repulsive interaction g (> 0).

The RG equations tell us that the bare value of the repulsive interaction g has a critical strength above/below which $m_{(4)}$ as well as $h_{(4)}$ and $\overline{h}_{(4)}$ become relevant/irrelevant on the renormalization. In the strong-coupling phase with $m_{(4)} \to \pm\infty$ and $h_{(4)}, \overline{h}_{(4)} \to -\infty$, $H_{b,4}$ and $H_{u,4}$ are maximally minimized by

$$\phi_{3,j} + \phi_{4,j} = \Phi_-, \quad \phi_{2,j} + \phi_{1,j} = \begin{cases} 2n\pi - \Phi_-, \\ (2n+1)\pi - \Phi_-, \end{cases}$$
(54)

$$\theta_{3,j} - \theta_{4,j} = \Theta_-, \quad \theta_{2,j} - \theta_{1,j} = \begin{cases} (2n+1)\pi - \Theta_-, \\ 2n\pi - \Theta_-, \end{cases}$$
(55)

with

$$\sigma_{3\overline{4},m} = \sigma_{2\overline{1},m} = \sigma_{\overline{34},m} = \sigma_{\overline{21},m} = \sigma,$$
(56)

for $m_{(4)} > 0$. The locking of the total displacement field results in an electrically insulating behavior along the field direction, while the long-range order of the spin superconducting phases leads to a long-range helical magnetic order, e.g.,

$$\langle S_{A,x}(\boldsymbol{r})\rangle + i\langle S_{A,y}(\boldsymbol{r})\rangle = v'e^{i\Theta_-}\cos[(k_{F,1}+k_{F,2})z],$$

$$\langle S_{B,x}(\boldsymbol{r})\rangle + i\langle S_{B,y}(\boldsymbol{r})\rangle = v''e^{i\Theta_-}\cos[(k_{F,1}+k_{F,2})z]$$
$$+ w''e^{i\Theta_-}\cos[(k_{F,3}+k_{F,4})z].$$

As for the charge degree of freedom, the insulating phase does not break the translational symmetry; $\langle\rho(\boldsymbol{r},c)\rangle$ always respects the translational symmetry for $c = A, B, A', B'$. The phase is stabilized by the pairings with the same LL but between the different spins, so that we call this phase the magnetic Mott insulator [46].

Unlike the spin nematic excitonic insulator, the transition temperature of the magnetic Mott insulator goes to zero at a certain critical field below H_0. For $H \to H_0$ ($H < H_0$), where K_1 and K_4 become very small, both A_{34} and A_{12} in Eqs. (51)–(53) become negatively very large. Accordingly, unlike in the spin nematic excitonic insulator case in the previous section, *all* of the three coupling constants, $m_{(4)}$, $h_{(4)}$, and $\overline{h}_{(4)}$ are renormalized to zero for those H sufficiently close to H_0 ($H < H_0$). In other words, the transition temperature of the magnetic Mott insulator always goes to zero at a certain critical field below H_0. This is also the case with the plain excitonic insulator stabilized by $H_{u,1}$, $H_{u,3}$, and $H_{b,13}$. These RG phase diagrams are not consistent with the experimental phase diagram of graphite under the high field [13–18,20].

Besides, the helical magnetic order in the Mott insulator is expected to be weak against *magnetic* disorders. Considering the anisotropy of the g factor in graphite [47], it is natural to assume that the high magnetic field allows the system to have single-particle backward scatterings between two electron pockets with $(n, \sigma) = (0, \uparrow)$ and $(0, \downarrow)$, and also between two hole pockets with $(n, \sigma) = (-1, \uparrow)$ and $(-1, \downarrow)$. The backward scatterings do exist, especially when graphite contains those graphene layers whose normal vectors (c axis) have nonzero angles with respect to the field direction. Such graphene layers can appear anywhere and randomly along the c axis, so that the backward scatterings are generally accompanied by random U(1) phases $\lambda_{j,\pm}(z)$:

$$H'_{\text{imp}} = \sum_j \int dz A_{j,+}(z)\{e^{i\lambda_{j,+}(z)}\psi_{1,+,j}^\dagger(z)\psi_{2,-,j}(z) + \text{H.c.}\} + \sum_j \int dz A_{j,-}(z)\{e^{i\lambda_{j,-}(z)}\psi_{1,-,j}^\dagger(z)\psi_{2,+,j}(z) + \text{H.c.}\} + \cdots.$$

When bosonized, these single-particle backward scatterings add random U(1) phases into $\Phi_- \pm \Theta_-$ in Eqs. (54) and (55), respectively:

$$H'_{\text{imp}} = \sum_j \int dz A_{j,+}(z)\sigma_{1\overline{2},j}\cos[\phi_{2,j} + \phi_{1,j} - \theta_{2,j} + \theta_{1,j} + \lambda_{+,j}(z)]$$

$$+ \sum_j \int dz A_{j,-}(z)\sigma_{\overline{1}2,j}\cos[\phi_{2,j} + \phi_{1,j} + \theta_{2,j} - \theta_{1,j} + \lambda_{-,j}(z)] + \cdots.$$

Since Φ_- and Θ_- comprise gapless Goldstone modes in the magnetic Mott insulator, the added random U(1) phases readily kill the long-range orders of Φ_- and Θ_-, however small the amplitudes $A_{j,\pm}(z)$ are [22–25]. Likewise, the plain excitonic insulator phase stabilized by $H_{u,1}$, $H_{u,3}$, and $H_{b,13}$ is expected to be weak against short-ranged charged disorders. The short-ranged disorder causes single-particle-type backward scatterings between $(0, \uparrow)$ and $(-1, \uparrow)$ pockets and between $(0, \downarrow)$ and $(-1, \downarrow)$ pockets. From this reasoning as well as the inconsistency between the RG phase diagrams and the experimental phase diagram of graphite, we conclude that the magnetic Mott insulator and the plain excitonic insulator can hardly explain the graphite experiment coherently.

One may expect that the spin nematic excitonic insulator could also suffer from random single-particle backward scatterings between $(0, \uparrow)$ and $(-1, \downarrow)$ pockets or between $(0, \downarrow)$ and $(-1, \uparrow)$ pockets. Nonetheless, these scatterings unlikely exist in the real system. Or, if any, they are much smaller than the others, because the relativistic spin-orbit interaction is needed for them, and it is extremely small in graphite [33,47]. Without the spin-orbit interaction, these backward scatterings need both the magnetic scatter and the short-ranged charged scatter on the same spatial point. Microscopically, however, these two types of the scatters are of different origins and they have no correlation at all. From this reasoning as well as the generic consistency between the RG phase diagram ($H < H_0$ in Fig. 1) and the experimental phase diagram, we conclude that an insulating phase in graphite at $H < H_0$ is the spin nematic excitonic insulator stabilized by the interplay between $H_{u,2}$ and $H_{b,2}$.

VI. TWO-POCKET MODEL ($H > H_0$)

For $H > H_0$, both the electron pocket with $(n, \sigma) = (0, \uparrow)$ and hole pocket with $(n, \sigma) = (-1, \downarrow)$ leave the Fermi level [8,19]. The low-energy electronic system for $H > H_0$ comprises only the electron pocket with $(n, \sigma) = (0, \downarrow)$ and the hole pocket with $(n, \sigma) = (-1, \uparrow)$. As before, we call $(n, \sigma) = (0, \downarrow)$ as $a = 2$ and $(n, \sigma) = (-1, \uparrow)$ as $a = 3$. The charge neutrality condition is given by $k_{F,0,\downarrow} + k_{F,-1,\uparrow} = \pi/c_0$. Under this condition, the interaction allows the following umklapp term:

$$H'_u = \sum_{j,m,n} \psi^\dagger_{3,+,n} \psi^\dagger_{2,+,j+m-n} \psi_{2,-,m} \psi_{3,-,j} + \text{H.c.}, \quad (57)$$

where the integrals over z and scattering matrix elements are omitted. Other two-particle interaction terms that are linked with the umklapp term at the one-loop level of the fermionic RG equations are interpocket and intrapocket scatterings between different chiralities [42]. They are

$$H'_b = \sum_{j,m,n} \psi^\dagger_{3,\pm,n} \psi^\dagger_{2,\mp,j+m-n} \psi_{2,\mp,m} \psi_{3,\pm,j}, \quad (58)$$

and

$$H'_d = \sum_{j,m,n} \begin{cases} \psi^\dagger_{2,\pm,n} \psi^\dagger_{2,\mp,j+m-n} \psi_{2,\mp,m} \psi_{2,\pm,j}, \\ \psi^\dagger_{3,\pm,n} \psi^\dagger_{3,\mp,j+m-n} \psi_{3,\mp,m} \psi_{3,\pm,j}, \end{cases} \quad (59)$$

respectively.

To construct effective boson theories of possible insulating phases stabilized by H'_u, we first assume the in-plane
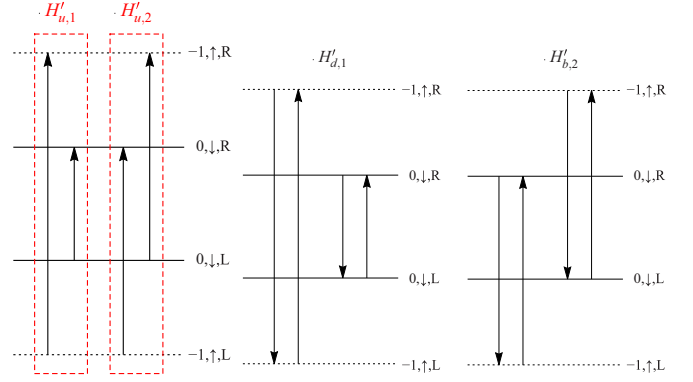

FIG. 6. Left: Schematic pictures of two-particle umklapp scatterings that are allowed in the two-pocket model under the charge neutrality condition, $H'_{u,1}$ and $H'_{u,2}$. They are direct ($j = n$) and exchange ($m = n$) processes of Eq. (57), respectively. Middle: Two-particle intrapocket scatterings $H'_{d,1}$: exchange processes ($m = n$) of Eq. (59). Right: Two-particle interpocket scatterings $H'_{b,2}$: exchange processes ($m = n$) of Eq. (58). As in Fig. 2, the vertical axis denotes the momentum along the field direction (k_z), while the horizontal axis denotes the chain index $y_j = k_j l^2$ with $k_j \equiv 2\pi j/L_x$ [$j = 1, 2, \ldots, L_x L_y/(2\pi l^2)$].

(graphene-plane) translational symmetry of the insulating phases, consider electron pairing within the same chain, and treat the interchain electron-electron interactions by the Hartree-Fock approximation. Specifically, we keep only the direct process (Hartree; $j = n$) and the exchange process (Fock; $m = n$) in Eqs. (57)–(59), and bosonize them into cosine terms:

$$H'_u + H'_b + H'_d = H'_{u,1} + H'_{u,2} + H'_{d,1} + H'_{b,2} + \cdots,$$

$$H'_{u,1} = \sum_{j,m} N^{(1)}_{j-m} \int dz\, \sigma_{3\bar{3},j}\sigma_{2\bar{2},m} \cos[2\phi_{3,j} + 2\phi_{2,m}], \quad (60)$$

$$H'_{u,2} = \sum_{j,m} N^{(2)}_{j-m} \int dz\, \sigma_{2\bar{3},j}\sigma_{3\bar{2},m} \cos\left[Q^{23}_{+,j} + Q^{23}_{-,m}\right], \quad (61)$$

$$H'_{d,1} = \sum_{j,m} O^{(1)}_{j-m} \int dz\, \sigma_{3\bar{3},j}\sigma_{3\bar{3},m} \cos[2\phi_{3,j} - 2\phi_{3,m}]$$
$$+ \sum_{j,m} \overline{O}^{(1)}_{j-m} \int dz\, \sigma_{2\bar{2},j}\sigma_{2\bar{2},m} \cos[2\phi_{2,j} - 2\phi_{2,m}], \quad (62)$$

$$H'_{b,2} = \sum_{j,m} P^{(2)}_{j-m} \int dz\, \sigma_{2\bar{3},j}\sigma_{2\bar{3},m} \cos\left[Q^{23}_{-,j} - Q^{23}_{-,m}\right]$$
$$+ \sum_{j,m} \overline{P}^{(2)}_{j-m} \int dz\, \sigma_{3\bar{2},j}\sigma_{3\bar{2},m} \cos\left[Q^{23}_{+,j} - Q^{23}_{+,m}\right]. \quad (63)$$

Here $H'_{u,1}$ is from the Hartree process ($j = n$) of Eq. (57), while $H'_{u,2}$, $H'_{d,1}$, and $H'_{b,2}$ are from the Fock processes ($m = n$) of Eq. (57), Eq. (59), and Eq. (58), respectively (Fig. 6). The Hartree processes of H'_d and H'_b renormalize the Luttinger parameters and Fermi velocities in H_0 [Eq. (19)]. Especially, the Hartree term of H'_d gives rise to positive $g_{2,a}$ ($a = 2, 3$)

in Eqs. (20) and (21) in the presence of the repulsive electron interaction ($g > 0$).

As in the previous section, we carried out the perturbative RG analyses on these effective boson models, $H_0 + H'_{u,1} + H'_{u,2} + H'_{d,1} + H'_{b,2}$. At the one-loop level of the perturbative RG equations, $H'_{u,1}$ and $H'_{d,1}$ are coupled with each other, and so are $H'_{u,2}$ and $H'_{b,2}$. When the bare interaction strength g is greater than critical interaction strength, respective pairs of the cosine terms grow to have larger amplitudes and the system enters strong-coupling phases. In the following two subsections, we argue that $H'_{u,1}$ and $H'_{d,1}$ stabilize a plain superposed charge density wave (CDW) phase, while $H'_{u,2}$ and $H'_{b,2}$ stabilize the spin nematic excitonic insulator phase.

A. Superposed CDW phase

When $H'_{u,1}$ and $H'_{d,1}$ become relevant, the cosine terms in Eqs. (60) and (62) are maximally minimized by the CDW phase, where a displacement field of the electron pocket and that of the hole pocket exhibit long-range orders individually:

$$2\phi_{2,j} = \Phi_2, \quad 2\phi_{3,j} = \Phi_3, \tag{64}$$

$$\Phi_2 + \Phi_3 = \begin{cases} 2n\pi & (n_{(1)} < 0), \\ (2n+1)\pi & (n_{(1)} > 0), \end{cases} \tag{65}$$

with

$$\sigma_{2\bar{2},j} = \sigma_{3\bar{3},j} = \sigma. \tag{66}$$

Such CDW is a plain superposition of a charge density wave of the electron pocket with $\downarrow$ spin and $\pi/k_{F,0,\downarrow}$ spatial pitch and that of the hole pocket with $\uparrow$ spin and $\pi/k_{F,-1,\uparrow}$ spatial pitch. Since this strong-coupling phase is not accompanied by any long-range order of spin superconducting phase fields, the transition temperature of the superposed CDW phase increases monotonically in the magnetic field in the presence of the repulsive electron-electron interaction: $g_{2,a=2}, g_{2,b=3} > 0$. Such behavior of the transition temperature is not consistent with graphite's experimental phase diagram; the experiment shows the reentrant insulator-metal transition at $H = H_{c,2} \simeq 75$ T.

Besides, the long-range order of the *relative* displacement between the two charge density waves, $\Phi_2 - \Phi_3$, is weak against random charged impurities, unless their spatial pitches are commensurate to the underlying lattice constant c_0 [22–25]. Namely, the impurity potentials induce single-particle backward scatterings within the same electron pocket and/or within the same hole pocket. The impurities appear spatially randomly as a function of the coordinate z. Thus, the scatterings add random U(1) phases into $2\phi_{2,j}$ and $2\phi_{3,j}$, unless Φ_2 and Φ_3 in Eq. (64) have finite mass in the CDW phase. When $2k_{F,0,\downarrow}$ or $2k_{F,-1,\uparrow}$ is incommensurate with respect to $2\pi/c_0$, the long-range ordering of $\Phi_2 - \Phi_3$ in Eq. (64) is generally accompanied by a gapless phason excitation. Thereby, even small random charged impurities wipe out the long-range order of the relative phase between the two density waves. Meanwhile, being locked into the discrete values by the cosine potential in the umklapp term ($H'_{u,1}$), the total displacement field, $\Phi_2 + \Phi_3$, always has a finite mass in the superposed CDW phase. The locking is therefore robust against the random charged impurities, as far as their amplitudes are small.

B. Spin nematic excitonic insulator (SNEI-II) phase

When $H'_{u,2}$ and $H'_{b,2}$ become relevant, the cosine terms in Eqs. (61) and (63) are maximally minimized by the excitonic insulator phase with broken U(1) spin rotational symmetry. To see the nature and RG phase diagram of this strong-coupling phase, let us first reduce the interchain coupling functions in $H'_{u,2}$ and $H'_{b,2}$ into coupling constants:

$$n_{(2)} \equiv 2\pi l^2 \sum_j N^{(2)}_{j-m},$$

$$p_{(2)} \equiv 2\pi l^2 \sum_j P^{(2)}_{j-m}, \quad \overline{p}_{(2)} \equiv 2\pi l^2 \sum_j \overline{P}^{(2)}_{j-m}.$$

For the repulsive interaction case ($g > 0$), bare values of these three coupling constants are negative; the cosine terms in $H'_{u,2}$ and $H'_{b,2}$ are all from the exchange processes. The one-loop RG equations for these coupling constants take the following forms:

$$\frac{dn_{(2)}}{d\ln b} = A_{23}n_{(2)} - \frac{C_{23}}{\pi l^2}n_{(2)}(p_{(2)} + \overline{p}_{(2)}), \tag{67}$$

$$\frac{dp_{(2)}}{d\ln b} = A_{23}p_{(2)} - \frac{C_{23}}{\pi l^2}(n^2_{(2)} + p^2_{(2)}), \tag{68}$$

$$\frac{d\overline{p}_{(2)}}{d\ln b} = A_{23}\overline{p}_{(2)} - \frac{C_{23}}{\pi l^2}(n^2_{(2)} + \overline{p}^2_{(2)}). \tag{69}$$

Negative semidefinite A_{23} and positive definite C_{23} have already been defined in Eq. (38) and Appendix C3, respectively. Thanks to an inversion symmetry ($Q^{ab}_{+,j} \to -Q^{ab}_{-,j}$), the coupled equations as well as the bare values of the coupling constants are symmetric with respect to an exchange between $p_{(2)}$ and $\overline{p}_{(2)}$. This decouples the RG equations into

$$\frac{df_\pm}{d\ln b} = A_{23}f_\pm \mp \frac{C_{23}}{\pi l^2}f^2_\pm, \tag{70}$$

where $f_\pm \equiv n_{(2)} \pm p_{(2)} = n_{(2)} \pm \overline{p}_{(2)}$. At zero temperature, A_{23} and C_{23} have no dependence on the scale change $\ln b$. Thereby, the equations immediately give an RG flow diagram as in Fig. 7. The strong and weak coupling phases at $T = 0$ are defined by

$$|n_{(2)}| - p_{(2)} > x_c \quad \text{(strong-coupling phase)},$$

$$|n_{(2)}| - p_{(2)} < x_c \quad \text{(weak-coupling phase)}, \tag{71}$$

with

$$x_c \equiv -\frac{\pi l^2}{C_{23}}A_{23} > 0. \tag{72}$$

On the strong-coupling side, the cosine terms in the bosonized Hamiltonian are maximally minimized by

$$\sigma_{2\bar{3},j} = \sigma_{3\bar{2},j} = \sigma, \tag{73}$$

$$\theta_{2,j} - \theta_{3,j} = \Theta, \tag{74}$$

$$2(\phi_{2,j} + \phi_{3,j}) = \begin{cases} 2n\pi & (n_{(2)} < 0), \\ (2n+1)\pi & (n_{(2)} > 0). \end{cases} \tag{75}$$

The locking of a sum of the two displacement fields leads to an electrically insulating property along the field direction. The
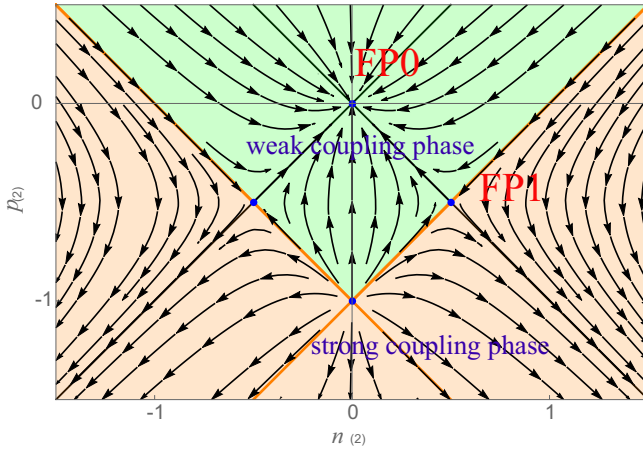
FIG. 7. Renormalization group flow at $T = 0$ in the two-dimensional parameter space subtended by $n_{(2)}$ and $p_{(2)} = \overline{p}_{(2)}$. Weak/strong-coupling phases stand for normal metal phase/spin nematic excitonic insulator (SNEI-II) phase, respectively. Quantum criticality of the quantum phase transition between these two is controlled by a fixed point named "FP1". The scaling dimension of the relevant parameter at FP1, ν_2, is given in Eq. (77).

optical conductivity calculated within the Gaussian approximation shows a gap behavior, $\sigma_{zz}(\omega) = (e^2 uK)/(2\pi l^2)\delta(\omega - \omega_g)$ with $uK = \sum_{a=2,3} u_a K_a$ and $\omega_g^2 \equiv 2\pi uK \sum_j N_j^{(2)}$ (see also the inset of Fig. 5). The long-range order of the spin superconducting phase $\theta_2 - \theta_3$ in Eq. (74) breaks the global U(1) spin rotational symmetry. The strong-coupling phase is accompanied by particle-hole pairing between the electron pocket with $\downarrow$ spin and the hole pocket with $\uparrow$ spin, so that we name the phase also as the spin nematic excitonic insulator phase. Nonetheless, the phase could be symmetrically distinct from the spin nematic excitonic insulator discussed in the previous section, depending on the *spatial parity* of the excitonic pairing (see also Sec. VIII A and Sec. X B). We thus distinguish these two by calling them SNEI-I for $H < H_0$ and SNEI-II for $H > H_0$, respectively.

The phase boundary condition, Eqs. (71) and (72), explains the metal-insulator transition at a lower field regime. For simplicity, we assume that the bare values of $n_{(2)}$ and $p_{(2)} = \overline{p}_{(2)}$ as well as $(C_{23})_{|T=0}$ have no H dependence. For a low-H regime, the magnetic length l is large; so is the critical value x_c in Eq. (72). Thereby, a given bare value of $|n_{(2)}| - p_{(2)}$ can be below the critical value x_c in the lower-H regime (weak-coupling phase; normal metal phase). On increasing H, the magnetic length l decreases and so does the critical value x_c. Thus, the bare value of $|n_{(2)}| - p_{(2)}$ exceeds the critical value x_c at a certain critical magnetic field ($H = H_c^*$). For $H_c^* < H$, the system enters the strong-coupling phase (SNEI-II phase). From a comparison with the graphite experiment [17,18,20], we assume that H_c^* is *smaller* than H_0. In this case, the system at $T = 0$ undergoes a phase transition from SNEI-I to SNEI-II at $H = H_0$.

The phase boundary condition Eqs. (71) and (72) also explains the $T = 0$ insulator-metal *reentrant* transition at a higher-field regime. When the field H increases further, both electron and hole pockets become smaller in size in the k_z space. This makes their bare Fermi velocities $v_{F,2}$ and $v_{F,3}$ as

well as Luttinger parameters K_2 and K_3 smaller. The smaller Luttinger parameters can increase the critical value x_c through the dependence of A_{23} on K_2^{-1} and K_3^{-1} [Eq. (38)]. To be more precise, suppose that the electron pocket with $n = 0$ LL with $\downarrow$ spin and the hole pocket with $n = -1$ LL with $\uparrow$ spin leave the Fermi level at $H = H_1$. When H gets "close" to H_1 from below ($H < H_1$), the increase of $-A_{23}$ can overcome the decrease of l^2 in Eq. (72), such that x_c increases again. Namely, for $H < H_1$, l^2 is always bounded by $(\hbar c)/(e H_1)$ from below, while K_2^{-1} and K_3^{-1} as well as $-A_{23}$ have no upper bound in principle. Thus, for some magnetic field $H_{c,2}$ with $H_c^* < H_0 < H_{c,2} < H_1$, x_c exceeds the bare value of $|n_{(2)}| - p_{(2)}$ again and the system falls into the weak-coupling phase (normal metal phase) again. From the set of reasonable parameter values used in Fig. 1 (see Appendix C4 for the set of parameters used in Fig. 1), we obtain $H_{c,2} = 82$ T and $H_1 = 120$ T.

C. Critical natures of the MI and reentrant IM transitions

The reentrant transition point at $H = H_{c,2}$ is a zero-temperature continuous phase transition with dynamical exponent $z = 1$. Toward this quantum critical point, the correlation length along the field direction ξ_z diverges as

$$\xi_z \propto |H - H_{c,2}|^{-1/\nu_2}. \tag{76}$$

The critical exponent ν_2 is given only by the Luttinger parameters *at the critical point* ($H = H_{c,2}$),

$$\nu_2 = \frac{1}{2} \sum_{a=2,3} \left(K_a + K_a^{-1} \right) - 2. \tag{77}$$

Since $z = 1$, the correlation length is inversely proportional to the gap ω_g in the optical conductivity along the field direction, $\sigma_{zz}(\omega)$:

$$\omega_g \propto (H_{c,2} - H)^{z/\nu_2} = (H_{c,2} - H)^{1/\nu_2}, \tag{78}$$

for $H < H_{c,2}$. By measuring how the gap vanishes toward $H = H_{c,2}$ as a function of the field, one can determine the values of the Luttinger parameters at the quantum critical point. By seeing how much the Luttinger parameters thus determined deviate from 1, one could also test the validity of our theory of the reentrant insulator-metal transition.

The low-H metal-insulator transition between the normal metal and SNEI-I phases is also a quantum critical point. Toward this point, $H = H_{c,1}$, the gap ω_g in the SNEI-I phase also vanishes,

$$\omega_g \propto (H - H_{c,1})^{1/\nu_1}, \tag{79}$$

for $H_{c,1} < H$. The critical exponent ν_1 is given by the Luttinger parameters at $H = H_{c,1}$,

$$\nu_1 = \frac{1}{2} \sum_a \left(K_a + K_a^{-1} \right) - 2, \tag{80}$$

where the summation in the pocket index a is taken over

$$\begin{aligned} a = 1, 4 \quad & (|A_{14}|C_{23}h_{(2)} \gg |A_{23}|C_{14}\overline{h}_{(2)}), \\ a = 2, 3 \quad & (|A_{14}|C_{23}h_{(2)} \ll |A_{23}|C_{14}\overline{h}_{(2)}). \end{aligned} \tag{81}$$

Meanwhile, the gap in $\sigma_{zz}(\omega)$ reaches finite constant values at $H = H_0 \pm 0$, when the phase transition from the SNEI-I

phase to the SNEI-II phase is of the first order. This is the case when the *spatial parities* of the excitonic pairings in the two phases are different from each other (see also Sec. VIII A and Sec. X B).

VII. IN-PLANE RESISTANCE IN THE FOUR-POCKET MODEL ($H < H_0$)

Generally, in-plane current operators in the clean limit have finite matrix elements only between neighboring Landau levels. When the temperature is much lower than the cyclotron frequency $\hbar\omega_0$, the in-plane resistance increases on increasing magnetic field H. Contrary to this expectation, the low-temperature in-plane resistance in graphite under high magnetic field shows an unexpected H dependence [14,15,17,18]. It shows a broad peak around 15 T $\sim$ 30 T, and then decreases slowly on further increasing H. From $H = 30$ T to $H = H_0 \simeq 53$ T, the resistance reduces by half or more. Besides, when the system enters the low-field-side out-of-plane insulating phase ($H_{c,1} < H < H_0$), the in-plane resistance shows an additional steep increase by 15% to 30% [14,15,18]. Unlike the out-of-plane resistivity, the additional increase amount becomes *smaller* for lower temperature.

A. *H* dependence of R_{xx} at $H < H_0$

The H dependence of the in-plane resistance in 30 T $< H < H_0 \simeq 53$ T can be explained by charge transport along the surface chiral Fermi arc (SCFA) states. To see this, notice first that the electron/hole pockets in the bulk are terminated with SCFA states of the electron/hole type around the boundary regions of the system (see Fig. 2 and Appendix A). The SCFA state of the electron/hole type is a bundle of N_a chiral edge modes of electron/hole type, respectively, where N_a is the number of k_z points within the electron/hole pocket ($a = 1, 2, 3, 4$). Here a denotes the pocket index: $1 \equiv (0, \uparrow)$, $2 \equiv (0, \downarrow)$, $3 \equiv (-1, \uparrow)$, and $4 \equiv (-1, \downarrow)$. The chiral edge mode enables unidirectional electric current flow along the boundary in the xy plane. The chiral directions of the electric current flows of the electron-type and hole-type edge modes are opposite to each other.

In the presence of short-ranged charged impurities, the current flow along the electron-type edge mode with σ spin can be scattered into the hole-type edge mode with the same σ spin. In this respect, the SCFA state with $(-1, \sigma)$ (hole type) and that with $(0, \sigma)$ (electron type) cancel each other by the intrasurface backward scatterings due to the charged impurities. In the absence of any backward scatterings between $(0, \sigma)$ and $(-1, \overline{\sigma})$ [$(\sigma, \overline{\sigma}) = (\uparrow, \downarrow), (\downarrow, \uparrow)$; see the last paragraph in Sec. V for the reasoning of the absence], both $N_2 - N_4$ anticlockwise (electron-type) chiral edge modes with $\downarrow$ spin and $N_3 - N_1$ clockwise (hole-type) chiral edge modes with $\uparrow$ spin *individually* contribute to the two-terminal conductance within the xy plane:

$$G_s = \frac{e^2}{h}(N_2 - N_4 + N_3 - N_1) = \frac{2e^2}{h}(N_3 - N_1). \quad (82)$$

From the first line to the second line, we used the charge neutrality condition: $N_1 + N_2 = N_3 + N_4$. Importantly, the in-plane conductance given by Eq. (82) usually *increases* on

increasing H for $H < H_0$. This is because a variation of N_1 with respect to H is larger than that of N_3: $dN_1/dH < dN_3/dH < 0$. For $N_3 = [L_z/(2c_0)](1 - H/H_1)$ and $N_1 = [L_z/(2c_0)](1 - H/H_0)$, the H dependence of the resistance due to the surface charge transport is given by

$$R_s = \frac{h}{e^2} \frac{c_0}{L_z} \frac{H_0 H_1}{H(H_1 - H_0)}. \quad (83)$$

The resistance is on the order of 1 Ω at $H = 30$ T ($L_z = 50$ μm, $c_0 = 0.67$ nm, $H_0 = 50$ T, and $H_1 = 120$ T). The value is on the same order as the experimental value (2 $\Omega \sim$ 3 Ω) [17].

B. *T* dependence of R_{xx} at $H < H_0$

The T dependence of the in-plane resistance inside the low-field-side insulating phase ($H_{c,1} < H < H_0$) can be explained by a coupling between the SCFA states and gapless Goldstone modes associated with the spin nematic order in the bulk. The spin nematic excitonic insulator (SNEI-I) phase breaks two global U(1) symmetries. They are the U(1) spin rotational symmetry around the field direction and the translational symmetry associated with the spatial polarization of the spin ($\uparrow$ or $\downarrow$) and pseudospin ($n = 0$ LL or $n = -1$ LL) densities.

Such SNEI-I phase has two low-energy gapless excitations. They are space-time fluctuations of the following two phase variables [Eqs. (45), (46)]:

$$f_j(z) \equiv [\theta_{3,j}(z) - \theta_{2,j}(z)] - [\theta_{4,j}(z) - \theta_{1,j}(z)] - 2\Theta_-, \quad (84)$$

$$g_j(z) \equiv [\phi_{3,j}(z) + \phi_{2,j}(z)] - [\phi_{4,j}(z) + \phi_{1,j}(z)] - 2\Phi_-. \quad (85)$$

When they vary slowly in z/c_0 and $y_j/l \equiv 2\pi l j/L_x$, their energy dispersions become linear in the momenta:

$$\mathcal{H}_{sw} = \frac{1}{2L_z N} \sum_{\mathbf{k}} (B_1 k^2 + C_1 k_z^2) f^{\dagger}(\mathbf{k}) f(\mathbf{k})$$
$$+ \frac{1}{2L_z N} \sum_{\mathbf{k}} (B_2 k^2 + C_2 k_z^2) g^{\dagger}(\mathbf{k}) g(\mathbf{k}), \quad (86)$$

with positive B_t and C_t ($t = 1, 2$), and $\mathbf{k} \equiv (k_z, k)$. k_z and k are conjugate to z and $y_j \equiv 2\pi l^2 j/L_x$, respectively:

$$f_j(z) \equiv \frac{1}{L_z N} \sum_{\mathbf{k}} e^{ik_z z + iky_j} f(\mathbf{k}),$$

$$g_j(z) \equiv \frac{1}{L_z N} \sum_{\mathbf{k}} e^{ik_z z + iky_j} g(\mathbf{k}).$$

The gapless modes couple with the SCFA states through a simple density-density interaction, e.g.,

$$\mathcal{H}' = \frac{1}{L_x} \sum_{a,\tau,b} \sum_n \sum_m \int dz \mathcal{A}^{e-b}_{(a,\tau;b)}(y_n, y_m)$$
$$\times \rho_{a,\tau,n}(z)[\psi^{\dagger}_{b,m}(z)\psi_{b,m}(z)], \quad (87)$$

with bulk density operator $\rho_{a,\tau,n}(z) \equiv \psi^\dagger_{a,\tau,n}(z)\psi_{a,\tau,n}(z)$ $(|y_n| \leqslant L_y/2)$. $a, b = 1, 2, 3, 4$ denote the pocket indices, and $\tau = \pm$ is the chirality index. By definition, the summations over the chain indices n and m in Eq. (87) are restricted within the bulk region and edge region, respectively; $L_y/2 \leqslant |y_m|$.

When bosonized, the density operator in the bulk region is given by a linear combination of the phase variables, $2\pi\rho_{a,\tau,n}(z) \equiv \partial_z\phi_{a,n}(z) - \tau\partial_z\theta_{a,n}(z)$. Such phase variables generally contain the two low-energy gapless excitations with the linear dispersions. Thus, the situation becomes precisely analogous to the electron-phonon interaction in metal [48,49]. The coupling endows the SCFA electrons with finite transport life times [49]. When the temperature is on the order of the bandwidth of the gapless Goldstone modes (but smaller than the transition temperature of the SNEI-I phase), the transport lifetime of the SCFA states is linear in temperature T; so is the resistivity due to the surface charge transport. This can explain the T dependence of the in-plane resistance in the insulating phases in graphite [14,15,18].

VIII. IN-PLANE RESISTANCE IN THE TWO-POCKET MODEL ($H > H_0$)

The in-plane resistance of graphite under the high magnetic field stays almost constant in the field inside the high-field-side out-of-plane insulating phase ($H_0 < H < H_{c,2}$) [17–21]. Above the reentrant insulator-metal (IM) transition field ($H_{c,2} < H$), the resistance shows the normal behavior: R_{xx} increases in the field [21].

In the following, we will argue that the SNEI-II phase in $H > H_0$ can be either topological [50–52] or topologically trivial, depending on the spatial parity of the excitonic pairing between electron pocket ($n = 0, \downarrow$) and hole pocket ($n = -1, \uparrow$). When the excitonic pairing field is an odd function in the momentum k_z, the SNEI-II phase becomes topological and thereby the SCFA state of electron type ($n = 0, \downarrow$) and the SCFA state of hole type ($n = -1, \uparrow$) are reconstructed into a helical surface state with a gapless Dirac cone. The electric transport through such Dirac-cone surface state is primarily determined by carrier density doped in the surface region, which has little field dependence. Thus, the reconstructed Dirac-cone surface state may provide a simple explanation for the field (nearly) independent and metallic behavior of the in-plane resistance observed in the high-field-side out-of-plane insulating phase ($H_0 < H < H_{c,2}$).

Topological SNEI phase

The strong-coupling phase discussed in Sec. VI (SNEI-II phase) consists of two topologically distinct phases, depending on the sign of the umklapp term $n_{(2)}$. A mean-field one-dimensional electronic Hamiltonian of the strong-coupling phase can be schematically described by the 2×2 Pauli matrices as

$$H^{\mathrm{snei2}}_{\mathrm{mf}}(q_z) = [M - 2\gamma_2\cos(q_zc_0)]\boldsymbol{\sigma}_3 + \Delta_{\mathrm{EI}}(q_zc_0)\boldsymbol{\sigma}_1$$

$$\equiv E_{\mathrm{EI}}(q_z)\{N_1(q_z)\boldsymbol{\sigma}_3 + N_2(q_z)\boldsymbol{\sigma}_1\}, \quad (88)$$

with $M < 2\gamma_2$, and

$$E_{\mathrm{EI}}(q_z) \equiv \sqrt{[M - 2\gamma_2\cos(q_zc_0)]^2 + \Delta^2_{\mathrm{EI}}(q_zc_0)}. \quad (89)$$
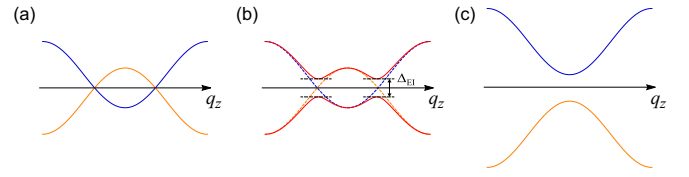

FIG. 8. (a) Single-particle electronic states in normal metal phase (two-pocket model). The electron pocket (blue curve) is formed by the $n = 0$ LL with $\downarrow$ spin, and the hole pocket (yellow curve) is by the $n = -1$ LL with $\uparrow$ spin. (b) Single-particle electronic states with the excitonic pairing. (c) Single-particle electronic states in the vacuum region.

The first and second elements of the 2×2 matrices correspond to the $n = 0$ LL with $\downarrow$ spin and $n = -1$ LL with $\uparrow$ spin, respectively [Fig. 8(a)]. For clarity, the electron pocket around $k_z = 0$ is shifted by π/c_0 in Eq. (88): $q_z \equiv k_z - \frac{\pi}{c_0}$. $\Delta_{\mathrm{EI}}(q_zc_0)$ stands for an excitonic pairing between the electron and hole pockets [Fig. 8(b)]. The pairing is induced by the umklapp $H'_{\mathrm{u},2}$ and interpocket scattering terms $H'_{\mathrm{b},2}$. The function form of $\Delta_{\mathrm{EI}}(q_zc_0)$ is determined by the value of the total displacement field, such as in Eq. (75).

For the negative umklapp term, $n_{(2)} < 0$, the excitonic pairing field $\Delta_{\mathrm{EI}}(q_zc_0)$ is an odd function in q_z, while, for the positive case, $n_{(2)} > 0$, it is even in q_z. These two cases represent two topologically distinct phases. In the former/latter case, the following topological winding number defined for the bulk 1-dimensional Hamiltonian Eq. (88) takes ± 1/zero respectively [53–55]:

$$Z \equiv \int_{-\frac{\pi}{c_0}}^{\frac{\pi}{c_0}} \frac{dq_z}{2\pi}\big(\vec{N} \times \partial_{q_z}\vec{N}\big)_3, \quad (90)$$

with $\vec{N} \equiv (N_1(q_z), N_2(q_z), 0)$.

The nonzero bulk winding number reconstructs the SCFA state of the electron type and that of the hole type into a 2-d surface state with a gapless Dirac cone at side surfaces. The side surface is subtended by z ($\parallel H$) and either x or y [Fig. 9(a)]. To be concrete, impose the periodic boundary conditions along z and x, and put a confining potential along the y direction. The mass term M in Eq. (88) depends on the coordinate y. In the vacuum regime, $|y| > L_y/2$, the electron/hole pocket goes above/below the Fermi level [Fig. 8(c)]. Thereby, Eq. (88) enters a normal 1-dimensional semiconductor regime, $M > 2\gamma_2$: the winding number takes zero in the
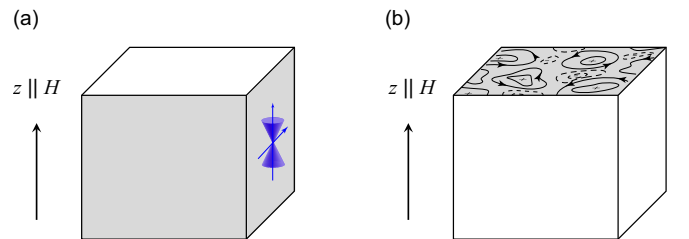

FIG. 9. Schematic pictures of (a) side surfaces (gray area) with the two-dimensional helical surface state with a gapless Dirac cone, and (b) top surface (gray area) with the two-dimensional Chalker-Coddington network model.
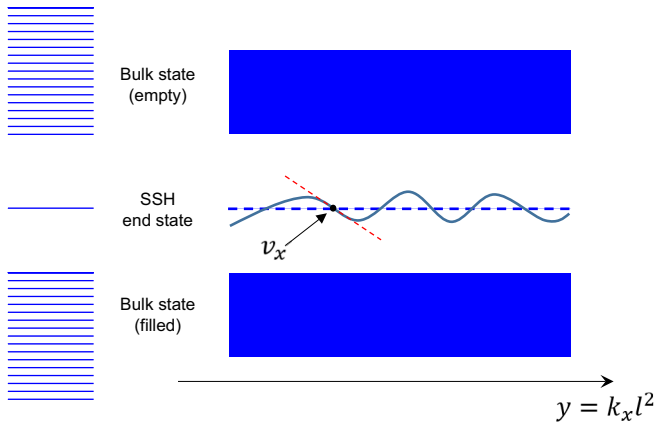
FIG. 10. Schematic picture of energetically degenerate SSH end states within the bulk excitonic band gap (blue dotted line). In a generic situation, the degeneracy is lifted by an electrostatic potential (black solid curve). An associated spatial gradient of the end-state eigenenergy with respect to y leads to a chiral electric current along the $-x$ direction.

vacuum. In the bulk region, $|y| < L_y/2$, the gapped mean-field Hamiltonian with the negative $n_{(2)}$ is in the band-inverted regime, $M < 2\gamma_2$: the winding number takes ± 1. Such two topologically distinct 1-dimensional gapped systems are inevitably separated by a 1-d gapless Dirac Hamiltonian, which should come somewhere around $|y| = L_y/2$. In other words, the side surface has a 2-d helical surface state that forms a gapless Dirac cone as a function of k_z and $y \equiv k_x l^2$ [Fig. 9(a)].

The reconstructed surface state has the *helical* velocities not only along the z direction but also along the x direction. To see this, notice that the velocity along the x direction is given by a derivative of the single-particle energy with respect to the spatial coordinate y: $v_x \equiv l^2 \partial E_{EI}/\partial y$. Such velocity changes its sign around $y = L_y/2$, where $E_{EI}(q_z)$ forms the 1-d gapless Dirac dispersion: $v_x < 0$ for $y < L_y/2$ and $v_x > 0$ for $y > L_y/2$ [see also Figs. 8(b) and 8(c)].

Quantitatively, the Dirac cone is highly anisotropic in its velocity within the side surface. Namely, the velocity along the x direction is determined by a work function in the edge region: $v_x = O(l^2 \partial M/\partial y)$. Conventionally, the work function varies in energy on the order of eV within a length scale of Å: $\partial M/\partial y = O(eV/Å)$. Thus, the velocity along the x direction is much faster than that along the z direction, the latter of which is given by the energy scale of the bandwidth ($2\gamma_2$) or the excitonic pairing (Δ_{EI}).

The 2-d helical surface state in the side surface is continuously connected to a 2-d critical wave function sitting on a top (bottom) surface. The top (bottom) surface is subtended by x and y coordinates [Fig. 9(b)]. Theoretically, the critical wave function belongs to the 2-d quantum Hall universality class, while it is generically off the Fermi level.

To see this, impose the open boundary condition along z ($\parallel H$) direction. The nonzero bulk winding number leads to an in-gap end state called the SSH (Su-Schrieffer-Heeger) state within the bulk excitonic gap (left panel of Fig. 10). The end states are localized at the two open boundaries along z direction, top and bottom surfaces. Due to the Landau degeneracy

associated with the in-plane coordinate degree of freedom, each boundary has an extensive number of such end states. In the clean limit, they are energetically degenerate. In the presence of charged impurities on the surface, the degeneracy is lifted by an electrostatic potential created by the impurities (right figure of Fig. 10). The potential depends on x and y, causing a finite spatial gradient of the end-state eigenenergy. The gradient in x or y gives rise to a chiral electric current (one-dimensional chiral mode) along y or $-x$ direction, respectively. Such chiral mode encloses a region with higher electrostatic potential. An uneven potential landscape gives rise to a group of chiral modes on the surface [Fig. 9(b)], where two spatially proximate (and thus counterpropagating) modes have finite intermode hoppings. Electronic states of such surface can be described by the Chalker-Coddington network (CCN) model [56,57]. The previous studies on the CCN model [56,58] conclude that a phase diagram as a function of the chemical potential has two localized regimes and the 2-d quantum Hall critical point intervenes between these two localized regimes. Thus, in-gap surface electronic states sitting on the top (bottom) surface are generally localized within the in-plane direction, unless the chemical potential is fine-tuned to the critical point.

IX. SUMMARY

Graphite under high magnetic field exhibits mysterious metal-insulator (MI) transitions as well as insulator-metal (IM) reentrant transitions. We discuss these enigmatic electronic phase transitions in terms of perturbative RG analyses of effective boson theories. We argue that the two insulating phases in graphite under high field are excitonic insulators with spin nematic orderings. Similar conclusions were suggested by experimental works both for $H < H_0$ [20] and $H > H_0$ [18]. This paper enumerates possible umklapp terms allowed under the charge neutrality condition, clarifies the nature of insulating states stabilized by each of them, and argues that excitonic insulators with long-range orderings of spin superconducting phases can give a possible explanation to the graphite experiments.

Based on this, we propose the following mechanism for the reentrant IM transition: When a pair of electron and hole pockets gets smaller in size, strong quantum fluctuation of the spin superconducting phase destabilizes the spin nematic excitonic insulator, causing the reentrant IM transition. The strength of the quantum fluctuation is quantified by the Luttinger parameters of the electron and hole pockets. We relate the Luttinger parameters with the critical exponent of the $T = 0$ reentrant IM transition point. We show that the exponent can be experimentally determined from the infrared optical spectroscopy. By determining the Luttinger parameters at the transition point, experimentalists can test the validity of our theory for the reentrant IM transition.

We attribute the "unexpected" field and temperature dependencies of the in-plane electric transport in graphite under the high field to surface charge transports through surface chiral Fermi arc (SCFA) states and reconstructed Dirac-cone surface states. We first argue that a metallic temperature dependence of the in-plane transport observed in the low-field-side insulating phases is due to bulk-edge couplings between the SCFA

states and gapless Goldstone modes associated with the spin nematic orderings. Being gapless excitations, the Goldstone modes in the spin nematic excitonic insulator phases could be experimentally detected through ultrasound measurements [59]. We also argue that the odd-parity excitonic pairing in the bulk reconstructs SCFA states of electron and hole into a $(2 + 1)$-d helical surface state with a gapless Dirac cone. Based on this finding, we discuss the field (nearly) independent and metallic behavior of the in-plane transport inside the high-field-side insulating phase [14,15,17,18].

X. DISCUSSION

A. Nature of the "normal" metal phase and criticality of metal-insulator transition

Our theory regards the "normal" metallic phase in the graphite experiment as the decoupled Luttinger liquid (LL) phase, where we assume that interchain electron-electron interactions only renormalize the Luttinger parameters and Fermi velocities as in Eqs. (20), (21), (B6), and (B7). Nonetheless, it could be possible that a fixed point of the decoupled LL phase [the Gaussian theory given by Eq. (19); schematically denoted by "FP0" in Fig. 11] is *unstable* against a certain perturbation associated with the interchain interactions (denoted by X in Fig. 11) and, as a result, the "normal" metal phase is characterized by a new stable fixed point (schematically denoted by "FP3" in Fig. 11). The stable fixed point could be the Fermi-liquid fixed point [60–65] or the sliding Luttinger liquid fixed point [66,67]. One of the experimental pieces of evidence that could support our theory's assumption of the decoupled Luttinger liquid is a T-linear behavior (or at least non-Fermi-liquid behavior) in the out-of-plane resistivity in the high-T "normal" metal phase. To our best knowledge, however, no comprehensive experimental studies have been carried out so far for the temperature dependence of the resistivity in the "normal" metal phase in graphite under high magnetic field [17,20].

When the metal phase is characterized by a new free theory instead of the free theory of the decoupled LL phase [the Gaussian theory given by Eq. (19)], critical properties of the metal-insulator (MI) and reentrant insulator-metal (IM) transitions are characterized by a new saddle-point fixed point (schematically denoted by "FP4" in Fig. 11), rather than by the FP1 that leads to the argument in Sec. VI C. Meanwhile, having a finite charge gap, a fixed point of the excitonic insulator (EI) is expected to be locally stable against the small perturbation. Thereby, the primary features of the two EI phases discussed in the paper will not change dramatically even in the presence of such perturbations. These features include the finite mobility gaps in $\sigma_{zz}(\omega)$ in the two SNEI phases, an overall structure of the H-T phase diagram, as well as the topological Dirac-cone surface state in the SNEI-II phase and in-plane electric transport due to the surface state.

B. Excitonic BCS-BEC crossover and nature of the transition between SNEI-I and SNEI-II phases

Our theory does not include the effect of excitonic condensation, as emphasized in Ref. [20]. When H approaches H_0 from above ($H > H_0$), electron-hole bound states formed
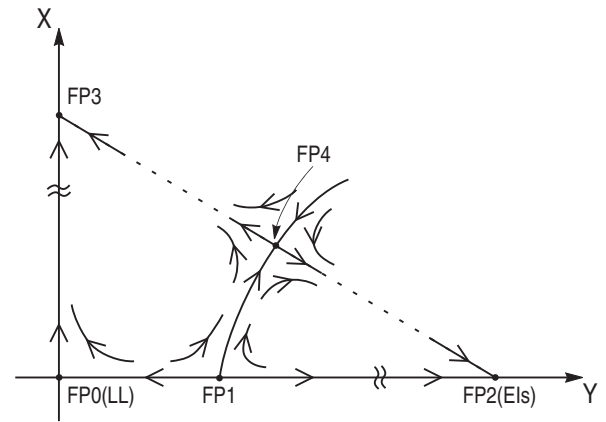

FIG. 11. Schematic picture of a possible RG phase diagram in the presence of a relevant perturbation (denoted by X) around the decoupled Luttinger liquid (LL) fixed point (denoted by "FP0"). In the presence of such relevant perturbation, the LL fixed point is unstable; the normal metal phase is characterized by a new stable fixed point (denoted by "FP3"). The horizontal axis (Y) denotes the umklapp and interpocket scattering terms that drive the system into the excitonic insulator (EI) phases. FP2 represents a stable fixed point characterizing the EI phases. The critical properties of the metal-insulator (MI) and reentrant insulator-metal (IM) transitions are characterized by a new saddle fixed point (denoted by "FP4") instead of by the FP1. In this schematic picture, we assume that the fixed point for the EI phases (FP2) is locally stable against the small perturbation X.

by an electron in the $(n, \sigma) = (0, \uparrow)$ LL and a hole in the $(n, \sigma) = (-1, \downarrow)$ LL can undergo Bose-Einstein condensation. Such condensation further assists electron-hole BCS pairings between $(n, \sigma) = (0, \downarrow)$ and $(n, \sigma) = (-1, \uparrow)$ LLs, through the umklapp term $H_{u,2}$. This leads to a phase with electrically insulating behavior along the field direction; the phase is essentially same as the SNEI-I phase discussed in the paper. When the exciton BEC effect is included in our theory, the phase boundary between SNEI-I and SNEI-II phases (say $H = H_{c,3}$) will presumably go above H_0 ($H_0 < H_{c,3}$).

For $H \geqslant H_{c,3}$, the long-range phase coherences defined by $\theta_{4,j} - \theta_{1,j} = n\pi - \Theta_-$ and $\phi_{4,j} + \phi_{1,j} = (m + 1)\pi - \Phi_-$ in Eqs. (45) and (46) fade away, while the other long-range phase coherences defined by $\theta_{3,j} - \theta_{2,j} = \Theta_-$ and $\phi_{3,j} + \phi_{2,j} = \Phi_-$ may survive, leading to a phase similar to the spin nematic excitonic insulator phase discussed in Sec. VI B. From this viewpoint, the SNEI-II phase could be regarded as a "partially ordered phase" derived from the SNEI-I phase. Nonetheless, it can be entirely possible that these two SNEI phases are symmetrically distinct from each other, depending on the spatial parities of the excitonic pairings in the two phases, whose importance was emphasized in Sec. VIII A. The qualitative nature of the phase transition between these two excitonic insulator phases needs further theoretical studies.

APPENDIX A: CHARGE NEUTRALITY CONDITION

Transverse conductivity σ_{xy} gives precise information on electron carrier density n_e and hole carrier density n_h in any given metal and semimetal under high magnetic field through the following formula:

$$\sigma_{xy}H = ec(n_e - n_h). \tag{A1}$$

e (> 0) and c are the electron charge and the speed of light, respectively. In the main text, we use the formula and evaluate the total number of k_z points in the electron/hole pockets N_e/N_h in graphite under the field. With the formula, the previous Hall conductivity measurement in the regime of 20 T $\lesssim H \lesssim$ 55 T [18,35–37] gives $(N_e - N_h) : L_z/c_0 = 10^{-4} : 1$. Using the Kubo formula of the Hall conductivity, Akiba discussed the validity of the formula in the quasi-quantum limit in graphite [18]. In the following, we employ Buttiker's theory of Hall conductivity [68,69] to demonstrate the validity of the formula in a generic three-dimensional metal and semimetal under high field.

Use the Landau gauge and assume that a given three-dimensional system is translationally symmetric along the x and z directions. Electrons are confined along the y direction within $|y| < L_y/2$ by a confining potential. A single-particle Hamiltonian comprises two parts:

$$\hat{\mathcal{H}}_T \equiv \hat{\mathcal{H}}_0(k_z; \hat{\kappa}_\pm) + \hat{\mathcal{V}}(k_z; \hat{\kappa}_\pm, \hat{y}), \tag{A2}$$

with $\kappa_\pm \equiv (-i\partial_y) \pm i(-k_x + \frac{eHy}{c\hbar})$. $\hat{\mathcal{H}}_0$ is a bulk Hamiltonian that depends on the coordinate y through $\hat{\kappa}_+$ and $\hat{\kappa}_-$. $\hat{\mathcal{V}}$ describes the effect of the confining potential; $\hat{\mathcal{V}} \equiv 0$ when $|y| \ll L_y/2$. $\hat{\mathcal{V}}$ depends on y explicitly. $\hat{\mathcal{H}}_T$ in Eq. (A2) is already Fourier-transformed with respect to x and z: they are functions of the conjugate momenta k_x and k_z. In a system with multiple energy bands, $\hat{\mathcal{H}}_T$ takes a matrix form. For the spinless graphite case, $\hat{\mathcal{H}}_T$ is a 4×4 matrix; the four bases are from the π orbitals in the A, A', B, and B' carbon atoms within the unit cell. Using the $\boldsymbol{k} \cdot \boldsymbol{p}$ expansion, Slonczewski, Weiss, and McClure derived $\mathcal{H}_0$ around the zone boundary of the first Brillouin zone of graphite.

In the following, we only assume that $\mathcal{H}_0(k_z; \kappa_\pm)$ as well as $\mathcal{V}(k_z; \kappa_\pm, y)$ are given by finite-order polynomials in $\kappa_\pm$ and y. Under this assumption, the explicit y dependence of $\mathcal{V}$ can be rewritten into the y_c dependence by use of $y \equiv (-i)(l^2/2)(\kappa_+ - \kappa_-) + y_c$ and $y_c \equiv k_x l^2$:

$$\hat{\mathcal{H}}_T(k_z; \hat{\kappa}_\pm, \hat{y}) = \hat{\mathcal{H}}_T'(k_z, y_c; \hat{\kappa}_\pm). \tag{A3}$$

Eigenstates of such $\hat{\mathcal{H}}_T$ are localized in the y coordinate at $y = y_c$. Eigenvalues depend on k_z, y_c, and the Landau index n:

$$\hat{\mathcal{H}}_T \phi_{n,k_z,y_c}(y - y_c) = E_n(k_z, y_c)\phi_{n,k_z,y_c}(y - y_c). \tag{A4}$$

A single-particle velocity operator along x is given by a k_x derivative of $\hat{\mathcal{H}}_T$. With $k_x l^2 \equiv y_c$, an expectation value of the velocity with respect to the eigenstate is given by a y_c derivative of the eigenvalue. Besides, the eigenstate is

uniformly extended along x. Thus, an electric current carried by the eigenstate is given by

$$J_{x,n,k_z,y_c} = \frac{(-e)l^2}{\hbar L_x}\frac{\partial E_n(k_z, y_c)}{\partial y_c}. \tag{A5}$$

The total current density from the nth Landau level is the sum of J_{x,n,k_z,y_c} over all the filled k_z and $k_x \equiv y_c/l^2$ points:

$$j_x = \frac{1}{L_z L_y}\sum_{k_z}\sum_{k_x} J_{x,n,k_z,y_c} f_T(E_n(k_z, y_c))$$

$$= \frac{(-e)}{\hbar L_y}\int_{-\frac{\pi}{c_0}}^{\frac{\pi}{c_0}}\frac{dk_z}{2\pi}\int_{-\infty}^{+\infty}\frac{dy_c}{2\pi}\frac{\partial E_n}{\partial y_c}f_T(E_n(k_z, y_c)). \tag{A6}$$

$f_T(E)$ is a Fermi distribution function. At zero temperature, this reduces to a step function,

$$f_{T=0}(E_n) = \begin{cases} \theta(\mu_+ - E_n(k_z, y_c)) & (y_c \simeq L_y/2), \\ \theta(\mu_- - E_n(k_z, y_c)) & (y_c \simeq -L_y/2). \end{cases} \tag{A7}$$

$\mu_\pm$ are Fermi levels around $y = \pm L_y/2$, respectively. In the presence of the Hall voltage V_H in the $+y$ direction, $\mu_+ - \mu_- = -eV_H$.

In graphite under the high field, the two electron/hole pockets in the bulk region ($n = 0/n = -1$ LLs with $\uparrow$ and $\downarrow$ spins) end up with two electron/hole surface chiral Fermi arc (SCFA) states in the boundary region. Namely, $E_{n=0/-1,\sigma}(k_z, y_c)$ increases/decreases in energy, when y_c goes from the bulk region to the boundary region (Fig. 2):

$$\begin{aligned} E_{n=0,\sigma}(k_z, y_c) \nearrow \quad (|y_c| \nearrow), \\ E_{n=-1,\sigma}(k_z, y_c) \searrow \quad (|y_c| \nearrow). \end{aligned} \tag{A8}$$

Accordingly, the current density induced by the finite Hall voltage comprises two parts that cancel each other:

$$j_x = -\frac{e}{h}\frac{(\mu_+ - \mu_-)}{L_y}\left(\int_{-k_1}^{k_1}\frac{dk_z}{2\pi} + \int_{-k_2}^{k_2}\frac{dk_z}{2\pi}\right)$$

$$- \frac{e}{h}\frac{(\mu_- - \mu_+)}{L_y}\left(\int_{k_3}^{\frac{2\pi}{c_0}-k_3}\frac{dk_z}{2\pi} + \int_{k_4}^{\frac{2\pi}{c_0}-k_4}\frac{dk_z}{2\pi}\right). \tag{A9}$$

The first part is from the two electron surface states that subtend chiral arcs from $k_z = -k_1$ to $k_z = k_1$ and from $k_z = -k_2$ to $k_z = k_2$, respectively. The other part is from the two hole surface states that subtend chiral arcs from $k_z = k_3$ to $2\pi/c_0 - k_3$ and from $k_z = k_4$ to $k_z = 2\pi/c_0 - k_4$, respectively (Fig. 2). To have Eq. (A9), we assume that the hole pocket energies are the same in the vacuum,

$$E_{n=-1,\sigma}(k_z, y_c = -\infty) = E_{n=-1,\sigma}(k_z, y_c = +\infty). \tag{A10}$$

Equation (A9) gives the Hall conductivity as

$$\sigma_{xy} = \frac{e^2}{h}\frac{1}{L_z}(N_1 + N_2 - N_3 - N_4) = \frac{ec}{H}(n_e - n_h), \tag{A11}$$

with $(N_1 + N_2)/L_z = 2\pi l^2 n_e$ and $(N_3 + N_4)/L_z = 2\pi l^2 n_h$. From the previous Hall conductivity measurement [18], we typically have

$$n_e - n_h = 5 \times 10^{15} \text{ cm}^{-3},$$

for $H = 30$ T, and

$$n_e - n_h = -10 \times 10^{15} \text{ cm}^{-3},$$

for $H = 55$ T. With $c_0 = 6.7 \times 10^{-10}$m, this gives the ratio between $N_e - N_h$ and L_z/c_0 as

$$N_e - N_h : L_z/c_0 = \pm 3 \times 10^{-4} : 1 \qquad \text{(A12)}$$

for 30 T $< H < 55$ T. From this very small number, we conclude that graphite under this field regime safely satisfies the charge neutrality condition.

APPENDIX B: RENORMALIZATION OF LUTTINGER PARAMETERS AND FERMI VELOCITIES

In the main text, we use the Hartree-Fock approximation for the four-pocket model or two-pocket model, to introduce effective boson Hamiltonians, such as Eqs. (18)–(21) with Eqs. (22)–(25) and (27)–(29) or with Eqs. (60)–(63). Thereby, the bare kinetic energy part takes a quadratic form in the phase variables, Eq. (19), whose coefficients (Luttinger parameters and Fermi velocities) are further renormalized by intrapocket forward scattering terms. In the following, we summarize how the intrapocket forward scattering terms renormalize the Luttinger parameters and Fermi velocities.

The electron interaction within the same pockets is given by

$$H_f = \sum_{j,m,n} \sum_{a=1,2,3,4\ (2,3)} \int dz \int dz' e^{-\frac{(z-z')^2}{2l_{0,z}^2}} V_{n-m,n-j}^{(1),a}$$
$$\times \psi_{a,n}^\dagger(z)\psi_{a,j+m-n}^\dagger(z')\psi_{a,m}(z')\psi_{a,j}(z), \qquad \text{(B1)}$$

with $\psi_{a,n}(z) \equiv e^{ik_{F,a}z}\psi_{a,+,n}(z) + e^{-ik_{F,a}z}\psi_{a,-,n}(z)$. The matrix element $V_{n,m}^{(1),a}$ ($a = 1, 2, 3, 4$) is obtained by the substitutions of Eqs. (7)–(10) into Eq. (6). In the limit of short interaction length ($l_{0,z} \ll l$), the matrix element takes the form of

$$V_{n,m}^{(1),a} \equiv \frac{g}{L_x}\frac{1}{l_{0,z}l} f^{(1),a}(y_n/l, y_m/l). \qquad \text{(B2)}$$

Dimensionless functions $f^{(1),a}(x, y)$ decay quickly for $|x|, |y| \gg 1$. With the Hartree-Fock approximation, H_f is bosonized into the following:

$$H_f = \sum_a \sum_{j,m} \int dz \sqrt{2\pi} l_{0,z} (V_{j-m,0}^{(1),a} - V_{0,j-m}^{(1),a})$$
$$\times (\rho_{a,+,j}\rho_{a+,m} + \rho_{a,-,j}\rho_{a,-,m})$$
$$+ \sum_a \sum_{j,m} \int dz \sqrt{2\pi} l_{0,z} (V_{j-m,0}^{(1),a} - V_{0,j-m}^{(1),a}e^{-2(k_{F,a}l_{0,z})^2})$$
$$\times (\rho_{a,+,j}\rho_{a-,m} + \rho_{a,-,j}\rho_{a,+,m})$$
$$+ 2\sum_a \sum_{j,m} \int dz \sqrt{2\pi} l_{0,z} (V_{j-m,0}^{(1),a}e^{-2(k_{F,a}l_{0,z})^2} - V_{0,j-m}^{(1),a})$$
$$\times \eta_{a,+,j}\eta_{a,-,j}\eta_{a,-,m}\eta_{a,+,m}\cos\{2[\phi_{a,j}(z) - \phi_{a,m}(z)]\},$$
$$+ \cdots, \qquad \text{(B3)}$$

where $\rho_{a,\pm,j}(z)$ stands for an electron density in the right $(+)$ or left $(-)$ branch in the ath pocket ($a = 1, 2, 3, 4$) of the jth chain ($j = 1, 2, \ldots, \frac{S}{2\pi l^2}$):

$$\rho_{a,\pm,j}(z) \equiv \psi_{a,\pm,j}^\dagger \psi_{a,\pm,j} = -\frac{1}{2\pi}(\partial_z \phi_{a,j} \mp \partial_z \theta_{a,j}). \qquad \text{(B4)}$$

The third term in Eq. (B3) represents a rigidity between two displacement fields in different chains in the same pocket. When the corresponding interchain interaction is negative definite, this could result in charge density wave orders with broken translational symmetry along the field direction. An interplay between this interchain rigidity term and one of the umklapp term is discussed for the two-pocket model case (see Sec. V).

The first two terms in Eq. (B3) lead to the renormalizations of the Luttinger parameters and Fermi velocities. To quantify them, we employ a gradient expansion with respect to the chain index,

$$\rho_{a,\tau,m} = \rho_{a,\tau,j} + (y_m - y_j)\partial_{y_j}\rho_{a,\tau,j}$$
$$+ \frac{1}{2}(y_m - y_j)^2 \partial_{y_j}^2 \rho_{a,\tau,j} + \cdots, \qquad \text{(B4)}$$

to keep only the leading order. This leads to

$$H_f = \sum_a \sum_j \int dz \left\{ \frac{g_{2,a} + g_{4,a}}{(2\pi)^2}(\partial_z \phi_{a,j})^2 \right.$$
$$\left. + \frac{-g_{2,a} + g_{4,a}}{(2\pi)^2}(\partial_z \theta_{a,j})^2 \right\} + \cdots, \qquad \text{(B5)}$$

with

$$g_{2,a} = 2\sqrt{2\pi} l_{0,z} \sum_m (V_{m,0}^{(1),a} - V_{0,m}^{(1),a}e^{-2(k_{F,a}l_{0,z})^2})$$
$$= \sqrt{\frac{2}{\pi}}\frac{g}{l^2} \int dx [f^{(1),a}(x, 0) - f^{(1),a}(0, x)e^{-2(k_{F,a}l_{0,z})^2}],$$
$$g_{4,a} = 2\sqrt{2\pi} l_{0,z} \sum_m (V_{m,0}^{(1),a} - V_{0,m}^{(1),a}) \qquad \text{(B6)}$$
$$= \sqrt{\frac{2}{\pi}}\frac{g}{l^2} \int dx [f^{(1),a}(x, 0) - f^{(1),a}(0, x)]. \qquad \text{(B7)}$$

When combined with the bare kinetic energy part,

$$H_{\text{kin}} = \sum_{a,j} \frac{v_{F,a}}{2\pi} \int dz \{(\partial_z \phi_{a,j})^2 + (\partial_z \theta_{a,j})^2\}, \qquad \text{(B8)}$$

Eq. (B5) gives Eq. (19) with Eqs. (20) and (21).

APPENDIX C: DERIVATION OF RENORMALIZATION GROUP EQUATIONS

In the main text, we employ one-loop RG equations, Eqs. (35)–(37), and clarify possible insulating phases as well as the nature of $T = 0$ metal-insulator and insulator-metal transition points in graphite under high field. We solve the RG equations numerically to obtain a finite-temperature phase diagram as in Fig. 1. The RG equations are derived perturbatively by use of the standard momentum-shell renormalization method [43]. In the following, we briefly summarize how to derive the one-loop RG equations for $H_{u,2}$ and $H_{b,2}$, Eqs. (35)–(37).

We begin with a partition function of the effective field theory:

$$Z = \sum_{\sigma\cdots} \int \mathcal{D}\phi \mathcal{D}\theta\, e^{-S_0[\phi,\theta] - S_1[\phi,\theta]}. \qquad \text{(C1)}$$

An action S comprises a Gaussian part S_0 and non-Gaussian part S_1:

$$S_0 = \int_0^\beta d\tau \int dz \sum_{a,j} \frac{1}{2\pi} \left\{ -2i\, \partial_z \theta_{a,j}(\boldsymbol{r}) \partial_\tau \phi_{a,j}(\boldsymbol{r}) \right.$$

$$\left. + u_a K_a [\partial_z \theta_{a,j}(\boldsymbol{r})]^2 + \frac{u_a}{K_a} [\partial_z \phi_{a,j}(\boldsymbol{r})]^2 \right\}, \quad \text{(C2)}$$

$$S_1 = \int_0^\beta d\tau \{ H_{u,2} + H_{b,2} + \cdots \}. \quad \text{(C3)}$$

Here a is the pocket index ($a = 1, 2, 3, 4$). The summation over Ising variables $\sigma_{...}$ represent traces over the two-dimensional spaces subtended by two Klein factors associated with the bosonization. With $\boldsymbol{r} = (z, \tau)$, $\boldsymbol{q} = (k_z, i\omega_n)$, and Matsubara frequency $\omega_n = 2n\pi/\beta$, the Fourier transforms of $\phi_{j,a}(z, \tau)$ and $\theta_{j,a}(z, \tau)$ are given by

$$\phi_{j,a}(\boldsymbol{r}) = \frac{1}{\beta L_z} \sum_{i\omega_n} \sum_{|k_z| < \Lambda} e^{ik_z z - i\omega_n \tau} \phi_{j,a}(\boldsymbol{q}). \quad \text{(C4)}$$

Λ is a cutoff in momentum space. We decompose the field operators into a slow mode and a fast mode in momentum space,

$$\phi_{j,a}(\boldsymbol{r}) = \phi_{j,a}^<(\boldsymbol{r}) + \phi_{j,a}^>(\boldsymbol{r}),$$

$$\phi_{j,a}^<(\boldsymbol{r}) = \frac{1}{\beta L_z} \sum_{i\omega_n} \sum_{|k_z| < \Lambda'} e^{i\boldsymbol{q}\cdot\boldsymbol{r}} \phi_{j,a}(\boldsymbol{q}),$$

$$\phi_{j,a}^>(\boldsymbol{r}) = \frac{1}{\beta L_z} \sum_{i\omega_n} \sum_{\Lambda' < |k_z| < \Lambda} e^{i\boldsymbol{q}\cdot\boldsymbol{r}} \phi_{j,a}(\boldsymbol{q}),$$

with $\Lambda' = \Lambda b^{-1}$. $b\ (> 1)$ denotes a scale change.

First integrate out the fast mode $\phi^>$ and $\theta^>$ in the partition function and rescale spatial and temporal length scales as

$$z_{\text{new}} = z_{\text{old}} b^{-1}, \quad \tau_{\text{new}} = \tau_{\text{old}} b^{-1}, \quad \beta_{\text{new}} = \beta_{\text{old}} b^{-1}. \quad \text{(C5)}$$

This gives a partition function for the slow mode. The partition function takes essentially the same form as Eqs. (C2) and (C3), while the interchain interactions in Eq. (C3) are renormalized. The renormalization is calculated with respect to an infinitesimally small scale change $\ln b\ (\ll 1)$. This gives the RG equations for the interactions as in Eqs. (35)–(37).

We derive the partition function for the slow mode perturbatively in the non-Gaussian part S_1. We do so up to the second order in S_1:

$$Z = Z_0^> \int \mathcal{D}\phi^< \mathcal{D}\theta^< e^{-S_0^<} e^{-\langle S_U \rangle_>} + O(S_i^3), \quad \text{(C6)}$$

where

$$\langle S_U \rangle_> = \langle S_1 \rangle_> - \frac{1}{2} \left(\langle S_1^2 \rangle_> - \langle S_1 \rangle_>^2 \right) \quad \text{(C7)}$$

and

$$\langle \cdots \rangle_> = \frac{1}{Z_0^>} \int \mathcal{D}\phi^> \mathcal{D}\theta^> \cdots e^{-S_0^>},$$

$$S_0^< = \frac{1}{2\beta L_z} \sum_{a,j} \sum_{i\omega_n} \sum_{|k_z| < \Lambda'} \cdots,$$

$$S_0^> = \frac{1}{2\beta L_z} \sum_{a,j} \sum_{i\omega_n} \sum_{\Lambda' < |k_z| < \Lambda} \cdots,$$

with $Z_0^> = \langle 1 \rangle_>$. "$\cdots$" on the right-hand sides of $S_0^{</>}$ is a Fourier transform of the integrand in Eq. (C2). The first term in Eq. (C7) gives a tree-level renormalization to the interchain interactions, while the second term gives a one-loop level renormalization.

1. Tree-level renormalization

$\langle S_1 \rangle_>$ in Eq. (C7) gives the tree-level renormalization to the interchain interactions:

$$\left\langle \int_0^\beta H_{u,2} d\tau \right\rangle_> = \frac{1}{2} \int d^2\boldsymbol{r} \sum_{j,m} \sum_{\epsilon=\pm} \sum_{\eta=\pm}$$

$$\times M_{j-m}^{(2)} \sigma_j^\eta \tau_m^\eta e^{i\epsilon M_{jm}^{\eta,<}(\boldsymbol{r})} e^{-\frac{1}{2}\langle M_{jm}^{\eta,>}(\boldsymbol{r})^2 \rangle_>}, \quad \text{(C8)}$$

$$\left\langle \int_0^\beta H_{b,2} d\tau \right\rangle_> = \frac{1}{2} \int d^2\boldsymbol{r} \sum_{j\neq m} \sum_{\epsilon=\pm} \sum_{\eta=\pm} \left\{ H_{j-m}^{(2)} \sigma_j^\eta \right.$$

$$\times \sigma_m^\eta e^{i\epsilon H_{jm}^{\eta,<}(\boldsymbol{r})} e^{-\frac{1}{2}\langle H_{jm}^{\eta,>}(\boldsymbol{r})^2 \rangle_>}$$

$$\left. + \overline{H}_{j-m}^{(2)} \tau_j^\eta \tau_m^\eta e^{i\epsilon \overline{H}_{jm}^{\eta,<}(\boldsymbol{r})} e^{-\frac{1}{2}\langle \overline{H}_{jm}^{\eta,>}(\boldsymbol{r})^2 \rangle_>} \right\}, \quad \text{(C9)}$$

where

$$M_{jm}^\eta(\boldsymbol{r}) \equiv Q_{\eta,j}^{23}(\boldsymbol{r}) + Q_{\eta,m}^{14}(\boldsymbol{r}),$$

$$H_{jm}^\eta(\boldsymbol{r}) \equiv Q_{\eta,j}^{23}(\boldsymbol{r}) - Q_{\eta,m}^{23}(\boldsymbol{r}),$$

$$\overline{H}_{jm}^\eta(\boldsymbol{r}) \equiv Q_{\eta,j}^{14}(\boldsymbol{r}) - Q_{\eta,m}^{14}(\boldsymbol{r}),$$

and

$$\sigma_j^+ \equiv \sigma_{3\bar{2},j}, \quad \sigma_j^- \equiv \sigma_{\bar{3}2,j}, \quad \tau_j^+ \equiv \sigma_{4\bar{1},j}, \quad \tau_j^- \equiv \sigma_{\bar{4}1,j}.$$

As the leading order in the infinitesimally small $\ln b$, we obtain

$$\langle M_{jm}^{\eta,>}(\boldsymbol{r})^2 \rangle_> = \sum_{a=1,2,3,4} \frac{1}{2} \left(K_a + \frac{1}{K_a} \right) \coth \frac{\beta u_a \Lambda}{2} \ln b,$$

$$\langle H_{jm}^{\eta,>}(\boldsymbol{r})^2 \rangle_> = 2 \sum_{a=2,3} \frac{1}{2} \left(K_a + \frac{1}{K_a} \right) \coth \frac{\beta u_a \Lambda}{2} \ln b,$$

$$\langle \overline{H}_{jm}^{\eta,>}(\boldsymbol{r})^2 \rangle_> = 2 \sum_{a=1,4} \frac{1}{2} \left(K_a + \frac{1}{K_a} \right) \coth \frac{\beta u_a \Lambda}{2} \ln b.$$

This leads to the tree-level RG equation as

$$\frac{dM_{j-m}^{(2)}}{d\ln b} = \left[2 - \frac{1}{4} \sum_{a=1,2,3,4} \left(K_a + \frac{1}{K_a} \right) \coth \frac{u_a \Lambda}{2T} \right] M_{j-m}^{(2)},$$

$$\frac{dH_{j-m}^{(2)}}{d\ln b} = \left[2 - \frac{1}{2} \sum_{a=2,3} \left(K_a + \frac{1}{K_a} \right) \coth \frac{u_a \Lambda}{2T} \right] H_{j-m}^{(2)},$$

$$\frac{d\overline{H}_{j-m}^{(2)}}{d\ln b} = \left[2 - \frac{1}{2} \sum_{a=1,4} \left(K_a + \frac{1}{K_a} \right) \coth \frac{u_a \Lambda}{2T} \right] \overline{H}_{j-m}^{(2)}.$$

2. One-loop level renormalization

$\langle S_1^2 \rangle_{>,c} \equiv \langle S_1^2 \rangle_> - \langle S_1 \rangle_>^2$ in Eq. (C7) gives the one-loop level renormalization to the interchain interactions. The one-loop renormalization comprises products between different

interactions:

$$S_1 = S_M + S_H + S_{\overline{H}} + \cdots ,$$

$$S_1^2 = S_M^2 + S_H^2 + S_{\overline{H}}^2 + 2S_M S_H + 2S_M S_{\overline{H}} + 2S_H S_{\overline{H}} + \cdots ,$$

(C10)

where S_M, S_H, and $S_{\overline{H}}$ are defined as follows:

$$S_I \equiv \frac{1}{2} \int d^2 \boldsymbol{r} \sum_{j \neq m} \sum_{\epsilon = \pm} \sum_{\eta = \pm} I_{j-m}^{(2)} (\cdots)_j^\eta (\cdots)_m^\eta$$

$$\times e^{i \epsilon I_{jm}^{\eta,<}(\boldsymbol{r})} e^{i \epsilon I_{jm}^{\eta,>}(\boldsymbol{r})},$$

(C11)

with $I = M, H, \overline{H}$. The products of two interaction terms take forms of

$$\langle S_I S_J \rangle_{>,c} = \frac{1}{4} \int d^2 \boldsymbol{r} \int d^2 \boldsymbol{r}' \sum_{i \neq j} \sum_{m \neq n} \sum_{\epsilon, \epsilon', \eta, \eta'} I_{i-j}^{(2)} J_{m-n}^{(2)}$$

$$\times (\cdots)_i^\eta (\cdots)_j^\eta (\cdots)_m^{\eta'} (\cdots)_n^{\eta'} \left\langle e^{i \epsilon I_{ij}^\eta(\boldsymbol{r})} e^{i \epsilon' J_{mn}^{\eta'}(\boldsymbol{r}')} \right\rangle_{>,c},$$

(C12)

where $\langle AB \rangle_{>,c} \equiv \langle AB \rangle_> - \langle A \rangle_> \langle B \rangle_>$. When $i \neq m, n$ and $j \neq m, n$ in Eq. (C12), the right-hand side vanishes identically. The terms with $i = m$ and $j = n$ or those with $i = n$ and $j = m$ are negligibly smaller than the others in the larger L_x limit. We thus consider only those terms in Eq. (C12) with $i = m, n$ and $j \neq m, n$ and/or those terms with $i \neq m, n$ and $j = m, n$.

The one-loop renormalization in Eq. (C12) generates S_M, S_H, and $S_{\overline{H}}$ as well as other types of cosine terms. Nonetheless, tree-level scaling dimensions of all the other cosine terms thus generated are negatively much larger than those of S_M, S_H, and $S_{\overline{H}}$. Namely, they are much more irrelevant than S_M, S_H, and $S_{\overline{H}}$ at the tree-level renormalization group flow. Thus, we only keep those terms in Eq. (C12) that generate S_M, S_H, and $S_{\overline{H}}$. S_M^2 with $\epsilon = -\epsilon'$, $\eta = \eta'$, and $i = m$ (or $j = n$) generates $S_{\overline{H}}$ (or S_H), respectively. S_H^2 ($S_{\overline{H}}^2$) with $\epsilon = -\epsilon'$, $\eta = \eta'$, and $i = m$ or $j = n$ or with $\epsilon = \epsilon'$, $\eta = \eta'$, and $i = n$ or $j = m$ generates S_H ($S_{\overline{H}}$), respectively. $S_M S_H$ ($S_M S_{\overline{H}}$) with $\epsilon = \epsilon'$, $\eta = \eta'$, and $i = n$ ($j = n$) or with $\epsilon = -\epsilon'$, $\eta = \eta'$, and $i = m$ ($j = m$) generates S_M. $S_H S_{\overline{H}}$ does not generate any of S_M, S_H, or $S_{\overline{H}}$. In the following, we only demonstrate how S_M^2 generates $S_{\overline{H}}$.

With $\epsilon = -\epsilon'$, $\eta = \eta'$, and $i = m$, Eq. (C12) with $I = J = M$ reduces to

$$\langle S_M^2 \rangle_{>,c} = \frac{1}{4} \int d^2 \boldsymbol{r} \int d^2 \boldsymbol{r}' \sum_{j,n}^{j \neq n} \sum_{i=m} \sum_{\epsilon, \eta} \tau_j^\eta \tau_n^\eta M_{i-j}^{(2)} M_{i-n}^{(2)}$$

$$\times e^{i \epsilon (M_{ij}^{\eta,<}(\boldsymbol{r}) - M_{in}^{\eta,<}(\boldsymbol{r}'))} \left\langle e^{i \epsilon M_{ij}^{\eta,>}(\boldsymbol{r})} e^{-i \epsilon M_{in}^{\eta,>}(\boldsymbol{r}')} \right\rangle_{>,c}$$

$$= \frac{1}{2} \int d^2 \boldsymbol{r} \int d^2 \boldsymbol{r}' \sum_{j,n}^{j \neq n} \sum_{i=m} \sum_{\epsilon, \eta} \tau_j^\eta \tau_n^\eta M_{i-j}^{(2)} M_{i-n}^{(2)}$$

$$\times \cos \left[M_{ij}^{\eta,<}(\boldsymbol{r}) - M_{in}^{\eta,<}(\boldsymbol{r}') \right] \left\langle M_{ij}^{\eta,>}(\boldsymbol{r}) M_{in}^{\eta,>}(\boldsymbol{r}') \right\rangle_>,$$

(C13)

where

$$\cos \left[M_{ij}^{\eta,<}(\boldsymbol{r}) - M_{in}^{\eta,<}(\boldsymbol{r}') \right]$$

$$= \cos \left[Q_{\eta,j}^{14,<}(\boldsymbol{r}) - Q_{\eta,n}^{14,<}(\boldsymbol{r}') \right] \cos \left[Q_{\eta,i}^{23,<}(\boldsymbol{r}) - Q_{\eta,i}^{23,<}(\boldsymbol{r}') \right]$$

$$- \sin \left[Q_{\eta,j}^{14,<}(\boldsymbol{r}) - Q_{\eta,n}^{14,<}(\boldsymbol{r}') \right]$$

$$\times \sin \left[Q_{\eta,i}^{23,<}(\boldsymbol{r}) - Q_{\eta,i}^{23,<}(\boldsymbol{r}') \right].$$

(C14)

The largest part of the contribution comes from $\boldsymbol{r} = \boldsymbol{r}'$. In this case, the second term in Eq. (C14) vanishes (see the next subsection for a justification of this approximation). For the first term with $j \neq n$, we replace $\cos[Q_{\eta,i}^{23,<}(\boldsymbol{r}) - Q_{\eta,i}^{23,<}(\boldsymbol{r}')]$ by its normal ordering with use of a formula $\cos \Phi =: \cos \Phi : \exp[-\langle \Phi^2 \rangle / 2]$ [43,70]. Within the normal order, we employ a Taylor expansion with respect to small $\boldsymbol{r}' - \boldsymbol{r}$. At the leading order expansion, Eq. (C14) becomes

$$\cos \left[M_{ij}^{\eta,<}(\boldsymbol{r}) - M_{in}^{\eta,<}(\boldsymbol{r}') \right] \simeq \cos \left[Q_{\eta,j}^{14,<}(\boldsymbol{r}) - Q_{\eta,n}^{14,<}(\boldsymbol{r}) \right]$$

$$\times e^{-\frac{1}{2} \langle [Q_{\eta,i}^{23,<}(\boldsymbol{r}) - Q_{\eta,i}^{23,<}(\boldsymbol{r}')]^2 \rangle_<}.$$

(C15)

Thereby, we have

$$\langle S_M^2 \rangle_{>,c} = \int d^2 \boldsymbol{r} \sum_{j,n}^{j \neq n} \sum_{\epsilon, \eta} \tau_j^\eta \tau_n^\eta \cos \left[\overline{H}_{jn}^{\eta,<}(\boldsymbol{r}) \right]$$

$$\times C_{23} \sum_i M_{i-j}^{(2)} M_{i-n}^{(2)} \ln b,$$

(C16)

where

$$C_{cd} \ln b \equiv \frac{1}{2} \int d\boldsymbol{r}' e^{-\frac{1}{2} \langle [Q_{\eta,i}^{cd,<}(\boldsymbol{r}) - Q_{\eta,i}^{cd,<}(\boldsymbol{r}')]^2 \rangle_<}$$

$$\times \left\langle Q_{\eta,i}^{cd,>}(\boldsymbol{r}) Q_{\eta,i}^{cd,>}(\boldsymbol{r}') \right\rangle_>,$$

(C17)

with $c, d = 1, 2, 3, 4$. Note that the integrand in Eq. (C17) is short-ranged in $\boldsymbol{r} - \boldsymbol{r}'$ and C_{cd} is a positive-definite real-valued quantity (see the next subsection). Equation (C16) in combination with Eqs. (C7) and (C10) dictates that $\overline{H}_{j-n}^{(2)}$ acquires the following one-loop renormalization,

$$\frac{d \overline{H}_{j-n}^{(2)}}{d \ln b} = \cdots - \frac{C_{23}}{2} \sum_i M_{i-j}^{(2)} M_{i-n}^{(2)} + \cdots .$$

(C18)

Since $M_{i-j}^{(2)} = M_{j-i}^{(2)}$, this is nothing but the first term of the one-loop renormalization in Eq. (37). Similarly, one can show all the other terms of the one-loop renormalizations in Eqs. (35)–(37). A factor 4 in the second term of the one-loop renormalization in Eq. (37) is due to the four distinct contributions to $S_{\overline{H}}$ from $S_{\overline{H}}^2$: (i) $\epsilon = -\epsilon'$, $\eta = \eta'$, $i = m$; (ii) $\epsilon = -\epsilon'$, $\eta = \eta'$, $j = n$; (iii) $\epsilon = \epsilon'$, $\eta = \eta'$, $i = n$; (iv) $\epsilon = \epsilon'$, $\eta = \eta'$, $j = m$ in Eq. (C12). Likewise, $2S_M S_H$ ($2S_M S_{\overline{H}}$) has two distinct contributions to S_M, giving rise to the first (second) term of the one-loop renormalization in Eq. (35): (i) $\epsilon = \epsilon'$,

$\eta = \eta'$, $i = n$ ($j = n$); (ii) $\epsilon = -\epsilon'$, $\eta = \eta'$, $i = m$ ($j = m$) in Eq. (C12). This completes the derivation of Eqs. (35)–(37).

3. Evaluation of C_{cd}

C_{ab} is defined in Eq. (C17). Let us first calculate the integrand in Eq. (C17):

$$\langle Q_{\eta,i}^{ab,>}(r) Q_{\eta,i}^{ab,>}(r') \rangle_> = \frac{1}{(\beta L_z)^2} \sum_{\Lambda' < |k_z| < \Lambda} \sum_{i\omega_n} e^{iq(r-r')} \langle Q_{\eta,i}^{ab,>}(q)^* Q_{\eta,i}^{ab,>}(q) \rangle_> , \langle [Q_{\eta,i}^{ab,<}(r) - Q_{\eta,i}^{ab,<}(r')]^2 \rangle_<$$

$$= \frac{1}{(\beta L_z)^2} \sum_{|k_z| < \Lambda'} \sum_{i\omega_n} 2(1 - e^{iq(r-r')}) \langle Q_{\eta,i}^{ab,<}(q)^* Q_{\eta,i}^{ab,<}(q) \rangle_< ,$$

where

$$\langle Q_{\eta,i}^{ab,>/<}(q)^* Q_{\eta,i}^{ab,>/<}(q) \rangle_{>/<} = \sum_{c=a,b} \{ \langle \phi_{c,i}^*(q)\phi_{c,i}(q) \rangle_{>/<} + \langle \theta_{c,i}^*(q)\theta_{c,i}(q) \rangle_{>/<}$$

$$+ \eta(-1)^c [\langle \phi_{c,i}^*(q)\theta_{c,i}(q) \rangle_{>/<} + \langle \theta_{c,i}^*(q)\phi_{c,i}(q) \rangle_{>/<}] \}, \tag{C19}$$

with $(-1)^a = 1$ and $(-1)^b = -1$. We used the Fourier transform in Eq. (C4). The Gaussian integrals over the fast/slow modes lead to

$$\langle \phi_{c,i}^*(q)\phi_{c,i}(q) \rangle_{>/<} = \frac{\beta L_z \pi u_c K_c}{u_c^2 k_z^2 + \omega_n^2}, \quad \langle \theta_{c,i}^*(q)\theta_{c,i}(q) \rangle_{>/<} = \frac{\beta L_z \pi u_c K_c^{-1}}{u_c^2 k_z^2 + \omega_n^2}, \quad \langle \phi_{c,i}^*(q)\theta_{c,i}(q) \rangle_{>/<} = -\frac{\beta L_z i \pi \omega_n}{k_z(u_c^2 k_z^2 + \omega_n^2)}.$$

Accordingly, we have

$$\langle Q_{\eta,i}^{ab,>}(r) Q_{\eta,i}^{ab,>}(r') \rangle_> = \frac{1}{2} \sum_{c=a,b} (K_c + K_c^{-1}) M_c(r - r') + \sum_{c=a,b} \eta(-1)^c F_{2,c}'(r - r'),$$

$$\langle [Q_{\eta,i}^{ab,<}(r) - Q_{\eta,i}^{ab,<}(r')]^2 \rangle_< = \frac{1}{2} \sum_{c=a,b} (K_c + K_c^{-1}) F_{1,c}(r - r') + \sum_{c=a,b} \eta(-1)^c F_{2,c}(r - r'), \tag{C20}$$

with

$$M_c(r) \equiv \int_{\Lambda' < |k_z| < \Lambda} dk_z \frac{1}{\beta} \sum_{i\omega_n} \frac{u_c e^{iqr}}{\omega_n^2 + u_c^2 k_z^2} = \cos(\Lambda z) e^{-u_c \Lambda |\tau|} \ln b,$$

$$F_{2,c}'(r) \equiv -\int_{\Lambda' < |k_z| < \Lambda} dk_z \frac{1}{\beta} \sum_{i\omega_n} \frac{i\omega_n}{k_z} \frac{e^{iqr}}{\omega_n^2 + u_c^2 k_z^2} = -i \, \text{sgn}(\tau) \sin(\Lambda z) e^{-u_c \Lambda |\tau|} \ln b,$$

$$F_{1,c}(r) \equiv \int_{|k_z| < \Lambda'} dk_z \frac{1}{\beta} \sum_{i\omega_n} \frac{2[1 - \cos(qr)] u_c}{\omega_n^2 + u_c^2 k_z^2} = \ln [(x^2 + y_c^2)/\alpha^2],$$

$$F_{2,c}(r) \equiv \int_{|k_z| < \Lambda'} dk_z \frac{1}{\beta} \sum_{i\omega_n} \frac{i\omega_n}{k_z} \frac{2 \cdot e^{iqr}}{\omega_n^2 + u_c^2 k_z^2} = 2i \, \text{Arg}[y_c + ix] \equiv 2i\theta_c(r),$$

and $y_c \equiv u_c \tau + \alpha \, \text{sgn}(\tau)$. On the right-hand side, $M_c(r)$, $F_{2,c}'(r)$, $F_{1,c}(r)$, and $F_{2,c}(r)$ are evaluated at zero temperature. Substituting these into Eq. (C17), we obtain C_{ab} at $T = 0$ as

$$C_{ab,T=0} = \sum_{c=a,b} \int_{-\infty}^{\infty} d\tau \int_{-\infty}^{\infty} dz \left(\frac{\alpha^2}{z^2 + y_a^2} \right)^{\lambda_a} \left(\frac{\alpha^2}{z^2 + y_b^2} \right)^{\lambda_b}$$

$$\times e^{-u_c \Lambda |\tau|} \left\{ \lambda_c \cos(\Lambda z) \cos[\Delta_{ab}(r)] + \frac{\eta}{2}(-1)^c \sin(\Lambda z) \text{sgn}(\tau) \sin[\Delta_{ab}(r)] \right\}$$

$$\simeq \sum_{c=a,b} \lambda_c \int_{-\infty}^{\infty} d\tau \, e^{-u_c \Lambda |\tau|} \int_{-\infty}^{\infty} dz \left(\frac{\alpha^2}{z^2 + y_a^2} \right)^{\lambda_a} \left(\frac{\alpha^2}{z^2 + y_b^2} \right)^{\lambda_b} \cos(\Lambda z), \tag{C21}$$

with $y_c^2 \equiv (u_c|\tau| + \alpha)^2$, $\lambda_a \equiv \frac{1}{4}(K_a + K_a^{-1})$, and $\Delta_{ab}(r) \equiv \theta_a(r) - \theta_b(r)$. The integrand on the first line is short-ranged in r, justifying *a posteriori* the approximations made in Eqs. (C14) and (C15). Based on the same spirit,

we approximate $\Delta_{ab}(r)$ by zero, to obtain the second line.

C_{ab} is positive definite. One can show this by carrying out the z-integral formally,

$$C_{ab,T=0} = \sum_{c=a,b} \lambda_c \int_{-\infty}^{\infty} d\tau\, G(\tau) e^{-u_c \Lambda |\tau|}, \qquad (C22)$$

and

$$G(\tau) \equiv \int_{-\infty}^{\infty} d\xi\, F_a(\xi;\tau) F_b(\Lambda - \xi;\tau) d\xi, \qquad (C23)$$

$$F_a(\xi;\tau) \equiv \int_{-\infty}^{\infty} dz\, e^{i\xi z} \left(\frac{\alpha^2}{z^2 + y_a^2}\right)^{\lambda_a},$$

$$= 2\sqrt{\pi}\alpha^{2\lambda_a} \left(\frac{|\xi|}{2|y_a|}\right)^{\lambda_a - \frac{1}{2}} \frac{K_{\lambda_a - \frac{1}{2}}(|y_a||\xi|)}{\Gamma(\lambda_a)}, \quad (C24)$$

with the Bessel function $K_\nu(x)$ and the Gamma function $\Gamma(x)$. Since $\lambda_a > 1/2$, $F_a(\xi,\tau)$ is positive definite and so is $G(\tau)$. With Eq. (C22), this assures the positive definiteness of $C_{ab,T=0}$.

$C_{ab,T=0}$ in Eq. (C21) depends on the Luttinger parameters K_a and K_b. Nonetheless, the dependence is much weaker than that of A_{ab} in Eq. (38). One can see this by evaluating an upper bound of $C_{ab,T=0}$,

$$C_{ab,T=0} < \sum_{c=a,b} \lambda_c \int dz \left(\frac{\alpha^2}{z^2 + \alpha^2}\right)^{\lambda_a + \lambda_b} \int d\tau\, e^{-u_c \Lambda |\tau|}$$

$$= \sum_{c=a,b} \frac{\alpha \lambda_c}{\Lambda_{\mathcal{E}}} \frac{\Gamma\left(\frac{1}{2}\right)\Gamma\left(\lambda_a + \lambda_b - \frac{1}{2}\right)}{\Gamma(\lambda_a + \lambda_b)} \equiv C_u.$$

$\Lambda_{\mathcal{E}}$ denotes a *finite* high-energy cutoff in the energy scale, $\Lambda_{\mathcal{E}} = \Lambda \times \max_{c=a,b}(u_c)$. When the Luttinger parameters get much smaller/larger than 1, $\lambda_a + \lambda_b \to +\infty$, the upper bounds of $C_{ab,T=0}$ as well as $|A_{ab,T=0}|$ diverge:

$$C_u \to \frac{\alpha}{\Lambda_{\mathcal{E}}} \Gamma\left(\frac{1}{2}\right)(\lambda_a + \lambda_b)^{\frac{1}{2}}, \quad |A_{ab,T=0}| \to 2(\lambda_a + \lambda_b).$$
$$(C25)$$

Meanwhile, $C_{ab,T=0}/|A_{ab,T=0}|$ goes to the zero in the limit of $\lambda_a + \lambda_b \to +\infty$. For simplicity, we assume that $C_{ab,T=0}$ does not depend on the magnetic field H in the main text. A typical value of $C_{ab,T=0}$ is evaluated in a simple case with $K_a = K_b = 1$ and $u_a = u_b = u$:

$$C_{ab,T=0,K_{a,b}=1,u_{a,b}=u}$$

$$= \int d\tau\, e^{-u\Lambda|\tau|} \int dz \frac{\alpha^2}{z^2 + (u|\tau| + \alpha)^2} e^{i\Lambda z}$$

$$= e^{-\Lambda\alpha} \frac{2\alpha^2}{u} \int_0^{\infty} dx \frac{e^{-2\Lambda x}}{x + \alpha} = e^{\Lambda\alpha} \frac{2\alpha^2}{u} E_1(2\Lambda\alpha). \quad (C26)$$

$E_1(x)$ is the exponential integral. α is a lattice constant along the z direction while Λ is a high-energy cutoff in momentum space: $\Lambda\alpha = O(1)$.

4. Parameters used in Fig. 1

To obtain the theoretical phase diagram at finite temperature as in Fig. 1, we solved numerically the RG equations Eqs. (42)–(44) for $H < H_0$ and Eqs. (67)–(69) for $H_0 < H < H_1$. Thereby, a set of parameters in the RG equations is chosen in the following way.

C_{ab} has an engineering dimension of (length)/(energy). From Eq. (C26), we set

$$C_{ab} = \frac{2\alpha}{\Lambda_{\mathcal{E}}}, \qquad (C27)$$

for any $a, b = 1, 2, 3, 4$. α is the lattice constant of the graphite along the c axis, $\alpha = c_0 = 6.7$ Å. $\Lambda_{\mathcal{E}}$ is a high-energy cutoff in the energy scale. We set this to be the bandwidth of the four pockets, $\Lambda_{\mathcal{E}} = 40$ meV.

According to Eqs. (39)–(41), $m_{(2)}, h_{(2)}, \overline{h}_{(2)}, n_{(2)}, p_{(2)}$, and $\overline{p}_{(2)}$ have the same engineering dimension as $\tilde{g} \equiv g/\alpha^2$, where g represents an interaction strength as in Eq. (7). For initial values of $m_{(2)}, \ldots, \overline{p}_{(2)}$ in the RG flow, we set

$$(m_{(2)}, h_{(2)}, \overline{h}_{(2)}) = \tilde{g}\,(3, -1.25, -1.25),$$

$$(n_{(2)}, p_{(2)}, \overline{p}_{(2)}) = \tilde{g}\,(-1.1, -1.25, -1.25). \quad (C28)$$

A value of $\tilde{g}$ is set in the following way. We consider that the interaction is from the Coulomb interaction and therefore its typical interaction energy scale is given by

$$E_{\text{int}} = \frac{e^2}{\epsilon l}. \qquad (C29)$$

The magnetic length l depends on the magnetic field and the relative permittivity ϵ is set to 13 for graphite. We regard that the Coulomb interaction ranges over the magnetic length in the xy plane, and ranges over the Thomas-Fermi screening length along the z direction λ_{TF}. We thus compare E_{int} with $g/(l^2 \lambda_{\text{TF}})$ [see Eq. (7)]. This leads to

$$\tilde{g} = \frac{g}{\alpha^2} = \frac{e}{\epsilon l} \frac{l^2}{\alpha^2} \lambda_{\text{TF}}. \qquad (C30)$$

The screening length along the c axis is set to $\lambda_{\text{TF}} = c_0/\sqrt{6}$.

A_{ab} in the RG equations is given by Eq. (38). $u_c\Lambda$ in Eq. (38) ($c = 1, 2, 3, 4$) is set to the high-energy cutoff in the energy scale, $\Lambda_{\mathcal{E}} = 40$ meV. For the Luttinger parameters K_a in Eq. (38), we use Eq. (21). The intrapocket forward scattering strengths in Eq. (21) are set as

$$g_{4,a=1} = g_{4,a=4} = \tilde{g}, \quad g_{4,a=2} = g_{4,a=3} = \tilde{g},$$

$$g_{2,a=1} = g_{2,a=4} = \tilde{g}/1.6, \quad g_{2,a=2} = g_{2,a=3} = \tilde{g}/1.1,$$

where $\tilde{g}$ is given in Eq. (C30). The bare Fermi velocity in Eq. (21) $v_{F,a}$ is a k_z derivative of the energy dispersion of the four pockets given in Eq. (2):

$$v_{F,a} = \frac{\partial E_{n,\sigma}(k_z)}{\partial k_z}\bigg|_{k_z = k_{F,n,\sigma}} \equiv -2\gamma_2 c_0 \sin(2\pi\xi_{n,\sigma}) \quad (C31)$$

with $a = (n,\sigma)$; $1 = (0, \uparrow)$, $2 = (0, \downarrow)$, $3 = (-1, \uparrow)$, and $4 = (-1, \downarrow)$. We set $2\gamma_2 = 40$ meV, and

$$\xi_{0,\uparrow} = \frac{1}{4} - \frac{H}{200\text{ T}}, \quad \xi_{0,\downarrow} = \frac{1}{4} - \frac{H}{480\text{ T}},$$

$$\xi_{-1,\uparrow} = \frac{1}{4} + \frac{H}{480\text{ T}}, \quad \xi_{-1,\downarrow} = \frac{1}{4} + \frac{H}{200\text{ T}}. \qquad (C32)$$

Equation (C32) realizes $H_0 = 50$ T and $H_1 = 120$ T.

APPENDIX D: CALCULATION OF OPTICAL CONDUCTIVITY $\sigma_{zz}(\omega)$

In the main text, we describe how the longitudinal optical conductivity along the field direction behaves in the SNEI phases as well as the metal-insulator transition points at $H = H_{c,1}$ and $H = H_{c,2}$. According to the linear response theory, the conductivity is given by a retarded correlation function between an electron polarization operator $\hat{P}_z$ and current operator $\hat{J}_z$. In the bosonization language, the former is a sum of the displacement fields over the pocket index (a) and the chain index (j),

$$\hat{P}_z = -\frac{e}{\pi} \sum_j \sum_a \int dz \phi_{a,j}(z). \tag{D1}$$

The latter is a sum of the current density fields,

$$\hat{J}_z = \frac{e}{\pi} \sum_j \sum_a u_a K_a \int dz \partial_z \theta_{a,j}(z). \tag{D2}$$

The correlation function is calculated with respect to the mean-field action for the SNEI phases. For the mean-field action, we employ a Gaussian approximation for $H_{u,2}$ and $H'_{u,2}$, to replace their cosine terms by proper quadratic terms,

$$H_{u,2} \simeq \sum_{j,m} M^{(2)}_{j-m} \int dz \, \{(\phi_{2,j} + \phi_{3,j} + \phi_{1,m} + \phi_{4,m})^2$$

$$+ (\theta_{2,j} - \theta_{3,j} + \theta_{1,m} - \theta_{4,m})^2\},$$

$$H'_{u,2} \simeq \frac{1}{2} \sum_{j,m} N^{(2)}_{j-m} \int dz \, \{(\phi_{2,j} + \phi_{3,j} + \phi_{2,m} + \phi_{3,m})^2$$

$$+ (\theta_{2,j} - \theta_{3,j} - \theta_{2,m} + \theta_{3,m})^2\}.$$

This in combination with H_0 in Eq. (19) gives a Gaussian ("mean-field") action that takes the form of

$$\mathcal{S}_{\text{MF}} = \frac{1}{2\beta L_z N} \sum_K (\vec{\phi}^\dagger_K \quad \vec{\theta}^\dagger_K)[\boldsymbol{M}_{0,K}]\begin{pmatrix} \vec{\phi}_K \\ \vec{\theta}_K \end{pmatrix}, \tag{D3}$$

with $K \equiv (k_z, k, i\omega_n)$. The Fourier transform is taken with respect to the spatial coordinate z, imaginary time τ, and the chain index j ($y_j \equiv 2\pi l^2 j/L_x$):

$$\phi_{a,j}(z, \tau) \equiv \frac{1}{\beta L_z N} \sum_K e^{ik_z z + ik y_j - i\omega_n \tau} \phi_{a,K}. \tag{D4}$$

In the following, we briefly summarize how to calculate the retarded correlation function with respect to $\mathcal{S}_{\text{MF}}$ in the SNEI-I phase with/without disorder.

For the model with two electron pockets and two hole pockets, the Gaussian action is described by an 8×8 matrix,

$$[\boldsymbol{M}_{0,K}] \equiv \begin{bmatrix} \boldsymbol{A}_K & \boldsymbol{B}_K \\ \boldsymbol{C}_K & \boldsymbol{D}_K \end{bmatrix}. \tag{D5}$$

A 4×4 matrix $\boldsymbol{A}_K$ is for the displacement fields of the four pockets ϕ_a ($a = 1, 2, 3, 4$), and 4×4 matrix $\boldsymbol{D}_K$ is for the superconducting phase fields of the four pockets θ_a ($a = 1, 2, 3, 4$). They are given by

$$\boldsymbol{A}_K \equiv \begin{bmatrix} \frac{u_1}{\pi K_1}k_z^2 + 2M(0) & 2M(0) & 2M^*(k) & 2M^*(k) \\ 2M(0) & \frac{u_4}{\pi K_4}k_z^2 + 2M(0) & 2M^*(k) & 2M^*(k) \\ 2M(k) & 2M(k) & \frac{u_2}{\pi K_2}k_z^2 + 2M(0) & 2M(0) \\ 2M(k) & 2M(k) & 2M(0) & \frac{u_3}{\pi K_3}k_z^2 + 2M(0) \end{bmatrix}, \tag{D6}$$

$$\boldsymbol{D}_K \equiv \begin{bmatrix} \frac{u_1 K_1}{\pi}k_z^2 + 2M(0) & -2M(0) & 2M^*(k) & -2M^*(k) \\ -2M(0) & \frac{u_4 K_4}{\pi}k_z^2 + 2M(0) & -2M^*(k) & 2M^*(k) \\ 2M(k) & -2M(k) & \frac{u_2 K_2}{\pi}k_z^2 + 2M(0) & -2M(0) \\ -2M(k) & 2M(k) & -2M(0) & \frac{u_3 K_3}{\pi}k_z^2 + 2M(0) \end{bmatrix}, \tag{D7}$$

where $M(k) \equiv \sum_j M^{(2)}_j e^{ik y_j}$. The other 4×4 matrices $\boldsymbol{B}_K$ and $\boldsymbol{C}_K$ connect the four ϕ fields and the four θ fields,

$$\boldsymbol{B}_K = \boldsymbol{C}_K = \frac{ik_z \omega_n}{\pi} \mathbf{1}_{4 \times 4}. \tag{D8}$$

$\mathbf{1}_{4 \times 4}$ stands for the 4×4 unit matrix.

For later convenience, we introduce a new basis with respect to the pocket index:

$$\vec{\Phi} \equiv \begin{bmatrix} \Phi_+ \\ \Phi_I \\ \Phi_{II} \\ \Phi_{III} \end{bmatrix} \equiv \frac{1}{2}\begin{bmatrix} 1 & 1 & 1 & 1 \\ 1 & 1 & -1 & -1 \\ 1 & -1 & 1 & -1 \\ 1 & -1 & -1 & 1 \end{bmatrix}\begin{bmatrix} \phi_1 \\ \phi_4 \\ \phi_2 \\ \phi_3 \end{bmatrix} \equiv \boldsymbol{T}\vec{\phi},$$

$$\vec{\Theta} \equiv \boldsymbol{T}\vec{\theta}. \tag{D9}$$

On the right-hand side, we omitted the subscript K for the ϕ, θ, Φ, and Θ fields. With the new basis, the Gaussian action is given by

$$\mathcal{S}_{\text{MF}} = \frac{1}{2\beta L_z N} \sum_K (\vec{\Phi}_K^\dagger \quad \vec{\Theta}_K^\dagger)[M_{c,K}] \begin{pmatrix} \vec{\Phi}_K \\ \vec{\Theta}_K \end{pmatrix}$$

and

$$[M_{c,K}] \equiv \begin{bmatrix} T\,A_K\,T & B_K \\ C_K & T\,D_K\,T \end{bmatrix}. \tag{D10}$$

We consider that the total displacement field Φ_+ couples with a disorder potential through

$$\hat{H}_{\text{imp}} = \sum_j \int dz\, \epsilon_j(z)\Phi_{+,j}^2(z). \tag{D11}$$

Physically, such disorder potential $\epsilon_j(z)$ is nothing but a local fluctuation of the dielectric constant. We take a quenched average over the local fluctuation as

$$\overline{\cdots} \equiv \frac{\int d\epsilon_j(z) \cdots e^{-\frac{1}{g_y}\sum_j \int dz\, \epsilon_j^2(z)}}{\int d\epsilon_j(z)\, e^{-\frac{1}{g_y}\sum_j \int dz\, \epsilon_j^2(z)}}. \tag{D12}$$

g_y stands for the disorder strength associated with spatially (but not temporally) fluctuating dielectric constant.

We first calculate an imaginary-time time-ordered correlation function between $\hat{P}_z$ and $\hat{J}_z$, and then take an analytic continuation, $i\omega_n \to \omega + i\eta$. This gives the retarded correlation function. The real part of the retarded correlation function is nothing but the optical conductivity $\sigma_{zz}(\omega)$:

$$\sigma_{zz}(\omega) = \text{Re}\{\overline{\sigma_{zz}(i\omega_n)}_{|i\omega_n=\omega+i\eta}\},$$
$$\overline{\sigma_{zz}(i\omega_n)} = \vec{e}_+^T\, U^{-1}\, T\, \overline{Q_{zz}^c(i\omega_n)}\, T\, \vec{e}_+, \tag{D13}$$

with $\vec{e}_+ \equiv (1,1,1,1)^T$. U^{-1} and $Q_{zz}^c(i\omega_n)$ $[\overline{Q_{zz}^c(i\omega_n)}$ is the quenched average of $Q_{zz}^c(i\omega_n)]$ as well as T are 4×4 matrices,

$$U^{-1} \equiv \begin{bmatrix} u_1 K_1 & & & \\ & u_4 K_4 & & \\ & & u_2 K_2 & \\ & & & u_3 K_3 \end{bmatrix}. \tag{D14}$$

$Q_{zz}^c(i\omega_n)$ is a Fourier transform of the imaginary-time time-ordered correlation function between four Φ fields and four Θ fields,

$$Q_{zz}^c(i\omega_n) = \int_0^\beta d\tau\, Q_{zz}^c(\tau)\, e^{i\omega_n \tau},$$
$$[Q_{zz}^c(\tau)]_{\alpha\beta} \equiv \frac{e^2}{\pi^2 V} \sum_{j,m} \int dz \int dz'\, [R_{jm}^c(\tau, z|0, z')]_{\alpha\beta},$$
$$[R_{jm}^c(\tau, z|0, z')]_{\alpha\beta} \equiv \frac{\int d\vec{\Phi} d\vec{\Theta} e^{-\mathcal{S}_{\text{MF}}} \partial_z \Theta_{\alpha,j}(z, \tau)\Phi_{\beta,m}(z, 0)}{\int d\vec{\Phi} d\vec{\Theta} e^{-\mathcal{S}_{\text{MF}}}}, \tag{D15}$$

with $\alpha, \beta = +, \text{I}, \text{II}, \text{III}$ and the chain index $j, m = 1, \ldots, S/(2\pi l^2)$.

With the use of a Born approximation [25], we can take the quenched average of $Q_{zz}^c(i\omega_n)$,

$$\overline{Q_{zz}^c(-i\omega_n)}^T = \frac{2e^2}{\pi^2 V} \sum_m \int dz'' \sum_k e^{-ik_z z''-iky_m}(-ik_z)$$
$$\times \{ \mathbf{1}_{4\times 4} - [M_{c,K}^{-1}]_{\Phi\Phi}\,[P(i\omega_n)] \}^{-1} [M_{c,K}^{-1}]_{\Phi\Theta}, \tag{D16}$$

where $[M_{c,K}^{-1}]_{\Phi\Phi}$, $[M_{c,K}^{-1}]_{\Phi\Theta}$, and $[P(i\omega_n)]$ are 4×4 matrices. $[M_{c,K}^{-1}]_{\Phi\Phi}$ and $[M_{c,K}^{-1}]_{\Phi\Theta}$ are 4×4 blocks of an inverse of the 8×8 matrix $[M_{c,K}]$ that connects Φ and Φ and that connects ϕ and Θ, respectively:

$$[M_{c,K}^{-1}]_{\Phi\Phi} \equiv T\,(A - BD^{-1}C)^{-1}\,T, \tag{D17}$$
$$[M_{c,K}^{-1}]_{\Phi\Theta} \equiv T\,(A - BD^{-1}C)^{-1}\,BD^{-1}\,T. \tag{D18}$$

4×4 matrices A, B, C, D, and T on the right-hand sides are given by Eqs. (D6)–(D9). $[P(i\omega_n)]$ is a 4×4 diagonal matrix that represents the effect of the disorder,

$$[P(i\omega_n)] \equiv \begin{bmatrix} g_y m(i\omega_n) & & & \\ & 0 & & \\ & & 0 & \\ & & & 0 \end{bmatrix}. \tag{D19}$$

$m(i\omega_n)$ is the sum of the (Φ_+, Φ_+) component of the inverse of the 8×8 matrix $[M_{c,K}]$ over $k \equiv (k_z, k)$:

$$m(i\omega_n) \equiv \frac{2}{L_z N} \sum_k [M_{c,K}^{-1}]_{\Phi_+\Phi_+}. \tag{D20}$$

Note that $m(i\omega_n)$ is an even function of ω_n (see below).

One may rewrite Eq. (D16) into

$$\overline{Q_{zz}^c(-i\omega_n)}^T$$
$$= \frac{2e^2}{\pi^2 V} \sum_m \int dz'' \sum_k e^{-ik_z z''-iky_m}(-\omega_n)T$$
$$\times \left[\frac{\pi^2}{k_z^2}(DA - DTPT) + \omega_n^2 \mathbf{1}_{4\times 4} \right]^{-1} T$$
$$= -\frac{e^2 \omega_n}{\pi^2 l^2} T \left[\frac{\pi^2}{k_z^2}(DA - DTPT) + \omega_n^2 \mathbf{1}_{4\times 4} \right]^{-1}_{|k=0} T. \tag{D21}$$

From the first to the second line, we took the sum over the chain index m and the integral over z'':

$$\frac{1}{V} \sum_m \int dz'' e^{-ik_z z''-iky_m} = \frac{1}{2\pi l^2} \delta_{k,0}^2. \tag{D22}$$

Substituting Eq. (D21) into Eq. (D13), we obtain the imaginary-time optical conductivity as

$$\overline{\sigma_{zz}(i\omega_n)} = \frac{e^2 \omega_n}{\pi^2 l^2} \vec{e}_+^T \left[\frac{\pi^2}{k_z^2}(DA - DTPT) + \omega_n^2 \mathbf{1}_{4\times 4} \right]^{-1}_{|k=0}$$
$$\times U^{-1} \vec{e}_+. \tag{D23}$$

The $k = 0$ limit in the integrand is well defined. To see this, use Taylor expansions of A and D in small k:

$$A_K = 2M(0)A_0 + k_z^2 A_1 + O(k), \quad D_K = 2M(0)D_0 + k_z^2 D_1 + O(k),$$

with

$$A_0 \equiv \begin{bmatrix} 1 & 1 & 1 & 1 \\ 1 & 1 & 1 & 1 \\ 1 & 1 & 1 & 1 \\ 1 & 1 & 1 & 1 \end{bmatrix}, \quad D_0 \equiv \begin{bmatrix} 1 & -1 & 1 & -1 \\ -1 & 1 & -1 & 1 \\ 1 & -1 & 1 & -1 \\ -1 & 1 & -1 & 1 \end{bmatrix},$$

and

$$A_1 \equiv \frac{1}{\pi} \begin{bmatrix} \frac{u_1}{K_1} & & & \\ & \frac{u_4}{K_4} & & \\ & & \frac{u_2}{K_2} & \\ & & & \frac{u_3}{K_3} \end{bmatrix}, \quad D_1 \equiv \frac{1}{\pi} \begin{bmatrix} u_1 K_1 & & & \\ & u_4 K_4 & & \\ & & u_2 K_2 & \\ & & & u_3 K_3 \end{bmatrix}.$$

Since $D_0 T P = 0$ and $D_0 A_0 = 0$, the integrand in the $k = 0$ limit takes a finite value:

$$\lim_{k_z \to 0} \lim_{k \to 0} \frac{1}{k_z^2}(D_K A_K - D_K T P T) = 2M(0)(D_0 A_1 + D_1 A_0) - D_1 T P T = 2M(0)D_0 A_1 + \frac{1}{\pi}\left[2M(0) - \frac{g_y m(i\omega_n)}{4}\right]U^{-1}A_0.$$

From the second to the last line, we used $T P T = \frac{g_y m(i\omega_n)}{4} A_0$ and $\pi D_1 = U^{-1}$.

The imaginary-time optical conductivity is further calculated from Eq. (D23) as

$$\overline{\sigma_{zz}(i\omega_n)} = \frac{e^2 \omega_n}{\pi^2 l^2} \vec{e}_+^T \left[2\pi^2 M(0)D_0 A_1 + \pi\left(2M(0) - \frac{g_y m(i\omega_n)}{4}\right)U^{-1}A_0 + \omega_n^2 \mathbf{1}_{4\times 4}\right]^{-1} U^{-1}\vec{e}_+$$

$$= \frac{e^2 \omega_n}{\pi^2 l^2} \vec{e}_+^T \left[\pi\left(2M(0) - \frac{g_y m(i\omega_n)}{4}\right)U^{-1}\vec{e}_+\vec{e}_+^T + \omega_n^2 \mathbf{1}_{4\times 4}\right]^{-1} U^{-1}\vec{e}_+, = \frac{e^2 uK}{\pi^2 l^2} \frac{\omega_n}{\omega_n^2 + \pi uK\left[2M(0) - \frac{g_y m(i\omega_n)}{4}\right]},$$

(D24)

with $uK \equiv \sum_{a=1,2,3,4} u_a K_a$. From the first to the second line, we used $A_0 D_0 = 0$, $\vec{e}_+^T D_0 = 0$, and $A_0 = \vec{e}_+\vec{e}_+^T$. From the second to the last line, we used $\vec{e}_+^T U^{-1}\vec{e}_+ = uK$. In the clean limit ($g_y = 0$), this gives $\sigma_{zz}(\omega) = (e^2 uK)/(2\pi l^2)\delta(\omega - \omega_g)$ with $\omega_g \equiv 2\pi uK \sum_j M_j^{(2)}$ after the analytic continuation.

The effect of the disorder average is included in $m(i\omega_n)$. To see this effect in $\sigma_{zz}(\omega)$, let us take $u_1 = u_4$, $K_1 = K_4$, $u_2 = u_3$, and $K_2 = K_3$ for simplicity. With the use of $M(k) = 0$ for $k \gg 1/l$ [25], we obtain the following expression for $m(i\omega_n)$,

$$m(i\omega_n) = \frac{\pi}{2}\left(\frac{K_1}{\sqrt{\omega_n^2 + \omega_1^2}} + \frac{K_2}{\sqrt{\omega_n^2 + \omega_2^2}}\right), \quad (D25)$$

with $\omega_1^2 \equiv 4\pi M(0)u_1 K_1 < 4\pi M(0)u_2 K_2 \equiv \omega_2^2$. After the analytic continuation, we finally obtain the optical conductivity as follows,

$$\sigma_{zz}(\omega) = \begin{cases} \frac{e^2 uK}{\pi l^2} \frac{|\omega_*|}{|g'(\omega_*)|}\delta(\omega - \omega_*), & 0 < \omega < \omega_1, \\ \frac{e^2 uK}{\pi^2 l^2} \frac{\omega b_1(\omega)}{a_1^2(\omega) + b_1^2(\omega)}, & \omega_1 < \omega < \omega_2, \\ \frac{e^2 uK}{\pi l^2} \frac{\omega b_2(\omega)}{a_2^2(\omega) + b_2^2(\omega)}, & \omega_1 < \omega_2 < \omega, \end{cases} \quad (D26)$$

where

$$g(\omega) = -\omega^2 + \omega_g^2 - \frac{g_y}{4}\frac{\pi^2 uK}{2}\left(\frac{K_1}{\sqrt{\omega_1^2 - \omega^2}} + \frac{K_2}{\sqrt{\omega_2^2 - \omega^2}}\right),$$

and

$$a_1(\omega) \equiv -\omega^2 + \omega_g^2 - \frac{g_y}{4}\frac{\pi^2 uK}{2}\frac{K_2}{\sqrt{\omega_2^2 - \omega^2}},$$

$$b_1(\omega) \equiv \frac{g_y}{4}\frac{\pi^2 uK}{2}\frac{K_1}{\sqrt{\omega^2 - \omega_1^2}},$$

and

$$a_2(\omega) \equiv -\omega^2 + \omega_g^2,$$

$$b_2(\omega) \equiv \frac{g_y}{4}\frac{\pi^2 uK}{2}\left(\frac{K_1}{\sqrt{\omega^2 - \omega_1^2}} + \frac{K_2}{\sqrt{\omega^2 - \omega_2^2}}\right).$$

Note that $\omega = \omega_*(< \omega_g)$ in Eq. (D26) is one and only one solution of $g(\omega) = 0$ within $0 < \omega < \omega_1$. The renormalized gap ω_* becomes progressively smaller, when the disorder strength increases. There exists a critical value of the disorder,

$$g_{y,c} \equiv \frac{1}{\pi^2 uK}\frac{8\omega_g^2 \omega_1 \omega_2}{K_1 \omega_2 + K_2 \omega_1}. \quad (D27)$$

When g_y approaches the critical value, the renormalized gap ω_* reduces to zero continuously. At $g_y = g_{y,c}$, the system undergoes a quantum phase transition from the SNEI-I phase ($g_y < g_{y,c}$) to a disorder-driven phase ($g_y > g_{y,c}$). To obtain Fig. 5, we use the same parameter sets as in Appendix C4. We set $u_1 = u_4$ and $u_2 = u_3$ by Eq. (20). We set g_y to be smaller than $g_{y,c}$.

APPENDIX E: MAGNETISM AND SPIN NEMATICITY IN SNEI PHASES

SNEI phases introduced in the main text are characterized by particle-hole pairings between $n = 0$ LL with $\uparrow$ ($\downarrow$) spin and $n = -1$ LL with $\downarrow$ ($\uparrow$) spins. The phases break the U(1) spin rotational symmetry around the field direction. Nonetheless, neither the A-carbon-site π-orbital electron spin nor the B-carbon-site electron spins exhibit magnetic order in the SNEI phases:

$$\langle S_{A,+}(\boldsymbol{r}) \rangle = \langle \psi_\uparrow^\dagger(\boldsymbol{r}, A) \psi_\downarrow(\boldsymbol{r}, A) \rangle = 0,$$

$$\langle S_{B,+}(\boldsymbol{r}) \rangle = \langle \psi_\uparrow^\dagger(\boldsymbol{r}, B) \psi_\downarrow(\boldsymbol{r}, B) \rangle$$

$$= \frac{1}{L_x} \sum_j [Y_{1,j}(y) Y_{0,j}(y)] \sum_{\tau = \pm} [\gamma_{B,\uparrow}^* \eta_{B,\downarrow} e^{-i\tau(k_{F,1} + k_{F,4})z} \langle \psi_{1,\tau,j}^\dagger \psi_{4,-\tau,j} \rangle$$

$$+ \eta_{B,\uparrow}^* \gamma_{B,\downarrow} e^{-i\tau(k_{F,2} + k_{F,3})z} \langle \psi_{3,\tau,j}^\dagger \psi_{2,-\tau,j} \rangle] = 0, \tag{E1}$$

because

$$\lim_{L_x \to \infty} \frac{1}{L_x} \sum_j Y_{1,j}(y) Y_{0,j}(y) = \frac{1}{2\pi l^2} \int dy \, Y_{1,j}(y) Y_{0,j}(y) = 0.$$

Magnetism of the SNEI-I phase is most explicitly manifested by the long-range order of the symmetric part of the 2nd-rank spin tensor composed of the spin-$\frac{1}{2}$ moment of the A-carbon-site π-orbital electron and that of the B-carbon site. Such 2nd-rank spin tensor has two components,

$$Q_{+-}^{AB}(\boldsymbol{r}) \equiv \langle S_{A,+}(\boldsymbol{r}) S_{B,-}(\boldsymbol{r}) \rangle, \quad Q_{++}^{AB}(\boldsymbol{r}) \equiv \langle S_{A,+}(\boldsymbol{r}) S_{B,+}(\boldsymbol{r}) \rangle.$$

In the SNEI-I phase, $Q_{+-}^{AB}(\boldsymbol{r})$ vanishes identically, while $Q_{++}^{AB}(\boldsymbol{r})$ exhibits both a ferro-type and a density-wave-type order:

$$Q_{++}^{AB}(\boldsymbol{r}) = \langle \psi_\uparrow^\dagger(\boldsymbol{r}, A) \psi_\downarrow(\boldsymbol{r}, A) \psi_\uparrow^\dagger(\boldsymbol{r}, B) \psi_\downarrow(\boldsymbol{r}, B) \rangle = \frac{1}{L_x} \left[\sum_j Y_{0,j}^2(y) \right] \frac{1}{L_x} \left[\sum_m Y_{0,m}^2(y) \right] \{ \gamma_{A,\uparrow}^* \gamma_{A,\downarrow} \eta_{B,\downarrow} \eta_{B,\uparrow}^* e^{-2i\Theta_-}$$

$$+ \gamma_{A,\uparrow}^* \gamma_{A,\downarrow} \eta_{B,\downarrow} \eta_{B,\uparrow}^* e^{-2i\Theta_-} + \gamma_{A,\uparrow}^* \gamma_{A,\downarrow} \eta_{B,\downarrow} \eta_{B,\uparrow}^* e^{i\Delta K z} e^{-i2\Phi_- - 2i\Theta_-} + \gamma_{A,\uparrow}^* \gamma_{A,\downarrow} \eta_{B,\downarrow} \eta_{B,\uparrow}^* e^{-i\Delta K z} e^{i2\Phi_- - 2i\Theta_-} \},$$

with $\Delta K \equiv k_{F,2} + k_{F,3} - k_{F,1} - k_{F,4}$. Here we used Eqs. (45)–(47) and

$$\langle \psi_{1,+,j}^\dagger(z) \psi_{4,-,m}(z) \rangle = \delta_{jm} i \sigma_{\bar{4}1,m} e^{i(\phi_1 + \phi_4) + i(\theta_4 - \theta_1)}, \quad \langle \psi_{1,-,j}^\dagger(z) \psi_{4,+,m}(z) \rangle = \delta_{jm} i \sigma_{4\bar{1},m} e^{-i(\phi_1 + \phi_4) + i(\theta_4 - \theta_1)},$$

$$\langle \psi_{2,+,j}(z) \psi_{3,-,m}^\dagger(z) \rangle = \delta_{jm} i \sigma_{\bar{3}2,m} e^{-i(\phi_2 + \phi_3) - i(\theta_3 - \theta_2)}, \quad \langle \psi_{2,-,j}(z) \psi_{3,+,m}^\dagger(z) \rangle = \delta_{jm} i \sigma_{3\bar{2},m} e^{i(\phi_2 + \phi_3) - i(\theta_3 - \theta_2)}.$$

The spatial inversion symmetry generally allows

$$\gamma_{A,\uparrow}^* \gamma_{A,\downarrow} \eta_{B,\downarrow} \eta_{B,\uparrow}^* = u. \tag{E2}$$

This gives

$$Q_{++}^{ab}(\boldsymbol{r}) = \frac{e^{-2i\Theta_-}}{(\pi^2 l^2)^2} [u + u \cos(\Delta K z - 2\Phi_-)]. \tag{E3}$$

Note also that the SNEI phases could be accompanied by a long-range ordering of small magnetic moments within the xy plane. Nonetheless, the moment does exist only in those spatial regions in the unit cell where two π orbitals of the A-carbon site and B-carbon site overlap. This statement is suggested by Eq. (E1) and finite expectation values of the following two quantities in the SNEI phases:

$$\langle \psi_\uparrow^\dagger(\boldsymbol{r}, A) \psi_\downarrow(\boldsymbol{r}, B) \rangle = \frac{\sqrt{2} i v}{\pi l^2} e^{-i\Theta_-} \cos[(k_{F,1} + k_{F,4})z + \Phi_-],$$

$$\langle \psi_\downarrow^\dagger(\boldsymbol{r}, A) \psi_\uparrow(\boldsymbol{r}, B) \rangle = \frac{\sqrt{2} i w}{\pi l^2} e^{i\Theta_-} \cos[(k_{F,2} + k_{F,3})z - \Phi_-],$$

with

$$v \equiv \gamma_{A,\uparrow}^* \eta_{B,\downarrow} \langle \sigma_{1\bar{4},j} \rangle \neq 0, \quad w \equiv \gamma_{A,\downarrow}^* \eta_{B,\uparrow} \langle \sigma_{2\bar{3},j} \rangle \neq 0.$$

[1] S. Tanuma, R. Inaba, A. Furukawa, O. Takahashi, Y. Iye, and Y. Onuki, in *Physics in High Magnetic Fields*, edited by S. Chikazumi and N. Miura (Springer, Berlin, 1981), p. 316.

[2] Y. Iye, P. M. Tedrow, G. Timp, M. Shayegan, M. S. Dresselhaus, G. Dresselhaus, A. Furukawa, and S. Tanuma, Phys. Rev. B **25**, 5478 (1982).

[3] H. Fukuyama, Solid State Commun. **26**, 783 (1978).

[4] D. Yoshioka and H. Fukuyama, J. Phys. Soc. Jpn. **50**, 725 (1981).

[5] Y. Iye, P. M. Berglund, and L. E. McNeil, Solid State Commun. **52**, 975 (1984).

[6] Y. Iye and G. Dresselhaus, Phys. Rev. Lett. **54**, 1182 (1985).

[7] K. Takahashi and Y. Takada, Physica B **201**, 384 (1994).

[8] Y. Takada and H. Goto, J. Phys.: Condens. Matter **10**, 11315 (1998).

[9] K. Sugihara, Phys. Rev. B **29**, 6722 (1984).

[10] Z. Tesanovic and B. I. Halperin, Phys. Rev. B **36**, 4888 (1987).

[11] A. H. MacDonald and Garnett W. Bryant, Phys. Rev. Lett. **58**, 515 (1987).

[12] V. M. Yakovenko, Phys. Rev. B **47**, 8851 (1993).

[13] H. Ochimizu, T. Takamasu, S. Takeyama, S. Sasaki, and N. Miura, Phys. Rev. B **46**, 1986 (1992).

[14] H. Yaguchi and J. Singleton, Phys. Rev. Lett. **81**, 5193 (1998).

[15] H. Yaguchi and J. Singleton, Physica B **256–258**, 621 (1998).

[16] H. Yaguchi, J. Singleton, and T. Iwata, Physica B **298**, 546 (2001).

[17] B. Fauque, D. LeBoeuf, B. Vignolle, M. Nardone, C. Proust, and K. Behnia, Phys. Rev. Lett. **110**, 266601 (2013).

[18] K. Akiba, A. Miyake, H. Yaguchi, A. Matsuo, K. Kindo, and M. Tokunaga, J. Phys. Soc. Jpn. **84**, 054709 (2015).

[19] F. Arnold, A. Isidori, E. Kampert, B. Yager, M. Eschrig, and J. Saunders, Phys. Rev. Lett. **119**, 136601 (2017).

[20] Z. Zhu, R. D. MacDonald, A. Shekhter, B. J. Ramshaw, K. A. Modic, F. F. Balakirev, and N. Harrison, Sci. Rep. **7**, 1733 (2017).

[21] Z. Zhu, P. Nie, B. Fauqué, R. D. McDonald, N. Harrison, and K. Behnia, arXiv:1808.03558.

[22] Y. Imry and S. K. Ma, Phys. Rev. Lett. **35**, 1399 (1976).

[23] L. J. Sham and B. R. Patton, Phys. Rev. B **13**, 3151 (1976).

[24] H. Fukuyama and P. A. Lee, Phys. Rev. B **17**, 535 (1978).

[25] X. T. Zhang and R. Shindou, Phys. Rev. B **95**, 205108 (2017).

[26] G. Gruner, *Density Waves in Solids* (Perseus Publishing, Cambridge, MA, 2000).

[27] B. I. Halperin, Jpn. J. Appl. Phys. **26**, 1913 (1987).

[28] L. Balents and M. P. A. Fisher, Phys. Rev. Lett. **76**, 2782 (1996).

[29] P. R. Wallace, Phys. Rev. **71**, 622 (1947).

[30] J. C. Slonczewski and P. R. Weiss, Phys. Rev. **99**, 636 (1955).

[31] J. W. McClure, Phys. Rev. **108**, 612 (1957).

[32] M. Inoue, J. Phys. Soc. Jpn. **17**, 808 (1962).

[33] G. Dresselhaus and M. S. Dresselhaus, Phys. Rev. **140**, A401 (1965).

[34] K. Nakao, J. Phys. Soc. Jpn. **40**, 761 (1976).

[35] S. Uji, J. S. Brooks, and Y. Iye, Physica B **246-247**, 299 (1998).

[36] Y. Kopelevich, B. Raquet, M. Goiran, W. Escoffier, R. R. da Silva, J. C. Medina Pantoja, I. A. Luk'yanchuk, A. Sinchenko, and P. Monceau, Phys. Rev. Lett. **103**, 116802 (2009).

[37] A. Kumar, J. Poumirol, W. Escoffier, M. Goiran, B. Raquet, and J. C. Pivin, J. Phys.: Condens. Matter **22**, 436004 (2010).

[38] C. Biagini, D. L. Maslov, M. Y. Reizer, and L. I. Glazman, Europhys. Lett. **55**, 383 (2001).

[39] S. W. Tsai, D. L. Maslov, and L. I. Glazman, Phys. Rev. B **65**, 241102(R) (2002).

[40] S. W. Tsai, D. L. Maslov, and L. I. Glazman, Physica B **312-313**, 586 (2002).

[41] A. A. Abrikosov, J. Low Temp. Phys. **2**, 37 (1970); **10**, 3 (1973).

[42] S. A. Brazovskii, Zh. Eksp. Teor. Fiz. **62**, 820 (1972) [Sov. Phys. JETP **35**, 433 (1972)]; Zh. Eksp. Teor. Fiz. **61**, 2401 (1971) [Sov. Phys. JETP **34**, 1286 (1972)].

[43] T. Giamarchi, *Quantum Physics in One Dimension* (University Press, Oxford, 2004).

[44] E. W. Fenton, Phys. Rev. **170**, 816 (1968).

[45] D. Jerome, T. M. Rice, and W. Kohn, Phs. Rev. **158**, 462 (1967).

[46] H. Yaguchi and J. Singleton, J. Phys.: Condens. Matter **21**, 344207 (2009).

[47] K. Matsubara, T. Tsuzuku, and K. Sugihara, Phys. Rev. B **44**, 11845 (1991).

[48] A. L. Fetter and J. D. Walecka, *Quantum Theory of Many-Particle Systems* (Dover Publications, Mineola, NY, 2003).

[49] G. Mahan, *Many-Particle Physics*, 3rd ed. (Kluwer Academic/ Plenum Publishers, New York, 2000).

[50] L. Fu, C. L. Kane, and E. J. Mele, Phys. Rev. Lett. **98**, 106803 (2007).

[51] R. Roy, Phys. Rev. B **79**, 195322 (2009).

[52] J. E. Moore and L. Balents, Phys. Rev. B **75**, 121306(R) (2007).

[53] A. J. Heeger, S. A. Kivelson, J. R. Schrieffer, and W. P. Su, Rev. Mod. Phys. **60**, 781 (1988).

[54] X. G. Wen and A. Zee, Nucl. Phys. B **316**, 641 (1989).

[55] M. Sato and S. Fujimoto, Phys. Rev. B **79**, 094504 (2009).

[56] J. T. Chalker and P. D. Coddington, J. Phys. C: Solid State Phys. **21**, 2665 (1988).

[57] C. M. Ho and J. T. Chalker, Phys. Rev. B **54**, 8708 (1996).

[58] F. Evers and A. D. Mirlin, Rev. Mod. Phys. **80**, 1355 (2008).

[59] D. LeBoeuf, C. W. Rischau, G. Seyfarth, R. Kuchler, M. Berben, S. Wiedmann, W. Tabis, M. Frachet, K. Behnia, and B. Fauque, Nat. Commun. **8**, 1337 (2017).

[60] R. Shankar, Physica A **177**, 530 (1991).

[61] A. Houghton and J. B. Marston, Phys. Rev. B **48**, 7790 (1993).

[62] M. Fabrizio, Phys. Rev. B **48**, 15838 (1993).

[63] A. H. Castro Neto, and E. Fradkin, Phys. Rev. Lett. **72**, 1393 (1994).

[64] A. H. Castro Neto, and E. Fradkin, Phys. Rev. B **49**, 10877 (1994).

[65] A. Houghton, H.-J. Kwon, and J. B. Marston, Phys. Rev. B **50**, 1351 (1994).

[66] V. J. Emery, E. Fradkin, S. A. Kivelson, and T. C. Lubensky, Phys. Rev. Lett. **85**, 2160 (2000).

[67] A. Vishwanath and D. Carpentier, Phys. Rev. Lett. **86**, 676 (2001).

[68] B. I. Halperin, Phys. Rev. B **25**, 2185 (1982).

[69] M. Buttiker, Phys. Rev. B **38**, 9375 (1988).

[70] P. Nozieres and F. Gallet, J. Phys. (Paris) **48**, 353 (1987).